

OKINAWA INSTITUTE OF SCIENCE AND TECHNOLOGY
GRADUATE UNIVERSITY

Thesis submitted for the degree of

Doctor of Philosophy

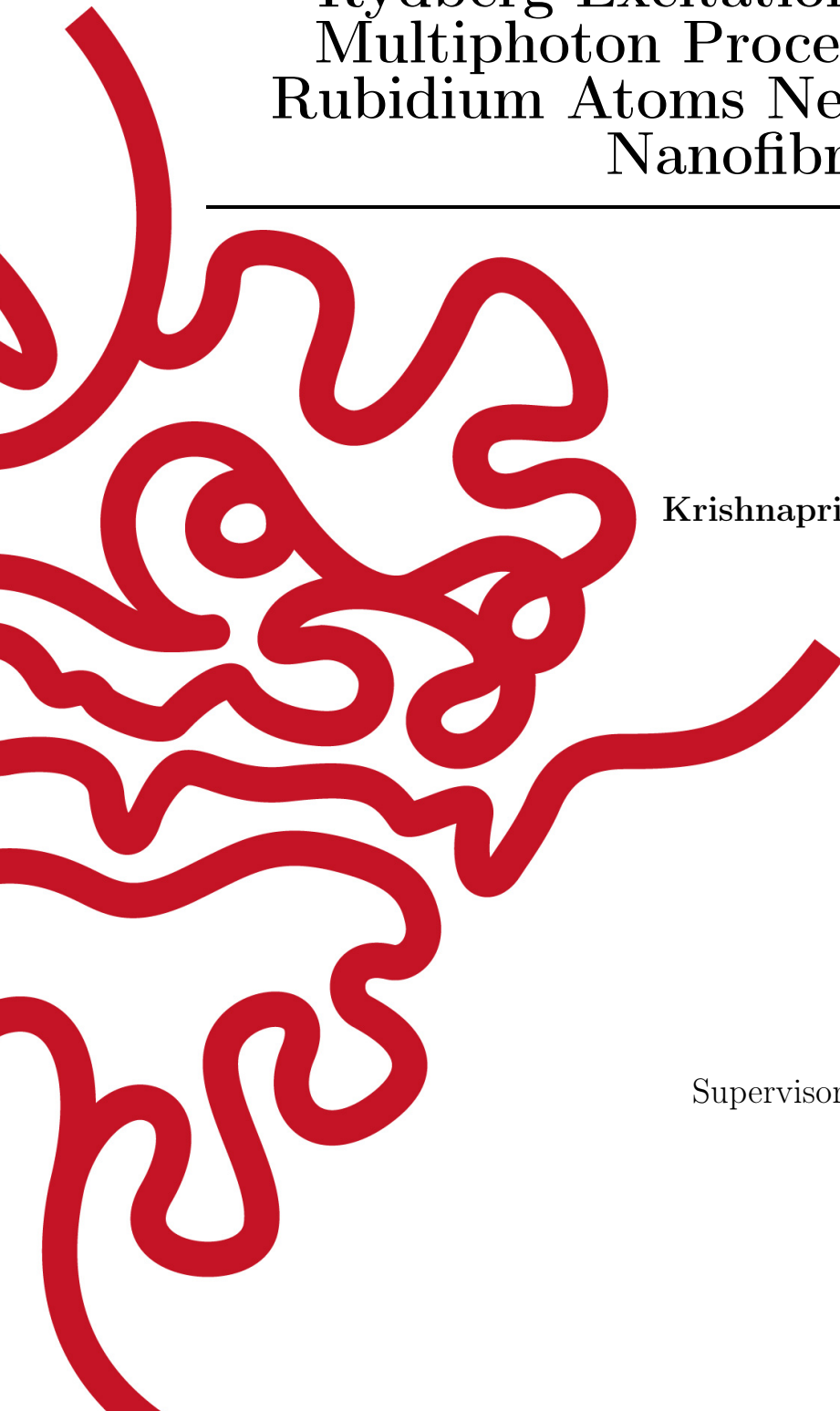
Rydberg Excitation and Other
Multiphoton Processes in Cold
Rubidium Atoms Near an Optical
Nanofibre

by

Krishnapriya Subramonian Rajasree

Supervisor: **Prof. Síle Nic Chormaic**

September 2020

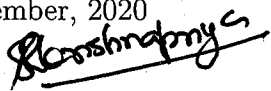


Declaration of Original and Sole Authorship

I, Krishnapriya Subramonian Rajasree, declare that this thesis entitled *Rydberg Excitation and Other Multiphoton Processes in Cold Rubidium Atoms Near an Optical Nanofibre* and the data presented in it are original and my own work. I confirm that:

- No part of this work has previously been submitted for a degree at this or any other university.
- References to the work of others have been clearly acknowledged. Quotations from the work of others have been clearly indicated and attributed to them.
- In cases where others have contributed to part of this work, such contribution has been clearly acknowledged and distinguished from my own work.
- None of this work has been previously published elsewhere, with the exception of the following:
 - T. Nieddu, T. Ray, K.S. Rajasree, R. Roy and S. Nic Chormaic, "Simple, narrow and robust atomic frequency reference at 993 nm exploiting the rubidium (Rb) $5S_{1/2}$ to $6S_{1/2}$ transition using one-color, two-photon excitation", *Opt. Express* **27**, 6528 (2019) [1]
 - K.S. Rajasree, T. Ray, K. Karlsson, J.L. Everett and S. Nic Chormaic, "Generation of cold Rydberg atoms at submicron distances from an optical nanofiber", *Phys. Rev. Research* **2**, 012038(R) (2020) *Rapid Communication* [2]
 - T. Ray, R.K. Gupta, V. Gokhroo, J.L. Everett, T. Nieddu, K.S. Rajasree and S. Nic Chormaic, "Observation of the ^{87}Rb $5S_{1/2}$ to $4D_{3/2}$ electric quadrupole transition at 516.6 nm mediated via an optical nanofibre" *New J. Phys.* **22**, 062001 (2020) *Fast Track Communication* [3]
 - K.S. Rajasree, R.K. Gupta, V. Gokhroo, F. Le Kien, T. Nieddu, T. Ray, S. Nic Chormaic and G. Tkachenko, "Spin selection in single-frequency two-photon excitation of alkali-metal atoms", *Phys. Rev. Research* **2**, 033341 (2020) [4]

Date: September, 2020

Signature: 

Abstract

Rydberg Excitation and Other Multiphoton Processes in Cold Rubidium Atoms Near an Optical Nanofibre

Optical nanofibres (ONF) are used to confine light in subwavelength dimensions. In ONFs, a large evanescent field component extends beyond the fibre surface into the surroundings. In this thesis, we propose and explore the possibility of exciting neutral rubidium Rydberg atoms near an ONF and thereby exploring new aspects of Rydberg physics heretofore experimentally inaccessible. Rydberg atoms exhibits many unique properties which makes them attractive. In this dissertation, optical methods to detect and manipulate Rydberg atoms such as multiphoton excitation and electromagnetically induced transparency (EIT) are investigated. The primary results of this dissertation shows that the Rydberg atoms have been generated no more than a few hundred nm from the ONF surface, through an atom loss method and advances in realising Rydberg EIT in an ONF-cold atom system is discussed. The single-frequency, two-photon excitation at 993 nm addressing the $5S_{1/2} \rightarrow 6S_{1/2}$ transition in ground state rubidium atoms mediated via the ONF is explored. The single-frequency, two-photon excitation serves as an alternative to two-photon excitation to Rydberg levels and could be crucial for developments in the neutral Rydberg atom-ONF interface, where we can avoid the possibility of ionisation. This thesis research forms the groundwork for future ONF-Rydberg atom studies of this nature.

Acknowledgements

First of all I want to begin by thanking my supervisor Prof. Sile Nic Chormaic, who has accepted and mentored me through out the research. I wish to express my gratitude for the invaluable advice, opportunities and exposure she has given me.

I express my sincere gratitude to Prof. Yabing Qi and Prof. Denis Konstantinov for being on my thesis committee and giving suggestions and comments throughout my PhD journey. I wish to express my acknowledgement to OIST Graduate School members, especially the Student Support Section who made an expat's student life so much easier. As part of OIST curriculum, I was fortunate to work in Prof. Thomas Busch's and Prof. Yoko Yasaki Sugiyama's units for lab rotations -the experiences from the labs have helped me during the course of my research.

I thank Dr. Tridib Ray, with whom I have worked closely from the start of my PhD journey. I have learnt many aspects of experimental research from him. I really appreciate his support throughout out my PhD. Dr. Thomas Nieddu, Dr. Kristoffer Karlson and Ratnesh Kumar Gupta have always been there to make experimental hours more enjoyable and pleasant. I would like to extend my thanks to Dr. Vandna Gohkroo, Dr. Jesse Everett and Dr. Georgiy Tkachenko for working closely with me on different projects. I extend my gratitude to all rotation students, intern students and postdocs who worked in the cold atom lab during the common time period especially Jinjin Du, Wenfang Li, Maria Langbecker, Shicheng Zhang, Sanele Dlamini, Mayuri Kawale, Lewis Bartos Picard, Lewis Ruks, Antoine Pichené, Muhammad Hasan Sirajul, René Henke and Tai Tran. I thank all members of the Light-Matter Interactions for Quantum Technologies Unit for making my PhD life a lot easier by helping me when I got stuck in my research. I would like to thank Ms. Emi Nakamura, our research unit administrator, for helping with all the experimental parts orders and being there for me to deal with all paper works and who made my business trips less stressful.

I am indebted to my mother Mrs. Rajasree, who always supported my dreams. I would like to thank my teachers from school and university for motivating me. I thank all my friends especially Xue Han, Yafei Mao, Harsha Paroor, Dinesh Yadav, Anjana Krishnadas, Touseef Haider, Intu Sharma, Maki Maeda, Rashi Sachdeva, Vikas Remesh, Santanu Mondal, Farzana Rahman, Houshu Hiyane, Jameesh Keloth, Vu Hong Le, Aysen Gurkan Ozer, Metin Ozer, Keerthy Menon, Ipsita Herlekar and Nikhil Santh who were there along by my side this PhD journey, making my days joyful. Thanks a lot.

Abbreviations

AOM	Acousto-optic modulator
CCD	Charge coupled device
CF	Conflat
CW	Continuous wave
DM	Dichroic mirror
EIT	Electromagnetically induced transparency
EOM	Electro-optic modulator
FL	Optical filter
FWM	Four-wave mixing
HC-PCF	Hollow core photonic crystal fibre
HWP	Half-wave plate
LP	Linear polariser
MOT	Magneto-optical trap
OM	Optical molasses
ONF	Optical nanofibre
PBS	Polarising beam splitter
PMF	Polarisation maintaining fibre
PMT	Photomultiplier tube
QWP	Quarter-wave plate
SM-ONF	Single-mode optical nanofibre
SPCM	Single photon counting module
StFWM	Stimulated four-wave mixing
TMP	Turbo molecular pump
TOF	Tapered optical fibre
TPA	Two-photon absorption
UHV	Ultrahigh vacuum
VR	Variable retarder

Nomenclature

A	Mode area
\mathbf{B}	Magnetic flux density vector
C_6	Van der Waals coefficient
\mathbf{D}	Electric displacement vector
\mathbf{E}	Electric field vector
E	Binding energy
F	Total angular momentum quantum number
G	Phase matching factor
\mathbf{H}	Magnetic field intensity vector
H	Hamiltonian
I	Nuclear spin
I	Field intensity
I_s	Saturation intensity
I_l	Modified Bessel functions of the first kind
J	Electronic total angular momentum quantum number
J_l	Bessel function of the first kind
K_l	Modified Bessel functions of the second kind
L	Orbital angular momentum quantum number
L	Hot zone
L_{MOT}	Loading rate of atoms to the trap
L_{eff}	Effective length of field overlap
M_i	Mueller matrix
$N, N_b, N_{\text{atoms}}, N_{\text{MOT}}, N_0$	Number of atoms
N_{counts}	Count collected by the camera
\mathbf{P}	Dielectric polarisation
P	Power
P_{ij}	Photon transition rate between i^{th} and j^{th} level
R'	Specific Rydberg constant for the element
R_B	Blockade radius
S_i	Stokes parameters
T, T_{cloud}	Temperature
V	V-number
V	Trapping volume
$V(r)$	Interaction energy between atoms
Y_l	Bessel function of the second kind
Z	Charge of the nucleus

a	Radius
d	Diameter
i	$\sqrt{-1}$
k, k_0, k_1, k_2	Wavenumber
l, m	Order of modes
m_a	Atomic mass
m_n	Mass of nucleus
n	Density of atoms
n_1, n_2	Refractive index of fibre core, cladding
\mathbf{n}, \mathbf{n}^*	Principal, effective principal quantum number
p	polarisation index
r_0	Untapered fibre radius
$r(z)$	Local radius of the taper
s	Spin quantum number
t, t_{exp}	Time
\mathbf{u}	Unit polarisation vector
\bar{v}	Average speed of atoms
v_c	Capture speed
z_b	Beat length of the modes
z_t	Tapering length
\mathcal{A}	Atoms in and out of the interaction region
\mathcal{E}_i	Amplitude of the electric field
\mathcal{L}	Lindblad operator
\mathcal{P}	Factor for the proportion of atoms in MOT and evanescent field
α_i	Absorption coefficient
$\alpha_J^{(0)}$	Reduced scalar two-photon susceptibility coefficient
β	Propagation constant
Γ_{ij}	Natural linewidths
Γ_R	Linewidth of Rydberg state
Γ_i, Γ	Decay rates
$\gamma_{ml}, \gamma_R, \gamma_t$	Loss rates
Δ	$\Sigma_1 - \Sigma_2$
$\delta, \delta_{1,2}, \delta_{993}, \Delta, \Delta_p, \Delta_r$	Laser detuning
δ_R	Quantum defect
ε	Dielectric permittivity
η	Quantum efficiency
Θ	Solid angle
κ	$\sqrt{k^2 - \beta^2}$
λ	Wavelength
μ	Magnetic permeability
ξ	Factor which expresses intensity and polarisation dependency features of the two-photon process
Σ_1, Σ_2	Brightness sum
Σ	$\Sigma_1 + \Sigma_2$
σ	Atomic cross-section

σ^+, σ^-	Polarisation of light: left or right circular polarisation
σ_{ij}	Density matrix elements
σ	Helicity parameter
χ	Electric susceptibility
$ \psi\rangle$	Wave function
Ω_R, Ω_i	Rabi frequency
Ω_r, Ω_p	Effective Rabi frequency
Ω_z	Tapering angle
ω_i	Angular frequency of light
ω_{ij}	Atomic transition frequency between i^{th} and j^{th} level
x, y, z	Cartesian co-ordinates
r, ϕ, z	Cylindrical co-ordinates
e	Electronic charge (1.602×10^{-19} C)
h	Planck constant (6.626×10^{-34} m ² kg s ⁻¹)
\hbar	Reduced Planck constant (1.055×10^{-34} m ² kg s ⁻¹)
k_B	Boltzmann constant (1.3806×10^{-23} m ² kg s ⁻² K ⁻¹)
m_e	Mass of electron (9.109×10^{-31} kg)
R_y	Rydberg constant (10973731.6 m ⁻¹)
ϵ_0	Vacuum dielectric permittivity (8.854×10^{-12} F m ⁻¹)

Contents

Declaration of Original and Sole Authorship	iii
Abstract	v
Acknowledgements	vii
Abbreviations	ix
Nomenclature	xi
Contents	xv
List of Figures	xvii
1 Introduction	1
1.1 Optical Nanofibres	2
1.2 Optical Nanofibre as an Atom Interface	2
1.3 Rydberg Atoms	5
1.4 Rydberg Atoms near Surfaces	8
1.5 Thesis Layout	10
2 Theory	13
2.1 Atom-Light Interactions	13
2.1.1 Ladder-Type Atomic Systems	14
2.2 Electromagnetically Induced Transparency	16
2.3 Two-Photon Absorption	17
2.4 Rydberg Atoms	19
2.5 Conclusions	22
3 Experimental Details	25
3.1 Single-Mode Optical Nanofibres	25
3.2 Optical Nanofibre Fabrication And Installation	26
3.2.1 Adiabatic Condition	27
3.2.2 Fibre Pulling Rig	28
3.2.3 Optical Nanofibre Fabrication	29
3.3 Ultrahigh Vacuum System	31

3.3.1	Mounting the Optical Nanofibre	32
3.4	Cold Atomic Ensemble of ^{87}Rb	33
3.5	Characterisation of the ^{87}Rb Atom Cloud	37
3.6	Fluorescence Signal Coupled to the ONF	41
3.7	Conclusions	43
4	Cold Rubidium Rydberg Atoms near an Optical Nanofibre	45
4.1	Vapour Cell Rydberg EIT and Step Scanning with EOM Sideband Locking	46
4.2	Trap Loss Studies with 29D Rydberg Atoms	49
4.3	Trap Loss Studies with 31S Rydberg Atoms	56
4.4	Dual-Scan Rydberg EIT in Cold Atom-ONF System	56
4.4.1	Free-Space, Dual-Scan Rydberg EIT Experiment	58
4.4.2	ONF-Based, Dual-scan Rydberg EIT Experiments	60
4.5	Conclusions	61
5	Single-Frequency, Two-Photon Transition in Rubidium using 993 nm	65
5.1	S \rightarrow S Two-Photon Transition in Rubidium	65
5.2	Single-Frequency, Two-Photon Spectroscopy in a Rubidium Vapour Cell	66
5.3	Single-Frequency, Two-Photon Spectroscopy in a MOT-ONF system . .	69
5.4	Polarisation Control by Imaging for an ONF Installed in a Vacuum Chamber	73
5.4.1	Verification of Polarisation Control using a Spin-Selection Rule .	74
5.5	Conclusions	79
6	Stimulated Four-Wave Mixing in a MOT-ONF System	81
6.1	Four-Wave Mixing	81
6.2	Experimental Details	82
6.3	Results and Discussion	85
6.4	Conclusions	89
7	Conclusions and Outlook	91
	Bibliography	93
A	Modes in Optical Nanofibres	107
A.1	Eigenvalue Equations from Maxwell's Equations	107
A.2	Electric Field Equations	112
B	Other Published Works	113
B.1	Observation of the ^{87}Rb $5\text{S}_{1/2}$ to $4\text{D}_{3/2}$ Electric Quadrupole Transition at 516.6 nm Mediated via an Optical Nanofibre	113
B.2	Simple, Narrow and Robust Atomic Frequency Reference at 993 nm Exploiting the Rubidium (Rb) $5\text{S}_{1/2}$ to $6\text{S}_{1/2}$ Transition using One-Color, Two-Photon Excitation	123

List of Figures

1.1	Schematic of a typical tapered optical fibre.	3
1.2	Schematic illustration of the collective Rydberg blockade phenomenon.	6
2.1	A three-level ladder system coupled to two lasers.	14
2.2	Coherent and incoherent TPA in a three-level ladder-type system.	18
2.3	Population of the intermediate state and the excited state for coherent and incoherent TPA.	18
2.4	Schematic illustration of the principle of the Rydberg blockade for two atoms.	21
3.1	Effective refractive index as a function of V-number.	26
3.2	Intensity profile of the fundamental mode outside an ONF of radius.	27
3.3	Parameters involved in the adiabatic criterion.	28
3.4	Schematic of the fibre pulling rig.	29
3.5	Transmission through the optical fibre as a function of pulling time.	30
3.6	Illustration of the vacuum system and MOT chamber.	31
3.7	Image of an ONF installed in the UHV chamber.	33
3.8	Energy levels of ^{87}Rb used in the works discussed in this thesis.	35
3.9	D_2 line manifold of ^{87}Rb used for the MOT implementation.	36
3.10	Saturated absorption spectrum of ^{87}Rb D_2 transition.	37
3.11	Optical arrangement for MOT setup.	38
3.12	Sketch of the imaging of the fluorescence of the MOT.	39
3.13	Fluorescence image of the atomic cloud and the loading profile of the MOT.	40
3.14	Detection of MOT fluorescence signal coupled to the ONF.	42
4.1	Two-photon transitions for Rydberg excitation discussed in this chapter.	46
4.2	Vapour cell Rydberg EIT setup.	47
4.3	Vapour cell Rydberg EIT signal.	48
4.4	Saturated absorption spectrum and error signal with EOM on and off.	48
4.5	Experimental setup for trap loss studies for Rydberg atom detection	49
4.6	Simplified ^{87}Rb energy diagram for Rydberg excitation.	50
4.7	Typical experimental output for trap loss studies.	51
4.8	Dependence of the population loss rates on the 482 nm laser detuning, Δ , for a fixed detuning of the 780 nm laser	52
4.9	Dependence of the population loss rate on the 482 nm laser detuning, Δ , for three different detunings of 780 nm laser.	53

4.10	The dependence of γ_R for the coherent and incoherent excitation on the power of the 482 nm pump laser	55
4.11	MOT decay curve when Rydberg laser is locked to the $31S_{1/2}$	57
4.12	Experimental sequence for the dual-scan Rydberg EIT experiments.	59
4.13	Schematic of the free-space, dual-scan Rydberg EIT experiment.	59
4.14	Typical free-space, dual-scan Rydberg EIT spectrum obtained.	60
4.15	The dependence of the EIT ratio peaks as a function of the 482 nm pump power.	61
4.16	Dual-scan experiment curve when probe is guided through ONF while 480 nm is through free-space.	62
4.17	The dependence of 780 nm transmission through ONF for different pump powers.	62
5.1	Energy level diagram for the 993 nm two-photon absorption between $5S_{1/2}$ and $6S_{1/2}$	67
5.2	Schematic of the vapour cell Doppler-free, two-photon spectroscopy setup.	68
5.3	Typical spectroscopic signals obtained by scanning the frequency of the 993 nm pump beam.	69
5.4	Experimental setup for 993 nm spectroscopy in MOT-ONF system.	70
5.5	Evidence of ONF-mediated, two-photon excitation in cold atoms.	71
5.6	High power discrepancies in 993 nm spectroscopy signal.	72
5.7	Linear dependence of the separation between the split peaks on the power of the 993 nm.	73
5.8	Imaging system used for polarisation identification and the polarisation compensation setup.	75
5.9	Schematic of the optical setup for polarisation dependence study.	77
5.10	The variation of the normalised Stokes' parameters during the heating stage.	78
5.11	Polarisation dependence of the 795 nm fluorescence.	78
6.1	Energy level diagram relevant to the stimulated four-wave mixing.	83
6.2	Simplified experimental schematic for stimulated four-wave mixing.	84
6.3	Signature of the stimulated four-wave mixing in MOT-ONF system.	84
6.4	The maximum forward photon count and reverse 795nm photon count as a function of increasing seed laser power.	85
6.5	The forward and reverse 795 nm spectra for lower seed laser power.	86
6.6	The forward and reverse 795 nm spectra for higher seed laser power.	86
6.7	The maximum forward photon count and reverse 795nm photon count as a function of increasing 993 nm laser power.	87
6.8	The forward and reverse 795 nm spectra for lower 993 nm laser power.	88
6.9	The forward and reverse 795 nm spectra for higher 993 nm laser power.	88
6.10	The variation of the polarisation of the generated FWM 795 nm light and seed 795 nm light.	89

Chapter 1

Introduction

The last few decades have witnessed exciting developments in quantum computing in different platforms like superconductors, trapped ions, semiconductors, atoms. Among those, the neutral atom's role is noteworthy [5–7]. Neutral Rydberg atoms, whose outer electron is in a highly excited state, exhibit exotic features like long lifetime, huge dipole moment, etc. With these properties, Rydberg atoms have emerged as leading candidates for neutral atom based quantum information processing [8–11], quantum simulations [12–14], quantum optics [15] and for sensing applications [16]. The long-lived quantum states and the precisely tunable dipolar interaction, leading to Rydberg blockade [17], can be used to prepare a mesoscopic atomic ensemble exhibiting quantum correlations and entanglement [18]. Such systems have already been used to demonstrate a quantum phase gate [19] and simulator [14] in free-space.

Interfacing interacting Rydberg atoms with micro-fabricated components is a very attractive choice for building compact and scalable hybrid quantum devices. As the development of neutral atom based quantum devices unfolds many perspectives in quantum simulation and computing, imagine if we could develop a way to exploit some of the unique properties of neutral atoms to build quantum networks that are easily integrated with the existing optical fibre network. While the component technologies may exist, the combination of neutral atoms and optical fibres has been a challenge and, once overcome, it could significantly increase the viability of atom-based quantum communication.

In this work, we explore controlling neutral, cold rubidium atoms via the evanescent field from optical nanofibres (ONF) to increase the range of phenomena that can be studied. This includes ground state and highly excited (Rydberg) atoms, using two or multiphoton processes, with the overall aim of creating and detecting Rydberg atoms next to ONFs for quantum information processing. Optical nanofibres are interesting because atoms in the evanescent field region are intrinsically coupled to an optical bus in the form of the fibre-guided mode. ONF-based atomic systems could be an excellent platform to study how Rydberg atoms can be controllably manipulated at vacuum-solid state interfaces. This could lead to low-loss transfer of information to and from the interaction region [20], a prerequisite for Rydberg-based quantum repeaters in fibre-coupled cavities [21].

In this chapter, we introduce ONFs and their advantages are explained. A comprehensive description of the state-of-the-art of the "nanofibre+neutral atom" system is

discussed, focussing on multiphoton processes, nonlinear optical process and neutral atom trapping mediated with the ONF evanescent field. Then we discuss Rydberg atoms and their exotic properties. Advances of research in the field of Rydberg atoms next to surfaces is given in the following section. The last section of this chapter provides the overall aim and layout of this thesis.

1.1 Optical Nanofibres

A conventional step index optical fibre, tapered down to hundreds of nanometres or approximately half the wavelength of light propagating through it, is termed as an ONF. In ONFs with a diameter smaller than the wavelength of the guided light, a significant portion of the guided light propagates outside its physical boundary. Another attractive property is that the light guided in the nanofibre is confined in a small volume leading to a very high evanescent field intensity. These fibres also have the distinct advantage of being readily integrated into experimental setups, due to the ease with which light can be coupled into and out of them using standard optical fibre components.

ONFs are usually prepared by heating a commercially available optical fibre to a temperature close to the glass softening point. At this temperature, the stripped region of the fibre can be elongated to the desired dimension without breaking. A typical schematic of a tapered optical fibre (TOF) is given in Fig. 1.1. The tapered optical fibre has three distinct regions: the pigtail, the transition region and the nanofibre/waist region. The pigtail is the unmodified initial fibre used for tapering and used to connect to other fibre components. In this region, the light is weakly guided in the core of refractive index, n_1 . Typically for silica (SiO_2), the core refractive index $n_1 = 1.46$ and the cladding refractive index (n_2) is 1.45, thereby ensuring that total internal reflection and the weakly guiding conditions are met. The transition region is where the fibre radius is reduced along the transition region length until the desired waist diameter is obtained. The tapering process is controlled so that the diameter changes adiabatically in the taper region, ensuring high transmission. The adiabatic condition is explained in detail in Chapter 3.2.1. The cladding in the pigtail becomes the core in the nanofibre region, and the surrounding medium acts as the cladding. When the tapered optical fibre is placed in vacuum, the refractive index difference of core and cladding in the nanofibre is approximately 0.45, thereby the light is propagating under the strongly guiding regime. The details of our fabrication method is given in the Chapter 3.2.3.

1.2 Optical Nanofibre as an Atom Interface

ONFs can be used in both cold and hot (vapour) atom experiments to study atom-light interactions. For example, ONFs have been used in an atomic vapour to observe nonlinear optical phenomena with low optical powers [22–26]. On the other hand, using ONFs with cold atoms trapped initially in a magneto-optical trap (MOT) opens up a wealth of exploration options in areas such as 1D quantum networks. The general MOT scheme uses laser cooling to reduce the average kinetic energy of an ensemble of atoms. The last decades have witnessed major advances in atomic physics with the help

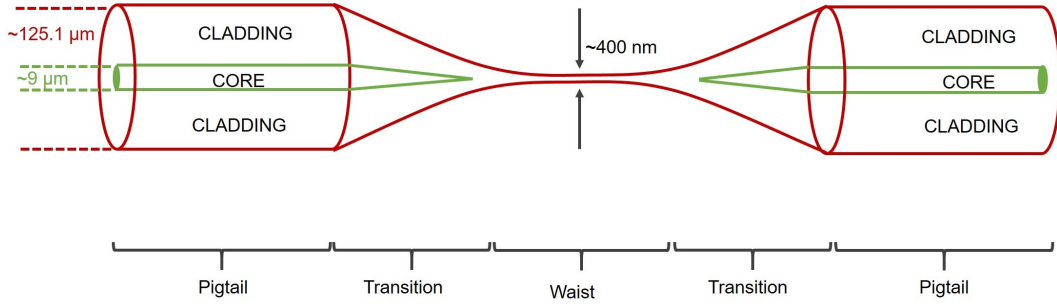


Figure 1.1: Schematic of a typical tapered optical fibre. The nanofibre is the region where the diameter of the fibre reduces to a few hundreds of nanometres. In the transition region the commercial fibre’s diameter ($\sim 125 \mu\text{m}$) is reduced to a minimum diameter $\sim 400 \text{ nm}$. Typical dimensions of the core, cladding and waist of single-mode fibre are given.

of laser cooling and trapping techniques to control the internal and external degrees of freedom of an atom. The average temperature of an atomic ensemble is a measure of the average kinetic energy, which is proportional to the velocity. Hence, by controlling the velocity of atoms the temperature can be controlled. More general details regarding laser cooling and magneto-optical trapping of atoms can be found in [27] with details of our system in Chapter 3. The atom cloud is formed in a MOT and is then overlapped with an ONF so that light travelling through the fibre interacts with the atoms. The ONF can be inserted into the MOT with minimal disturbance to the cooling beams. Here, the temperature of the atoms are typically hundreds of μK , whereas the ONF is at room temperature or even higher when light is propagating through it. This creates an excellent system which can be used to transfer information directly from the light:atom interaction site at the nanofibre waist to the output pigtail.

Properties of atoms in the vicinity of a dielectric surface are well-studied [28–30]. The issue of scattered light by an atom near an ONF has been addressed in [31, 32]. The ONF was demonstrated to collect the light spontaneously emitted from the atoms; a significant amount of photons can be coupled to the guided modes of the ONF. For example, theoretically the collection efficiency for light emitted from a ^{133}Cs atom on an ONF was found to be 28% [33]. This was experimentally demonstrated in [34]. The presence of the ONF also modifies the decay rates depending on the relative distance between the atom and fibre [35]. At short distances, the potential is governed by van der Waals interactions, *i.e.*, $\leq \lambda/10$ (λ is the transition wavelength) and Casimir-Polder interactions at long distances describe the total surface potential producing asymmetries in the fluorescence spectrum. In a MOT-ONF system, the van der Waals force makes important contributions to the modification of the atom’s properties; the Casimir-Polder force is negligible [30, 36]. This interaction manifests as a red-shifted asymmetry in the fluorescence spectrum [37]. Later, it was experimentally shown that the effect of the surface can be reduced by using a violet laser in the presence of the MOT [29]. It was observed that the ONF transmission reduced due to atom adsorption on the surface, but was recovered by sending light of μWs of power [38, 39] through the fibre. One of the factors that can influence the ONF performance is charge accumulation. In Ref. [40], the authors provided an estimate of the surface charge density of a ta-

pered fibre with a diameter of $1.6 \mu\text{m}$ to be $4 \times 10^{-6} \text{ C/m}^2$ using charged particles in a linear Paul trap. This is expected to decrease as the fibre diameter is reduced. Most studies related to such measurements have been conducted by the ion trapping community, who are keen to use tapered optical fibres as information transfer channels for quantum networks. There are also ongoing studies on coated ONFs to reduce these surface charges. In addition, there could be light-induced charges on the dielectric material [41].

When on-resonant light is guided through the ONF, it interacts with atoms in the vicinity of the waist. The interaction strength between an atom with a photon is dependent on the ratio σ/A , where A is the mode area and σ is the atomic cross-section. The light carrying the interaction signature then couples back to the fibre. The emission rate gets enhanced by the cooperativity of the atoms via the guided modes of the ONF. The efficiency of coupling of emission into the guided modes increases with increasing atom number and approaches unity for a large number of atoms [42]. An example of active probing using an ONF is absorption spectroscopy, obtained by launching resonant laser light through the fibre. Various such experiments carried out with a MOT-ONF system have been reviewed [43, 44]. This probing technique was used to find MOT characteristics such as temperature [45] and lifetime [46].

In 2004, it was proposed that the evanescent field from an ONF could also be used to create a gradient trap. This ONF-based gradient trap was shown to trap neutral atoms around the waist of an ONF, when red-detuned light propagates through the fibre [47]. The red-detuned light creates an attractive potential, thus bringing atoms towards the fibre surface. For ONFs whose diameter is about half the wavelength of the propagating light, this potential can be counterbalanced by the centrifugal force acting on the atoms, thus the atoms are trapped. The fibre trapping scheme was further improved by considering a two colour trap: blue-detuned light, along with the red-detuned light, could be used to repel atoms from the surface of the ONF [48], preventing atoms from sticking to the fibre. The two-colour scheme was experimentally realised when ^{133}Cs atoms were successfully trapped around an ONF [49, 50]. The polarisations of the detuned beams were orthogonal to achieve confinement in the azimuthal direction. The spectral properties of atoms showed an asymmetric behaviour, pointing to the fact of state dependent light shifts induced by the trapping light. This can be solved by detuning to magic wavelengths, which was shown in [51]. Further experimental progress with this system is well-explained in [52–54]. The nanofibre-trapped atomic ensemble has the advantage that collisional broadening and motional dephasing is absent, thereby improving the signal quality [55]. In Ref. [49, 56], the authors employed dispersion based measurements in the nanofibre trapped atoms, by sending a non-resonant probe beam through the ONF. While aforementioned traps utilise the fundamental modes, there are theoretical studies to use higher order modes for trapping [57, 58].

Once the basic characteristics of cold atoms were observed via an ONF, the research diversified by including other quantum emitters such as quantum dots near or on the fibre surface [59–61]. Interactions were also enhanced by creating cavities on the ONF, with the cavity mirrors either outside of the fibre or inside the taper region of the fibre [62, 63]. The strong confinement and long interaction length along the ONF makes it an attractive platform to perform quantum nonlinear optics. Electromagnetically

induced transparency (EIT) is an optical technique through which absorption of light by atoms is modified. EIT has influenced fundamental and applied atomic physics research and a detailed review is given in Ref. [64]. The transparency is obtained as a result of atom-light interactions where the absorption of light by an atomic medium gets modified in the presence of another intense light beam. One of the requirements to realise EIT is two optical fields addressing two transitions, one of which is of higher power than the other; the transition requiring higher intensity is usually named as the pump and that of lower intensity is mentioned as the probe beam. Note that the pump is sometimes referred to as the control beam. A detailed theoretical discussion on EIT is given in Chapter 2.

Theoretically, it was shown that EIT and one of its applications, slowlight, could be realised in the cold atom-ONF hybrid system [65]. In 2015, the EIT phenomenon was demonstrated using an ONF [55, 66, 67]. A research group in Laboratoire Kastler Brossel, France successfully implemented this technique to demonstrate an optical memory at the single-photon level and slow light using ^{133}Cs [67]. In Ref. [55], EIT and slow light were studied along with the storage of fibre-guided optical pulses in ONF trapped caesium atoms.

1.3 Rydberg Atoms

Rydberg atoms are neutral atoms where the valence electrons are in a high principal quantum number state (\mathbf{n}), thence it has a large orbital radius. The outermost electrons are far away from the core by a factor of 100-1000 compared to ground state atoms, leading to enhanced polarisability [68]. This also leads to an increase in the induced dipole moments and strong long-range dipole-dipole interactions. The properties of Rydberg atoms depend on the principal quantum number of the Rydberg state. Typically, experiments are carried out with the principal quantum number ranging from 10-200. Alkali Rydberg atoms are attractive to study because of their hydrogen-like structure, with deviation occurring from the simple hydrogen model due to the difference in the core electrons. We elaborate on the properties of Rydberg atoms in Chapter 2.

Many reviews on Rydberg atoms address their extraordinary properties [10, 69, 70]. The advantage of using neutral Rydberg atoms over ions or other systems as qubits is their state-dependent properties. Noninteracting atoms in the ground state address the requirement of the long storage time and, when they are excited to Rydberg levels, they can be strongly interacting and the strength depends on the level to which they are excited. Hence, exciting and de-exciting neutral atoms to Rydberg levels with resonant photons makes them an excellent tool to implement quantum logic [10, 71].

Interactions among Rydberg atoms at large distances is a van der Waals interaction and at smaller distances a dipole-dipole interaction. One of the pronounced effects of the interaction between highly excited atoms is the blockade effect. Here, the Rydberg energy state is shifted out of resonance with respect to the exciting laser due to interaction with a neighboring Rydberg atom. If we consider a volume of atoms, we can define a blockade radius as the radius within which only one Rydberg excitation is possible. This modification in excitation was reported in [72]. The blockade process

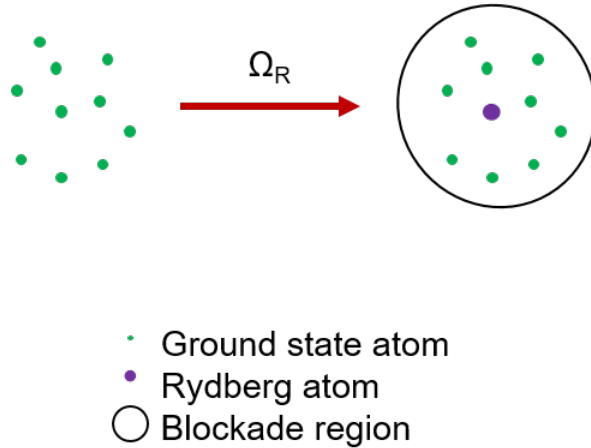


Figure 1.2: Schematic illustration of the collective Rydberg blockade phenomenon. Consider an ensemble of N - two-level non-interacting atoms. If they are excited with a coupling strength, Ω_R , they exhibit Rabi oscillations of frequency Ω_R . When the atoms are separated by a distance less than the blockade radius, effectively one excitation is possible with a modification to the Rabi frequency.

leads to enhancement of the Rabi oscillation by a factor of $\sqrt{N_b}$, where N_b is the number of atoms within the volume described by the blockade radius (see Fig. 1.2).

This strong interaction between neutral Rydberg atoms leads to collective entanglement of the atoms, making them an interesting candidate for photonic quantum devices [10]. The collective entanglement of Rydberg atoms was experimentally studied using an ultracold atomic ensemble [17]. Rydberg blockade also leads to a quantum phase transition to a crystalline phase of Rydberg excitation [73]. Rydberg blockade was also used for creating a single photon source [74]. It was theoretically proposed [8] and experimentally realised that C-NOT gate [19] protocols can be performed using Rydberg blockade.

Any application of Rydberg atoms requires the ability to coherently excite from the ground level to the Rydberg level. Most of the Rydberg based experiments are performed using cold atoms [75], which facilitate the process due to negligible Doppler effects and the ease of preparation of atoms in a specific quantum state. The density of the atomic ensemble also plays a crucial role in Rydberg experiments [69]. The dipole matrix elements for Rydberg level excitation is very small, hence, the laser light used for Rydberg excitation has to be intense and narrow in frequency. Many schemes use lasers of hundreds of mWs for Rydberg excitation. Generally, for rubidium, single-photon excitation to a Rydberg level occurs at 297 nm [76]. This single photon excitation sets the requirement for a stable light source around 300 nm, often an inconvenient wavelength without dye lasers. Therefore, two-photon excitation is generally used to excite to Rydberg levels, shifting the wavelength of excitation to one which is achievable using diode lasers and this is the method adopted in this thesis work.

The most common used detection technique for Rydberg atoms is the multi-channel plate or channeltron. A multi-channel plate detects the ions, which are produced by applying an electric field or far infrared pulses to the Rydberg atoms. Friedler *et*

al. proposed coupling the excited state in a lambda (Λ) EIT scheme to a highly excited Rydberg state [77]. They showed that one could transfer the strong interactions between Rydberg atoms onto the optical transition and thereby realise a photonic phase gate. The Rydberg atom community, which heavily depended on the destructive methods subsequently, started focussing on the EIT methods to study and detect Rydberg atoms. In 2007, Rydberg-EIT was successfully observed [78]. This Rydberg detection method has a handful of advantages such as being non-destructive; hence, the atom can be reused and it can be used to detect Rydberg atoms in confined geometries. In Rydberg EIT, similar to normal EIT, two lasers, a pump and probe, are used. This technique finds applications to study the interaction between Rydberg gases and enhances the nonlinear properties of Rydberg atoms [79–85]. In Ref. [86], the authors utilised Rydberg EIT to image individual Rydberg atoms. Note there are numerous optical and non-destructive techniques other than EIT to detect and study the Rydberg atoms. There are several proposals and demonstrations of multiphoton processes to detect and study the properties of the Rydberg levels [87–91]. The advantage of relying on multiphoton processes mediated by a Rydberg level is that the multichannel nature of the multiphoton process allows for multichannel information processing related to Rydberg states. There is another category of detection technique which relies on the loss of the atoms in the atomic ensemble as a result of Rydberg excitation so that the Rydberg atom excitation can be imaged [92] or studied [93, 94]. In our work, we focussed on using optical methods for detection since, applying an electric field for ionisation could damage the ONF.

In most experiments using cold atoms, the trapping lasers are switched off during the Rydberg excitation. The trapping force in an optical lattice is the spatial modulation of the light shift by interference of the lasers with frequencies around the transition between the trapped atomic ground state and another bound excited state. It has been proposed to use ponderomotive optical lattices for trapping Rydberg atoms [95]. This method claims that the polarisability of the Rydberg transition is negative, therefore different from the ground state, leading to ground state lattice potential minima coinciding with the Rydberg state potential maxima. In Ref. [96], the authors proposed that inverting the lattice soon after the Rydberg excitation would eventually lead to the potential minima near the initially prepared Rydberg atoms. The atom is trapped entirely due to the weak Coulomb binding of the atomic nucleus to the trapped Rydberg electron. This proposal was experimentally realised with a higher trapping efficiency [96] than earlier methods. Subsequently Zhang *et al.* proposed a blue-detuned trap, which exhibits dipole trapping for both the Rydberg and neutral atom [97]. They studied different geometries where both the neutral and Rydberg atoms can be trapped. Recently, Barredo *et al.* [98] experimentally demonstrated three dimensional trapping of Rydberg atoms utilising optical bottle beam traps. Aside from the above experiments, there are steps towards using magnetic fields to create microtraps to trap Rydberg atoms [99].

1.4 Rydberg Atoms near Surfaces

Since this thesis work has as a primary aim the creation of Rydberg atoms next to an ONF, we need to consider the effect of the dielectric surface on the atom's lifetime. It is already known that the Rydberg atoms, with their very large polarisability, can interact strongly with nearby surfaces. This strong interaction is widely used in surface physics [100], quantum information [101], etc. Previously, a metallic surface placed near a Rydberg atom was used to study the Casimir-Polder effect [102–104]. Theoretical calculations showed that the interaction between the metal surface and a Rydberg atom leads to energy level shifts on the order of GHz [104].

Micro/nano cells are an alternative platform where atoms close to surfaces are studied [105, 106]. They are excellent systems to probe atom-atom interactions as well the atom-surface interactions. One of the initial steps to study Rydberg atoms near surfaces was to excite a thermal vapour of ^{87}Rb to Rydberg levels in a microscopic cell [107]. In the experiment, the authors used the Rydberg EIT excitation method to excite and detect the Rydberg atoms [107]. The excitation to different Rydberg levels with various cell thicknesses was studied and they showed that the EIT peak position and peak width depend on the cell thickness.

There were also several proposals and experimental developments on atom chip experiments by exciting Rydberg atoms near the surface [108, 109]. In an experiment in this direction, a group of researchers from the University of Amsterdam excited a ^{87}Rb atom cloud to Rydberg levels using the EIT scheme [110] approximately $100\ \mu\text{m}$ away from a gold surface coated with a thin layer of SiO_2 (25 nm). The major challenge was the rubidium adsorbed on the chip surface, creating a stray electric field. UV light was used to reduce this effect and the temperature of the surface was increased by 50 K. This minimised the stray fields by desorbing atoms from the surface. Later Davtyan *et al.*, controlled the electric field by changing the adsorbate distribution with the help of a laser [111]. The laser changes locally the surface dipole distribution through heating and/or a light-induced atomic desorption process. Subsequently Hond *et al.* successfully demonstrated Rydberg blockade in the system [112].

Following the attempts to integrate the Rydberg atoms with surfaces Chougale *et al.* theoretically studied an interesting system of Rydberg excitation in a chain of atoms coupled to a photonic crystal waveguide [113]. They proposed to exploit the locally induced cavity modes to exchange the excitation to nearby ground state atoms. They studied the interaction dynamics behaviour for short and long range, when one of the atoms is in a Rydberg state. They observed complex dynamics when there are two Rydberg excitations in the system and discussed the dissipation process due to spontaneous emission of the atom from the Rydberg level to free space, advising on using higher Rydberg level to reduce the effect.

Hollow-core photonic crystal fibres (HC-PCF) recently became an alternative platform to realise thermal vapour based atomic experiments. Three-photon excitation of caesium vapour to Rydberg levels in HC-PCF has been experimentally realised [114]. The room temperature maintained caesium vapour was pumped into two different core size HC-PCFs and the experiment was done with high (4 months exposure) and low (2 months exposure) optical density of ^{133}Cs regime. Unexpected level shifts were observed and these shifts disappeared after 4 months exposure. Epple *et al.* attributed

this to a decrease of the charge density or adsorption of the atoms on the core wall. This work was an initial step towards incorporating Rydberg atoms with dielectric waveguides, but the authors could not provide a trend for the behaviour observed. The authors of [115] used the higher order modes to study the distribution and underlying effects of these electric fields. They concluded that the fields are caused by the dipole moments of atoms adsorbed on the fibre.

Although the technique to excite and detect Rydberg atoms might be similar, in cold atoms additional degrees-of-freedom are controlled both internally and externally. Langbecker *et al.* reported on the excitation and detection of cold Rydberg atoms with a resonant two-photon EIT process within a HC-PCF [116]. They observed a shift and broadening of the EIT spectra compared to experiments in free-space. To study the loss dependent process, they introduced a probe pulse after EIT excitation. The EIT and probe absorption signal were quite different for a low repetition number of experimental cycles and the authors termed this as an EIT regime where coherent Rydberg excitation is observed. For a higher repetition number of experimental cycles, they observed the absorption signal follows the EIT signal; this can be due to the atom loss from the Rydberg excitation or ionisation.

Rydberg Atoms near an Optical Nanofibre

By optically exciting Rydberg atoms in the evanescent field of an ONF, they are expected to be a few hundreds of nm from the fibre surface, within the evanescent field region. Aside from endeavours to combine ONFs and ground-state, neutral atoms, work on Rydberg excitation next to ONFs has, to-date, been limited to theoretical proposals due to the difficulty in generating highly excited atom states within a few 100 nm of surfaces, *e.g.* dielectrics or metals, and the problem of induced electric fields - even at distances as large as $\sim 100 \mu\text{m}$ - by adsorption of atoms on the surface [108, 117].

Despite the technical difficulties there are several theoretical papers which studied Rydberg atoms next to an ONF. Stourm *et al.* studied the behaviour of a sodium Rydberg atom next to an ONF of diameter 200 nm [20]. It was found that the spontaneous emission rate from the Rydberg atom coupled into the guided and radiation modes. They concluded that spontaneously emitted light is predominantly coupled to radiation modes over the guided modes of the ONF. They suggested using a thicker fibre with higher order modes to increase the guided mode coupling. Later, the authors studied rubidium Rydberg atoms near an ONF to ensure relevance to experimental efforts [118]. They studied the dependence of the ONF radius and distance from the atom to the fibre on the spontaneous emission coupling to the guided and radiation modes. They showed that the spontaneous emission is amplified in the presence of the ONF. They concluded that, when a Rydberg atom is close to an ONF, there is significant coupling of spontaneously emitted light to the guided modes of the ONF. This is very promising for experimental developments.

Stourm *et al.* also calculated the position dependent Lamb shift, which give rises to a position dependent Casimir-Polder force [118]. They included the possibility of quadrupolar transitions in the de-excitation of the Rydberg atoms. They concluded that the contributions from quadrupolar transitions to the guided modes is negligible,

but the contribution to the Lamb shift is non-negligible. Since the Casimir-Polder force has an attractive nature they concluded, for the typical distances considered, the atom can crash into the fibre producing a huge electric field. Hence the importance of atom trapping for both ground and Rydberg atoms in the system is inevitable to ensure experiments will be viable.

1.5 Thesis Layout

The main focus of this thesis work is to excite and detect Rydberg atoms via the evanescent field of an ONF. As discussed earlier, one of the widely employed optical processes to excite atoms to a Rydberg level is a two-photon excitation. In the first set of experiments discussed in Chapter 4, we detect the presence of Rydberg atoms via atom loss from the trap. In the latter part, we discuss the step-by-step progress to implement the Rydberg excitation and detection with a resonant two-photon EIT scheme with both beams propagating through the ONF. We find that ONF or alternative trapping is inevitable to proceed with further studies. For effective implementation of the nanofibre trapping, one needs full control of the polarisation and intensity of light at the fibre waist. In the ONF-atom system, the polarisation of the light at the waist is difficult information to access, since it is influenced by stress induced by the ferrules, splicing, etc. In typical atomic experiments mediated by an ONF, the polarisation is studied using a Rayleigh scattering method [50, 51, 67] or simply by adjusting the input polarisation such that the light-atom interaction is optimum [119]. Hence, achieving control of the polarisation of the nanofibre-guided light is a significant step in opening new trapping mechanisms for Rydberg atoms, e.g. exploiting the ponderomotive force. We implement a polarisation compensation technique in Chapter 5 for this purpose. To confirm the successful compensation, a polarisation dependent atomic process is studied in the system.

In the second half of the thesis work, we explore two-photon processes to low lying non-Rydberg energy levels where atom ionisation is negligible. As a first step, we study the $5S_{1/2} \rightarrow 6S_{1/2}$ two-photon, single-frequency excitation via a virtual intermediate level in a vapour cell and in the ONF-MOT system. We test polarisation control in the ONF-MOT system by verifying the two-photon transition probability of the $5S_{1/2} \rightarrow 6S_{1/2}$ transition in cold rubidium atoms. One Rydberg atom detection method suggests using an input probe [93] along with two-photon Rydberg excitation scheme to drive a four-wave mixing process. By studying the $S \rightarrow S$ two-photon excitation in the presence of an additional laser we demonstrate the stimulated four-wave mixing in an ONF based atomic system for first time. This could be implemented for Rydberg atom detection in our system. The chapter-wise outline of the thesis is as follows:

Chapter 2: This chapter provides an introduction to light-matter interactions discussed in the course of this thesis work, followed by a discussion of ladder-type three-level systems relevant to our work. Electromagnetically induced transparency and two-photon excitation are explained in detail. We introduce the properties of Rydberg atoms which make them attractive candidates in several fields like quantum simulation, sensing, etc.

Chapter 3: This chapter presents details of the experimental system, *i.e.* the ONF

passing through the cold atom cloud. The method used to prepare the ONF from commercially available fibre and the installation procedure in the vacuum chamber is explained. The experimental techniques to produce the cold atoms are discussed.

Chapter 4: A ladder-type, two-photon excitation scheme [78] is used to excite the atoms to the Rydberg state, and a trap loss method [93] is used to probe the Rydberg excitation. We implement a rate equation model [120] to determine the rate of population transfer to the Rydberg state. Both coherent two-photon excitation and incoherent two-step excitation is demonstrated. A density matrix based model is developed for the three-level, ladder-type system interacting with the evanescent field of the ONF. In the latter half of the chapter, we explain our step-by-step approach implemented to realise Rydberg EIT in optical molasses mediated by the ONF.

Chapter 5: Here, we discuss a single-frequency, two-photon excitation process. We explore the $5S_{1/2} \rightarrow 6S_{1/2}$ transition scheme in rubidium. We study two-photon excitation in a vapour cell and in the MOT-ONF system. We adapt the methods of Tkachenko *et al.* [121] to control the polarisation of light at the ONF waist. This method relies on imaging the scattered light from the fibre surface using a camera and a single lens. We implement the technique to study the selection rule for the $5S_{1/2} \rightarrow 6S_{1/2}$ transition, which is dependent on the polarisation and confirms the compensation technique.

Chapter 6: In this chapter we study a stimulated four-wave mixing process in ^{87}Rb using a seed laser of wavelength 795 nm. The seed laser drives the two-photon excitation (explained in Chapter 5) to drive the four-wave mixing process.

Chapter 7: Finally, a conclusion of this thesis work and an outlook on future experiments are provided .

Chapter 2

Theory

In this chapter, we discuss the theoretical background/modelling used to explain the experimental results. The first few sections revolve around the light-matter interaction based on the three-level system relevant for this work. Later, we focus on the Rydberg atoms especially Rb. We close this chapter with an extensive discussion on properties of Rydberg atoms that make them an excellent tool for quantum simulations.

2.1 Atom-Light Interactions

Let us begin by considering a two-level system with initial state $|1\rangle$ and final state $|2\rangle$. When light interacts, the system makes a transition from state $|1\rangle \rightarrow |2\rangle$, and the optical properties of the medium, such as absorption and dispersion of the light, depend on the electric susceptibility [122]

$$\mathbf{P} = \varepsilon_0 \chi \cdot \mathbf{E}, \quad (2.1)$$

where \mathbf{P} is the dielectric polarization, ε_0 is the vacuum permittivity and \mathbf{E} is the electric field. The susceptibility is defined as $\chi = \chi' + i\chi''$, where the absorption of the light by the medium is described by the imaginary part of the susceptibility and the real part gives the dispersion of the light. Equation 2.1 is valid when the intensity of the interacting light is weak. When the intensity of the interacting light is not weak, the optical susceptibility is expanded as a power series [122]

$$\chi = \chi_1 + \chi_2 \cdot \mathbf{E} + \chi_3 \cdot \mathbf{E}\mathbf{E} + \dots, \quad (2.2)$$

where χ_1 is the linear optical susceptibility, which is field independent and a constant for the medium. When the light intensity is high, the susceptibility is no longer constant and is field dependent. The higher order terms give rise to various of nonlinear atom-light interactions. Some of the second order nonlinear effects are second-harmonic generation and optical parametric processes. The third order term contributes to two-photon absorption, third-harmonic generation, four-wave mixing, optical Kerr effect, etc. [123].

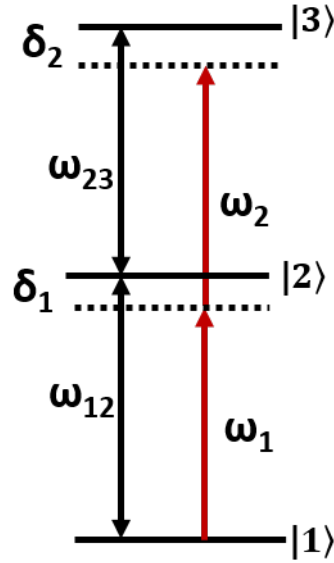


Figure 2.1: A three-level ladder system with ground state $|1\rangle$, intermediate state $|2\rangle$ and excited state $|3\rangle$ coupled with two optical fields of frequency ω_1 and ω_2 , which are detuned from the atomic transitions by δ_1 and δ_2 , respectively.

2.1.1 Ladder-Type Atomic Systems

Three levels can be viewed as being in lambda, V or ladder/cascade configurations. Here, we concentrate on the interaction of light with a ladder-type, three-level atom. Ladder-type atomic systems are attractive platforms for multiphoton process [107], atomic filters [124] and to access Rydberg levels [10, 125]. Two-photon spectroscopy and EIT are two well-known and widely used spectroscopic techniques used to study ladder systems.

Consider an atom with ground state $|1\rangle$, intermediate state $|2\rangle$ and excited state $|3\rangle$. Let us consider the levels to be represented by three quantum numbers $|\mathbf{n}_i, J_i, L_i\rangle$, $i = 1, 2, 3$, where \mathbf{n}_i is the principal quantum number, L_i is the orbital angular momentum quantum number and J_i is the total angular momentum quantum number. The states are separated by energies $\hbar\omega_{12}$ and $\hbar\omega_{23}$. Let us assume that the transition $|1\rangle \rightarrow |2\rangle$ is initiated with the optical field, $\mathcal{E}_1 \cos(\omega_1 t)$, of Rabi frequency Ω_1 . The transition $|2\rangle \rightarrow |3\rangle$ is addressed with the optical field $\mathcal{E}_2 \cos(\omega_2 t)$ and of Rabi frequency Ω_2 . The detunings of the optical field from the atomic transition frequencies are $\delta_1 = \omega_{12} - \omega_1$ and $\delta_2 = \omega_{23} - \omega_2$. Figure 2.1 shows a ladder configuration three-level atom.

Optical Bloch equations

The dynamics of the system can be calculated using the Schrödinger equation in the absence of decoherence given by

$$i\hbar\frac{d|\psi\rangle}{dt} = H|\psi\rangle, \quad (2.3)$$

where H is the Hamiltonian of the system and $|\psi\rangle$ is the wave function. The real atomic levels exhibit a finite lifetime, hence the dissipative process should be accounted for. Hence, we rely on the time evolution of the density matrix (σ_{ij}) where the dissipation terms can be included. The three-dimensional density matrix is given by

$$\sigma_{ij} = \begin{bmatrix} \sigma_{11} & \sigma_{12} & \sigma_{13} \\ \sigma_{21} & \sigma_{22} & \sigma_{23} \\ \sigma_{31} & \sigma_{32} & \sigma_{33} \end{bmatrix}. \quad (2.4)$$

In Eqn. 2.4, the diagonal elements give the populations and the off-diagonal elements are the atom-light coupling coherences. Using Liouville's theorem, the time evolution of the density matrix can be written as

$$i\hbar\dot{\sigma}_{ij} = [H, \sigma_{ij}]. \quad (2.5)$$

The decoherence or dissipative process is added to Eqn. 2.4 by introducing the Lindblad operator (\mathcal{L}). Thus, the time evolution of the density matrix or the optical Bloch equation is

$$i\hbar\dot{\sigma}_{ij} = [H, \sigma_{ij}] + i\hbar\mathcal{L}. \quad (2.6)$$

To solve Eqn. 2.6, the Hamiltonian and the Lindblad operator for the three-level system under consideration are required. The Hamiltonian of the coupled system is given by $H=H_0+H_I$. H_0 , is the Hamiltonian of the bare atom without any external fields. H_I is the interaction Hamiltonian, which describes a perturbation due to the applied field [126]. We have that

$$H = \begin{bmatrix} 0 & \Omega_1 & 0 \\ \Omega_1 & -2\delta_1 & \Omega_2 \\ 0 & \Omega_2 & -2(\delta_1 + \delta_2) \end{bmatrix}. \quad (2.7)$$

The Lindblad operator for a three-level cascade system is the sum of the contribution from both dissipative and dephasing processes. The finite linewidth of the laser increases the dephasing rate of the non-diagonal elements and leaves the population of the levels unchanged. Hence, the Lindblad operator is written as [126]

$$\mathcal{L} = \begin{bmatrix} \Gamma_{21}\sigma_{22} & -\frac{1}{2}\Gamma_2\sigma_{12} & -\frac{1}{2}\Gamma_3\sigma_{13} \\ -\frac{1}{2}\Gamma_2\sigma_{21} & -\Gamma_{21}\sigma_{22} + \Gamma_{32}\sigma_{33} & -\frac{1}{2}(\Gamma_2 + \Gamma_3)\sigma_{23} \\ -\frac{1}{2}\Gamma_3\sigma_{31} & -\frac{1}{2}(\Gamma_2 + \Gamma_3)\sigma_{32} & -\Gamma_{32}\sigma_{33} \end{bmatrix}, \quad (2.8)$$

where the decay rates for the levels $|2\rangle$ and $|3\rangle$ are given by $\Gamma_2 = \gamma_2 + \Gamma_{21}$, $\Gamma_3 = \gamma_3 + \Gamma_{32}$, respectively. The Γ_{ij} are the natural linewidths and γ_i are the dephasing rates. Thus, solving Eqn. 2.6, the obtained optical Bloch equations for a three-level ladder system are as follows

$$\begin{aligned}
\dot{\sigma}_{11} &= \frac{1}{2} [2\Gamma_{21}\sigma_{22} + i(\sigma_{12} - \sigma_{21})\Omega_1], \\
\dot{\sigma}_{22} &= \frac{1}{2} [-2\Gamma_{21}\sigma_{22} + 2\Gamma_{32}\sigma_{33} - i(\sigma_{12} - \sigma_{21})\Omega_1 + i(\sigma_{23} - \sigma_{32})\Omega_2], \\
\dot{\sigma}_{33} &= \frac{1}{2} [-2\Gamma_{32}\sigma_{33} + i(\sigma_{23} - \sigma_{32})\Omega_2], \\
\dot{\sigma}_{21} &= \frac{1}{2} [-\Gamma_2\sigma_{21} + i(2\delta_1\sigma_{21} - \sigma_{11}\Omega_1 + \sigma_{22}\Omega_1 - \sigma_{31}\Omega_2)], \\
\dot{\sigma}_{32} &= \frac{1}{2} [-\Gamma_2\sigma_{32} - \Gamma_3\sigma_{32} + i(2\delta_2\sigma_{32} + \sigma_{31}\Omega_1 - \sigma_{22}\Omega_2 + \sigma_{33}\Omega_2)], \\
\dot{\sigma}_{31} &= \frac{1}{2} [-\Gamma_3\sigma_{31} + i(2\delta_1\sigma_{31} + 2\delta_2\sigma_{31} + \sigma_{32}\Omega_1 - \sigma_{22}\Omega_2)]. \tag{2.9}
\end{aligned}$$

2.2 Electromagnetically Induced Transparency

EIT is one of the optical techniques through which absorption of light by atoms is modified. EIT has influenced fundamental and applied atomic physics research and a detailed review is given in Ref. [64]. The transparency is obtained as a result of atom-light interactions where the absorption of light by an atomic medium gets modified in the presence of another intense light beam. The two dipole-allowed transitions in the ladder-type system are addressed with a strong pump laser ($|2\rangle \rightarrow |3\rangle$) and a weaker probe laser ($|1\rangle \rightarrow |2\rangle$). The pump laser is tuned to the resonant frequency, whereas the probe frequency is scanned across the transition. Consider an atom to be in state $|1\rangle$. On applying probe, the atom can make a transition to $|2\rangle$. When the pump laser, which is resonant to $|2\rangle \rightarrow |3\rangle$ is applied, the atom can decay back either directly to $|1\rangle$ or can follow $|2\rangle \rightarrow |3\rangle \rightarrow |1\rangle$. These pathways destructively interfere under specific conditions and exhibit reduced absorption at the resonance.

Mathematically, in Eqn. 2.9, when the laser addressing the levels $|2\rangle \rightarrow |3\rangle$ is strong, and the population is primarily in $|1\rangle$, *i.e.* $\sigma_{11}=1$, $\sigma_{22} = \sigma_{33} = 0$. The solution for Eqn. 2.9 can be used to find the optical susceptibility. The susceptibility for the EIT probe is given as [76]

$$\varepsilon_0\chi \cdot \mathbf{E} = 2N|\mathbf{d}_{12}|\sigma_{12}. \tag{2.10}$$

Here, \mathbf{d}_{12} is the dipole moment. The absorption of the light passing through the medium is included in the imaginary part of χ . Ladder-type EIT is of growing interest for a variety of applications including the search for Rydberg states [78], photon-pair generation [127], slow light [67], etc. This was previously studied in a cold atom-nanofibre system in our group at OIST [66].

2.3 Two-Photon Absorption

Two-photon absorption (TPA) is a third-order, nonlinear optical phenomenon which is commonly encountered in three-level, ladder-type atomic systems [122]. The atoms are excited to the final state by simultaneously absorbing two photons. It is the simplest case of a multiphoton process. The general selection rule for the two-photon transition is that the transition is allowed only if $\Delta L = 0, 2$ [128]. Hence, the two-photon transition is allowed only if the initial state $|1\rangle$ and the final state $|3\rangle$ have the same parity. This parity rule is a consequence of the odd character of the electric dipolar coupling. Hence, the two-photon process gives access to energy level transitions which are inaccessible with single-photon excitation. The general selection rule for the electronic angular momentum quantum number, J , is that the two-photon transition can be allowed only if $\Delta J \leq 2$ [129–131].

The energy level diagram for a two-photon process is given in Fig. 2.2. In Fig. 2.2(left), the atoms are transferred to the real level $|2\rangle$, *i.e.*, $\delta_1=0$, and then to the excited state $|3\rangle$. The TPA process is shown in Fig. 2.2(right), where the atoms transfer to $|3\rangle$ by absorbing photons of frequencies ω_1 and ω_2 through a virtual intermediate state, $|2\rangle$, which is detuned from a real level by δ_1 . To understand more about the difference between the two processes, let us consider two light fields of the same Rabi frequency ($\Omega_1=\Omega_2=\Omega$). Assuming the population is initially in the state $|1\rangle$, the populations of states $|2\rangle$ and $|3\rangle$ for the two cases are given in Fig. 2.3. Figure 2.3(a) represents the population when both light fields are resonant with the transition corresponding to Fig. 2.2(left). The atoms reach $|2\rangle$ then arrive to $|3\rangle$. The next scenario is when there is non-zero detuning as in Fig. 2.2(right) and the populations are given in Fig. 2.3(b). When there is a detuning, the population reaching $|2\rangle$ is reduced. As long as the two-photon resonance condition is valid, *i.e.*, $\delta_1 = \delta_2$, the population reaches $|3\rangle$. When δ_2 is larger than the Rabi frequency of the fields, we can adiabatically eliminate state $|2\rangle$. A detailed theoretical discussion can be found in [132]. The process can be equated to one photon process from $|1\rangle \rightarrow |3\rangle$ with the Rabi frequency defined by $\Omega^2/2\delta_2$. Therefore, the two-photon process is similar to two one-photon processes and if two-photon coherence is not required, we will refer it as incoherent two-photon absorption in this thesis [133, 134].

The two-photon absorption can be initiated by two photons of the same frequency or different frequencies. We employ the terminology single-frequency TPA, when the two photons have the same frequency to initiate TPA and two-frequency TPA otherwise. Narrowing the discussion to a single-frequency two-photon excitation we have $\omega_1 = \omega_2 = \omega = (\omega_{12} + \omega_{23})/2$, $\mathbf{u}_1 = \mathbf{u}_2 = \mathbf{u}$, and $\mathcal{E}_1 = \mathcal{E}_2 = \mathcal{E}/\sqrt{2}$. The two-photon transition rate, P_{13} , is calculated using second order perturbation theory [135] and can be simplified as

$$P_{13} \propto \frac{1}{\Gamma} |\alpha_J^{(0)}|^2 \xi, \quad (2.11)$$

where Γ is the total decay rate, $\alpha_J^{(0)}$ is the reduced scalar two-photon susceptibility coefficient and the factor $\xi = |(\mathcal{E} \cdot \mathcal{E})|^2 = |\mathcal{E}|^4 |\mathbf{u} \cdot \mathbf{u}|^2$ expresses both of the characteristic features of the two-photon process: the quadratic dependency on the field intensity,

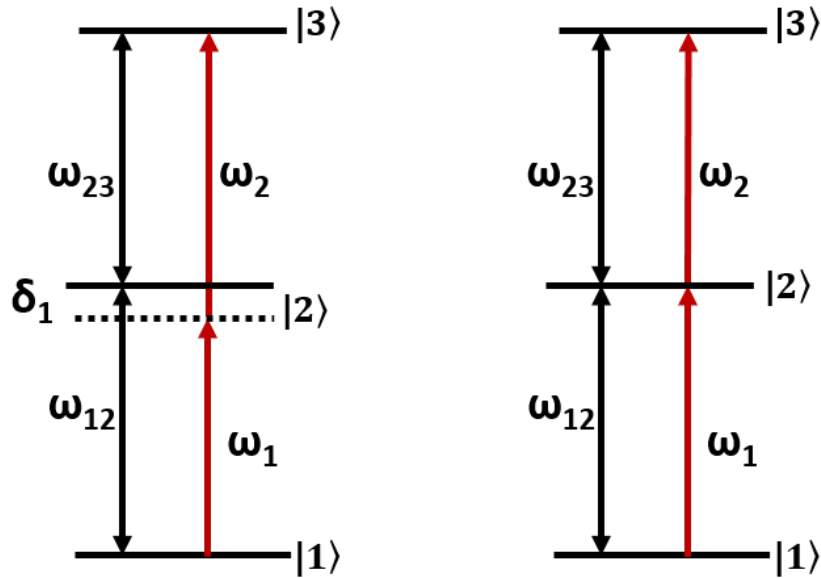


Figure 2.2: Three-level, ladder-type system. (Left) Incoherent TPA: two-photon absorption with a real intermediate state, (right) Coherent TPA: two-photon absorption with a virtual intermediate state.

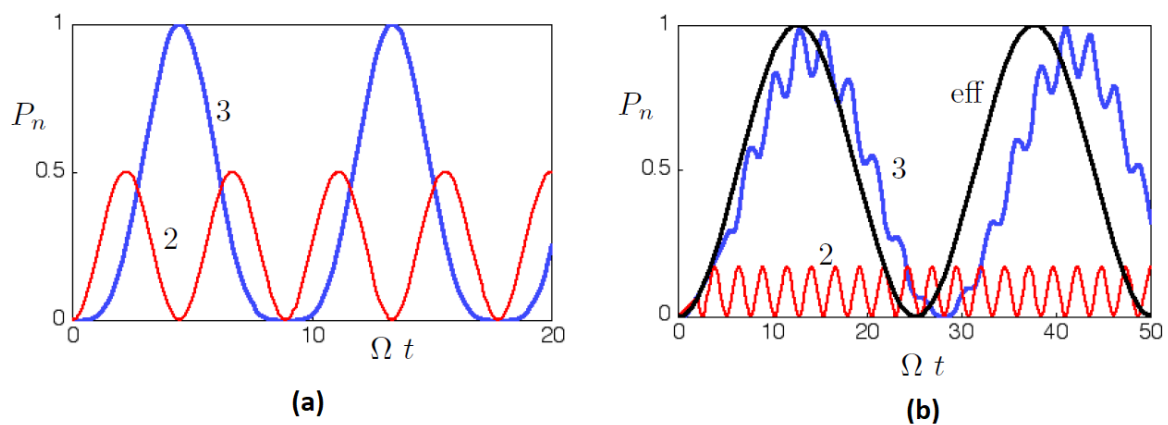


Figure 2.3: Population of the intermediate state (red) and the excited state (blue) for (a) incoherent and (b) coherent TPA. The smooth black curve shows the prediction of an effective two-state system, an approximation that becomes increasingly accurate as the detuning grows larger and the population reaching state $|2\rangle$ diminishes. Image taken from [132]. Permission granted by Acta. Physica Slovaca.

$I = |\mathcal{E}|^2$, and the polarisation dependency. The factor $|(\mathbf{u} \cdot \mathbf{u})|^2$ has a maximum value of 1 and is achieved when two fields have identical linear polarisations or opposite circular polarisations. The minimal value is achieved for two fields with orthogonal linear polarisations or identical circular polarisations. This polarisation dependency is utilised to verify the polarisation of light in an ONF, which is elaborated in Chapter 5.

2.4 Rydberg Atoms

In 1890, Johannes Rydberg proposed an equation to calculate the wavenumber of any emission line for the atoms in the first three groups of the periodic table [136] which is given by

$$k = R_y \left(\frac{1}{\mathbf{n}_1^2} - \frac{1}{\mathbf{n}_2^2} \right), \quad (2.12)$$

where k is the wavenumber, R_y is the Rydberg constant and $\mathbf{n}_{1,2}$ is the principal quantum number of the energy level. The physical meaning of \mathbf{n} and R_y is explained with the help of the Bohr atomic model, where the binding energy of an electron in a hydrogen atom is given by $-R_y/\mathbf{n}^2$. The Bohr model also successfully defines the Rydberg constant, R_y , in terms of electronic properties such that

$$R_y = \frac{Z^2 e^4 m_e}{16\pi^2 \epsilon_0^2 \hbar^2}. \quad (2.13)$$

Here, Z is the atomic number or number of protons, e is the electron charge and m_e is the mass of the electron. The value of the Rydberg constant is $10973731.6 \text{ m}^{-1}$ [68]. Even though there were shortcomings in the Bohr atomic model, it helped to introduce the scaling laws for the atomic properties with \mathbf{n} . Later, it was verified using a full quantum mechanical model. Table 2.1 shows how the properties scale with \mathbf{n} . In alkali metal atoms of particular interest, when an electron is excited to a high \mathbf{n} level, the scaling laws found for hydrogen are valid. The difference between hydrogen and the alkali atoms is the influence of the core electrons on the valence electron. When the electron is far from the core, the valence electron sees a net positive charge of 1. However, when the valence electron is closer, and for the states $L \leq 3$, it sees a higher charge since the valence electron can penetrate the closed electron shells causing improper screening. This leads to an increase in the binding energy $E(\mathbf{n}, J, L)$ which can be accounted by including a quantum defect term, $\delta_R(\mathbf{n}, J, L)$, which depends on the principal quantum number \mathbf{n} , the total angular momentum quantum number, J , and the orbital angular momentum quantum number, L , such that

$$\mathbf{n}^* = \mathbf{n} - \delta_R(\mathbf{n}, J, L). \quad (2.14)$$

\mathbf{n}^* is known as the effective principal quantum number. The quantum defect can be expressed with the Rydberg-Ritz formula as [68]

$$\delta_R(\mathbf{n}, J, L) = \delta_{R0} + \frac{\delta_{R2}}{(\mathbf{n} - \delta_{R0})^2} + \frac{\delta_{R4}}{(\mathbf{n} - \delta_{R0})^4} + \frac{\delta_{R6}}{(\mathbf{n} - \delta_{R0})^6} + \dots \quad (2.15)$$

Table 2.1: Rydberg scaling properties. Values are taken from [69]

Property	Scaling $(\mathbf{n}^*)^x$	5S state	Rydberg state 43 S
Orbit radius	2 [139]	$2.974 \times 10^{-10} \text{m}$	$1258.858 \times 10^{-10} \text{m}$
Binding energy	-2 [140]	4.18 eV	8.56 meV
Radiative lifetime	3 [141]	26.2 ns	42.3 μs
Polarisability	7	-79.4 mHz/(V/ cm^2)	-17.7 MHz/(V/ cm^2)

Here, the terms δ_{R0} , δ_{R2} , δ_{R4} , δ_{R6} are the higher order terms in the expansion of δ_R and can be found from spectroscopic measurements [137, 138]. With the inclusion of the quantum defect, the binding energy can be rewritten as

$$E(\mathbf{n}, J, L) = \frac{-R'}{(\mathbf{n} - \delta_R(\mathbf{n}, J, L))^2} = \frac{-R'}{(\mathbf{n}^*)^2}, \quad (2.16)$$

where $R' = R_y / (1 + (m_e/m_n))$ is the specific Rydberg constant for the element and R_y is the Rydberg constant. The effective quantum number depends mainly on L. In the case of rubidium, $\delta_R \approx 0$ [137], when $L > 3$, *i.e.*, it can be approximated to the hydrogen atom.

In Table 2.1, we present values for the 5S ground state and the 43S excited state for rubidium to compare and understand how dramatically the properties are scaled. One of the interesting properties of the Rydberg states is the large orbital radius and, therefore, the dipole moment scales with \mathbf{n}^2 . The consequence of the large dipole moment is an extreme sensitivity to external fields. This large dipole moment leads to strong interactions between pair of atoms. Consider two 2-level atoms with a ground state, $|g\rangle$ and a Rydberg state, $|r\rangle$. The spectrum of the two atoms consists of $|gg\rangle$, $|rg\rangle \pm |gr\rangle$ and $|rr\rangle$. The interaction between the atoms ($V(r)$) falls into two regimes: van der Waals and the resonant dipole regimes. The contribution from the nearest neighbours changes as the interaction regime changes. In the van der Waals regime, the interactions are dominated by nearest neighbour [76, 142], whereas in the resonant dipole-dipole regime the surrounding atoms are equally important. The state $|rr\rangle$ is shifted depending on the distance between the atoms. When a laser is tuned to resonance for one atom, at large separations both the atoms can be excited to Rydberg levels. As the distance reduces, the interaction detunes $|rr\rangle$ from resonance with the laser. This suppression of excitation to the Rydberg level is called Rydberg blockade (see Fig. 2.4).

The main criterion for the blockade of Rydberg excitation is that the interaction energy between two atoms should be more than the linewidth, Γ_r , of the $|rr\rangle$ state, *i.e.*,

$$V(r) > \hbar \times \max(\Omega_R, \Gamma_r), \quad (2.17)$$

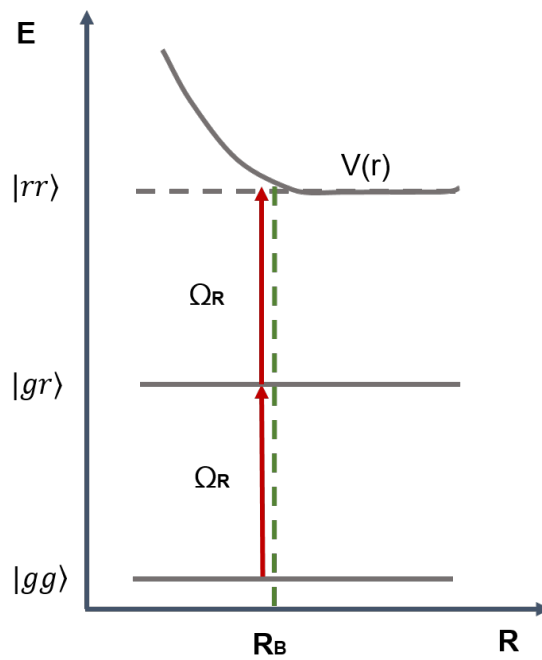


Figure 2.4: Schematic illustration of the principle of the Rydberg blockade for two atoms. Ω_R is the single atom Rabi frequency. The Rydberg blockade radius, R_B , determines the volume of atoms which takes part in Rydberg blockade. In an ensemble of N atoms within a blockade volume, one excitation is possible due to the position-dependent shift of the energy level, $|rr\rangle$, induced by the interaction. Each blockade sphere acts as a superatom which has two levels, hence, the blockade helps to create a singly excited collective state.

where $\max(\Omega_R, \Gamma_r)$ gives the maximum values of the linewidth of $|rr\rangle$ and the Rabi frequency, Ω_R . This criterion is satisfied when the separation between the atoms is less than the blockade radius, defined by

$$R_B = \sqrt[6]{\frac{C_6}{\Omega_R}}, \quad (2.18)$$

where C_6 is the van der Waals interaction coefficient.

The atom is excited to the final Rydberg state when the electromagnetic radiation interacts with the dipole moment of the valence electron. The coupling strength is proportional to the dipole matrix element, which is dependent on the overlap of its wave function with the electric dipole moment. The dipole moment for a Rydberg transition is extremely small. Hence, we need to rely on intense and narrow lasers for Rydberg excitation. For example, let us consider a single photon excitation from the 5S ground state to the $n=30$ Rydberg level in ^{87}Rb excited by light at 298.113 nm. Even if we use 1 W focussed to 50 μm , we obtain a very low Rabi frequency. Hence, to avoid using high power short wavelength lasers, typically, the excitation to Rydberg levels is achieved by a two-photon process or sometimes even by a three-photon process due to the easy availability of stable high power lasers at these wavelengths.

The long lifetime, along with the strong interactions, make Rydberg atoms attractive for applications in coherent quantum gates [15]. The lifetime of Rydberg atoms is determined by radiative decay to lower levels and transitions induced to other levels by black body radiation. In order to reduce the black-body radiation induced transitions, some experiments are carried out at cryogenic temperature. In our experiments, the stray electric field from the charged surface of the ONF, even though it may be very small, could influence the lifetime of the Rydberg atoms formed near the ONF.

In this thesis work, we use a two-photon scheme to excite neutral ground state atoms to a Rydberg state. In [2], we demonstrate coherent and incoherent TPA to the Rydberg state, which is discussed in Chapter 4. When a Rydberg atom is formed next to the fibre surface, the interactions between Rydberg atoms and between the surface and the Rydberg atom could be mapped onto light with Rydberg EIT. Even though the Rydberg excitation using TPA and EIT employs the same two-photon ladder type scheme, the EIT scheme produces a sub-natural linewidth, hence the influence of the ONF on the Rydberg level can be better understood with Rydberg EIT. To realise EIT in the system, the pump Rabi frequency (Ω_2) should be much higher than the decay rate. Hence, the ratio of the probe and pump Rabi frequency is crucial to successfully observe EIT in the system. Initial steps to demonstrate Rydberg EIT in an ONF-based atomic system were the primary focus of this PhD work.

2.5 Conclusions

Rydberg atoms are highly excited atoms where the properties can be approximated with simple scaling laws with respect to the principal quantum number, n . For the alkali metal atoms, the interaction with the core creates a perturbation to the hydrogenic states that is characterised by quantum defects. The scaling with n allows a great degree of control over the magnitude and sign of the interaction, which can

be additionally tuned using external fields to create long-range, resonant dipole-dipole interactions.

In this thesis, we explore two schemes of TPA. We rely on the two-frequency TPA for the Rydberg excitation using 780 nm and 480 nm light. Other than the Rydberg excitation, we study the parameters influencing the strength of the single-frequency TPA using 993 nm light. To appreciate the experiments in this thesis an understanding of the three-level ladder system is inevitable. Hence, the optical Bloch equations were derived for a ladder-type, three-level atom interacting with two optical fields. This helps us to calculate the properties by knowing the density matrix. This basic understanding of light-atom interactions helps to describe and understand processes like EIT, two-photon absorption, etc., providing a necessary theoretical framework for understanding the experimental results discussed in the later chapters.

Chapter 3

Experimental Details

This chapter gives the details of the experimental system in which the work described in the later chapters is carried out. We begin the chapter by introducing the fabrication and installation process of the ONF in the vacuum chamber. The second section sheds light on the experimental techniques to produce the laser-cooled rubidium atom cloud, which is then overlapped with ONF. Lastly the characterisation techniques implemented to study the properties of the system are described.

3.1 Single-Mode Optical Nanofibres

Any optical fibre exhibits modes in which the guided light is distributed. The number of modes an optical fibre can support is related to a parameter, the V-number, which is defined by

$$V = \frac{2\pi a}{\lambda} \sqrt{n_1^2 - n_2^2}, \quad (3.1)$$

where a is the radius, n_1 and n_2 are the refractive index of the core and cladding, respectively and λ is the wavelength of the light. The V-number is proportional to the frequency, hence it is also termed as a normalised frequency. Each mode exhibits a cut-off frequency, below which the mode cannot propagate. An optical fibre is single-mode when $V < 2.405$, *i.e.*, only the fundamental mode propagates through the fibre. Each of the modes can be quasi-circularly polarised or quasi-linearly polarised. For an ONF of radius 200 nm, which is typical for experiments with Rb atoms, the V-number is plotted along with the effective refractive index of a mode, $n_{\text{eff}} = \beta/k_0$, in Fig. 3.1. The propagation constant, β , is determined by solving the eigenvalue equation given by

$$\begin{aligned} \frac{J_0(ha)}{haJ_1(ha)} = & - \left(\frac{n_1^2 + n_2^2}{2n_1^2} \right) \frac{K_1'(qa)}{qaK_1(qa)} + \frac{1}{h^2a^2} \\ & - \left[\left(\frac{n_1^2 - n_2^2}{2n_1^2} \right)^2 \left(\frac{K_1'(qa)}{qaK_1(qa)} \right)^2 + \left(\frac{\beta}{n_1k_0} \right)^2 \left(\frac{1}{q^2a^2} + \frac{1}{h^2a^2} \right)^2 \right]^{1/2}. \end{aligned} \quad (3.2)$$

In the above equation, $h = (n_1^2k^2 - \beta^2)^{1/2}$ and $q = (\beta^2 - n_2^2k^2)^{1/2}$ define the fields inside and outside of the fibre, respectively. J_n represents Bessel functions of the first kind and K_n represents the modified Bessel functions of the second kind. In this thesis,

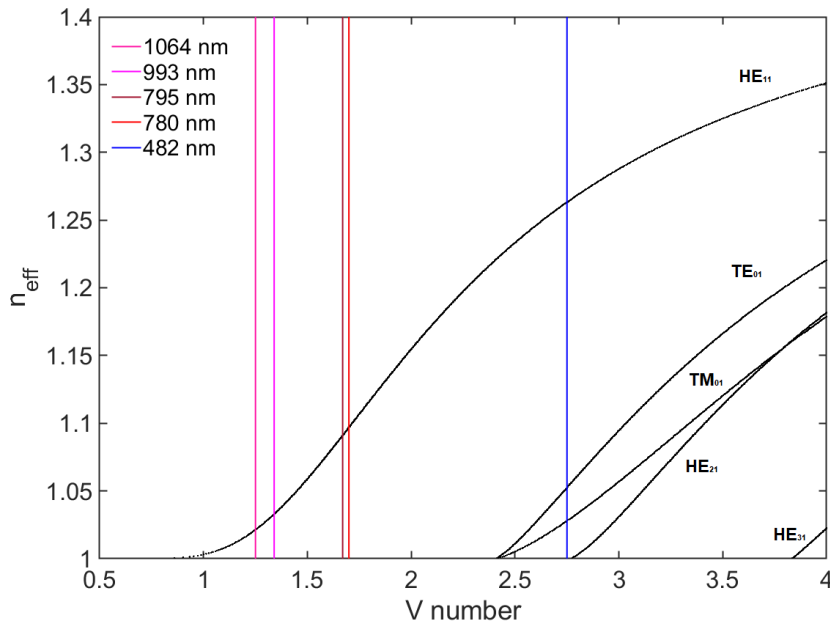


Figure 3.1: Numerical solution for the n_{eff} for a silica fibre with air as cladding for a radius of 200 nm. The vertical line gives the V-number for different wavelengths used in the thesis work.

the wavelengths of light guided in the ONF are 482 nm, 780 nm, 795 nm, 993 nm and 1064 nm and the V numbers are indicated in the Fig. 3.1. More detailed discussion on light propagation in an ONF and a derivation of the eigenvalue equation is given in Appendix A.1.

Here, we restrict the discussion to the intensity profile of quasi-linearly polarised light guided in a single-mode optical nanofibre (SM-ONF) for 780 nm. Figure 3.2 shows the intensity profile of the HE_{11} mode for a 200 nm radius ONF with 780 nm linearly polarised light guided through it. The relevant electric field equations inside and outside the fibre for the fundamental mode are given in Appendix A.2. The contrast between the refractive indices of the core and cladding along with the boundary condition for the normal component of the electric field in the ONF causes the discontinuity of the intensity at the fibre surface. We see that the electric field is maximum when $y = 0$, outside of the fibre. The defined polarisation is elliptic in the plane with the rotation around the y axis.

3.2 Optical Nanofibre Fabrication And Installation

An ONF is at the heart of the experimental system used in this thesis work. We require that the ONF used should be capable of withstanding several mW of power. Thus, the ONF fabrication process should be optimised so that it is capable of guiding a high power with a high transmission. Even though we work with different wavelengths, we optimised the ONF fabrication so that the resultant fibre is single-mode for 780 nm light. Once a good quality fibre is obtained, it is installed in the vacuum chamber for

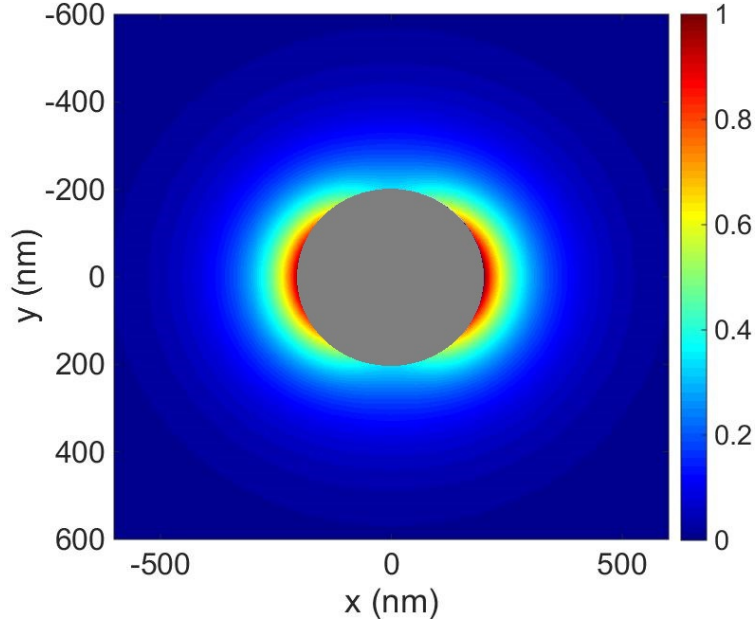


Figure 3.2: Intensity profile of the fundamental mode outside an ONF of radius 200 nm and for quasi-linearly polarised light of $\lambda=780$ nm. Colour bar indicates the intensity in arbitrary units.

the cold atoms. Then, the robustness of the fibre in ultrahigh vacuum should be tested.

3.2.1 Adiabatic Condition

In the waist region, the cladding material of the pigtail becomes the core and the surrounding medium acts as the cladding. The transition from core guidance to cladding guidance in a tapered optical fibre is very crucial and depends on the shape of the transition. In the taper region, the local fundamental mode from the core transfers to the cladding mode. To ensure a low loss in the transfer, the transition should be adiabatic at every point, *i.e.*, the fibre diameter should vary slowly. This condition restricts the tapering angle (see Fig. 3.3) to be less than Ω_z , given by

$$\Omega_z \ll \frac{r(z)}{z_b} = \frac{r(z)(\beta_1 - \beta_2)}{2\pi}, \quad (3.3)$$

where $r(z)$ is the local radius of the taper transition, the propagation constant of the fundamental mode is β_1 , the propagation constant for the nearest symmetric mode is β_2 and z_b is the beat length. When the tapering length (z_t) is larger than the beat length of the modes (z_b), the fundamental mode can propagate adiabatically. On the other hand, if $z_t \ll z_b$, there is a significant loss. Hence, the $z_t = z_b$ condition approximately establishes a delineation between the lossy and the adiabatic radius variation. For single-mode optical nanofibres (SM-ONFs), the taper angle can be relatively large due to the large difference between the propagation constants ($\beta_1 - \beta_2$) for the fundamental mode and the next higher order mode with the same symmetry.

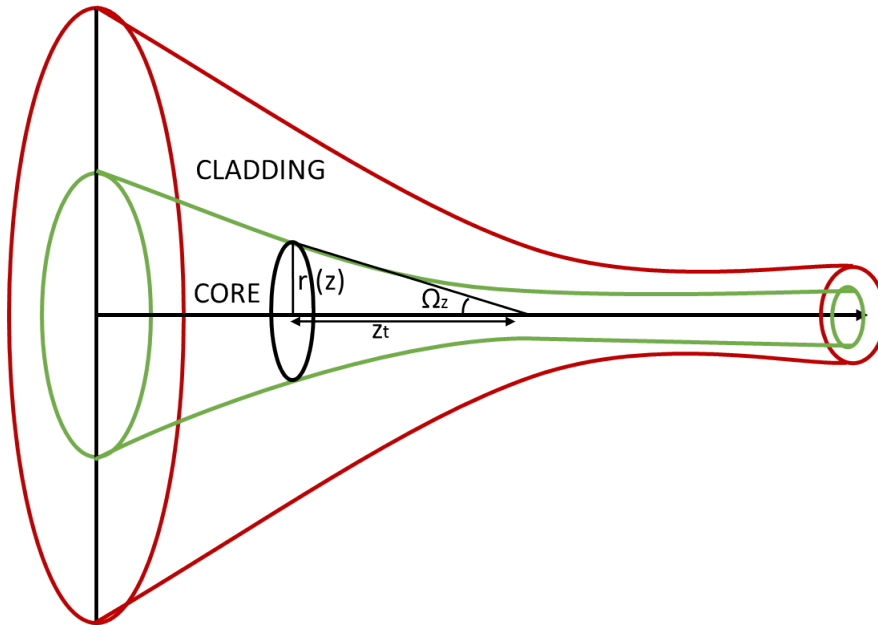


Figure 3.3: Parameters involved in the adiabatic criterion.

3.2.2 Fibre Pulling Rig

ONFs are prepared by heating and stretching optical fibre. The heat source used to heat the fibre could be a flame [143], a CO_2 laser [144] or micro-heaters [145]. Depending on the desired final precision, quality, and the waist diameter, the pulling process is chosen. Each technique has its own advantages and disadvantages which are well-explained in [143]. The techniques to pull a suitable ONF are well-developed in our research unit and used by many members for various applications. The techniques and apparatus have been refined and improved for almost two decades.

In this work, we use a flame brushing technique to produce the nanofibre. A typical schematic for a fibre pulling rig is given in Fig. 3.4. There are three independent translation stages to control the flame and the two fibre pigtailed, all of which are controlled by an XPS-Q4 controller. A LabVIEW program sends user-chosen parameters like velocity, acceleration, and position values to the XPS-Q4 controller. The fibre pulling rig uses an oxy-hydrogen flame as the heat source. A mass flow controller controls the oxygen and hydrogen flow at a fixed ratio of 1:2, so that the combustion results in only water as the byproduct. This also helps in achieving a stable flame. The gas burner is placed on one of the three motorised translation stages to control the horizontal movement and on a micrometer stage to control the vertical height. The gas burner nozzle used in the set up is a 3×3 matrix of 9 holes of $200 \mu\text{m}$ diameter designed to yield a suitable flame profile and minimise backflow. The gas nozzle's centre is aligned such that it coincides with the fibre clamped on the other two translation stages. The vertical distance between the fibre and the flame is determined by trial-and-error.

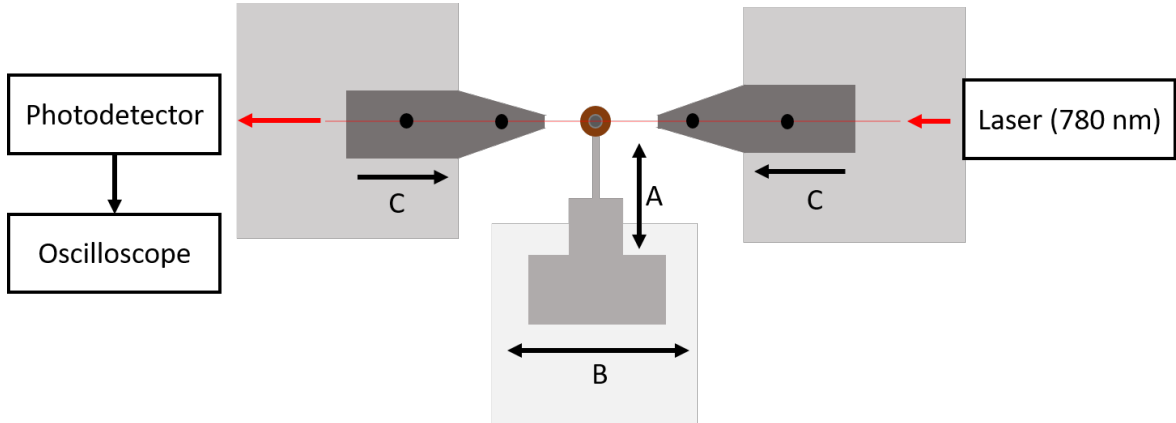


Figure 3.4: Top view schematic of the fibre pulling rig. A: Stepper motor stage. B: ILS-LM linear motor stage. C: XMS linear motor stage.

Since the fibre is of subwavelength dimension, if the environment in which the fibre is pulled is dusty, this could lead to dust settling at the nanofibre waist leading to scattering for light propagating through the fibre. HEPA filters were installed in the laboratory to maintain a clean environment. A laminar flow unit was installed on top of the rig enclosure to create a positive pressure in the cabin, also reducing dust. Obtaining a fibre suitable for ultrahigh vacuum and high power is challenging but, once installed, a single fibre can be used for many years of experiments.

3.2.3 Optical Nanofibre Fabrication

As a consequence of the adiabatic criterion, the shape of the taper is also important for carrying the correct mode through the fibre waist. The taper can be determined by two approaches –forward and reverse solving–depending on whether we restrict the shape of the transition or the pulling conditions [146]. We desire a finite taper length (to fit in the vacuum chamber and typical MOT diameter is of ~ 1 mm). For example, an exponential taper profile can be expressed by the equation of the local radius, $r(z)$, such that

$$r(z) = r_0 \exp(-z/L), \quad (3.4)$$

where r_0 is the untapered fibre radius, L is the hot zone and z is the length along the fibre axis. The hot zone is the distance over which the flame is oscillating during the pulling process.

The first step in making an ONF is to strip the acrylic coating of the fibre from the region where the tapering will be carried out. The stripped region is initially cleaned with a dry tissue and further wiped with isopropyl alcohol and then with acetone. The fibre is clamped on the translation stages which have linear stepper motors. During the process of tapering the fibre, 780 nm laser light is sent through one end of the fibre and its transmission is measured at the other pigtail using a photodiode. Once the LabVIEW program initiates the process, the flame moves horizontally to be perfectly beneath the clamped fibre via a stepper motor (indicated as A in Fig. 3.4). Then, stage B (ILS-LM linear motor) activates the horizontal movement of the flame beneath the

fibre. Simultaneously, the translation stages C (XMS linear motor translation stages) are activated and pull the fibre lengthwise, thereby reducing its diameter. The fibre is heated to between 1200°C and 1500°C, which is above the annealing temperature and lower than the softening temperature for silica. Once the process is finished the flame is removed from the proximity of the fibre.

Commercially available fibre (SM800, Fibercore) is used for the ONF preparation. The final radius of the fibre installed was calculated using Eqn. 3.4 and was found to be 258 nm. The program to fabricate the ONF with an exponential taper profile was already written and the parameters which determine the final fibre diameter were identified. The hot zone and the pull length for the desired radius (200 - 300 nm) were found by multiple trials. Hence, by repeatedly pulling and measuring the fibre waist with a scanning electron microscope, the pulling parameters given to the LabVIEW control program were optimised to get a fibre capable of carrying high power and having the desired waist.

The fibres produced typically show 99% final transmission at 780 nm. An example of such a transmission plot is given in Fig. 3.5. Once the pulling process is started, the fibre becomes so small that the light leaks into the cladding and is guided where the original cladding becomes the core and the air becomes the cladding. At this point, the core of the fibre is large in comparison with the wavelength of the light and the fibre is multimode. Since different modes have different effective refractive indices, this leads to phase differences and thereby mode interference. The mode interference pattern envelope shows beating due to the coexistence of different frequencies. These can be seen in the transmission spectrum while performing the tapering. The amplitude of these oscillations varies during the tapering process. When the fibre is small enough, the excited modes are cut off and the fibre returns to the single-mode condition again. The modes excited during the pulling process can be identified by analysing the transmission spectrum.

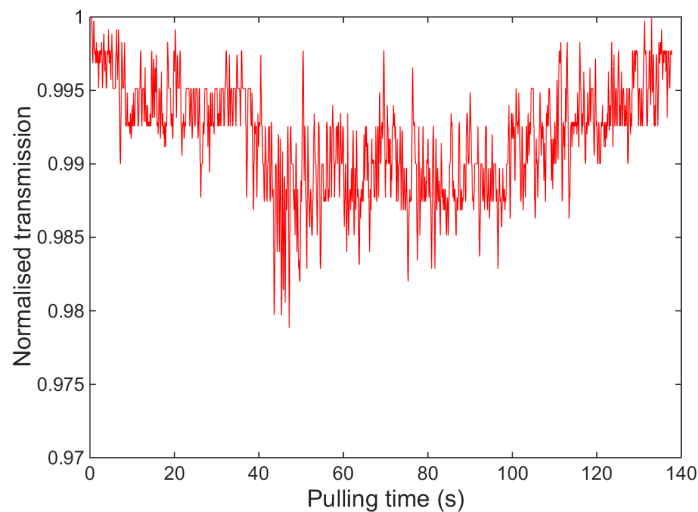


Figure 3.5: Transmission through the optical fibre as a function of pulling time. Here 1.00 is 100% transmission.

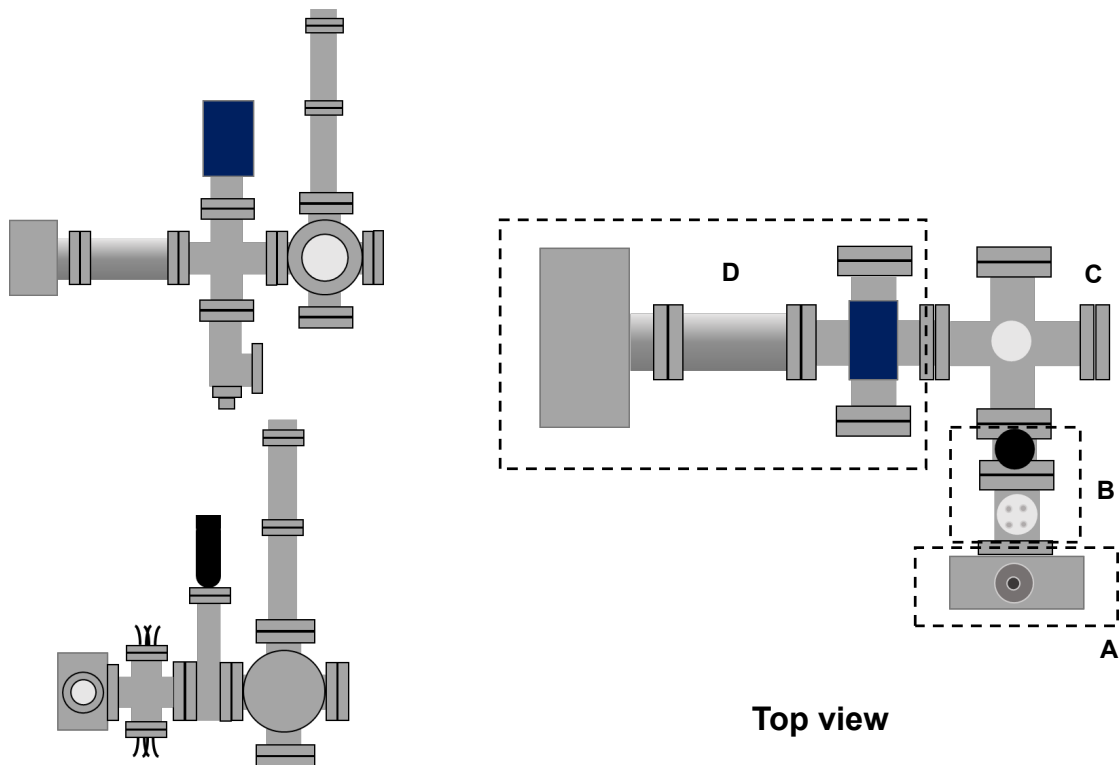
3.3 Ultrahigh Vacuum System

One of the essential requirements for the preparation of cold atoms in a MOT is ultrahigh vacuum (UHV). Once the fibre pulling process is optimised, we prepare the vacuum chamber where the fibre can be mounted. A schematic diagram of the UHV system is given in Fig. 3.6.

For ease of explanation, the system is divided into four sections. Section A is the main MOT chamber, where the ONF should be installed. The MOT chamber is a steel octagonal chamber with ten ports. Out of the ten ports, eight ports (2.75" conflat (CF) port) are in the eight rectangular surfaces and two (4.5" CF port) of them are in the octagonal surfaces. Six of the 2.75" ports are anti-reflection coated viewports allowing access for the MOT beams and probe beams. The upper and lower 2.75" ports are fibre feedthrough flanges, through which the ONF pigtail can be safely fed through the MOT chamber using Teflon ferrules. The ONF is placed in the chamber vertically on a mounting system consisting of a U-mount which is attached to a cylindrical base. This mounting system eventually gets attached to the top fibre feedthrough flange. The 4.5" port at the backside octagonal surface is connected to section B.

Section B is a four-way cross connected to a pneumatic valve. The top and bottom

Side view of sections C and D



Side view of sections A, B and C

Figure 3.6: Illustration of the vacuum system and MOT chamber.

flanges of the four-way cross are electric feedthroughs where rubidium dispensers can

be attached. Section C is a six-way cross, where one of the 4.5" CF ports is an anti-reflection coated viewport, for the access of the MOT beams. The top flange of the six-way cross is connected to the titanium sublimation pump (Agilent TSP Filament Cartridge) and the left port is connected to section D. The remaining two flanges of the six-way cross are closed off with blank CF flanges. Section D is an assembly of a four-way cross connected to an ion pump (VacIon Plus Starcell 55, Varian) using a stainless steel bellows. The top flange of the four-way cross is connected to an ionisation gauge (Dual Filament Bayard-Alpert Pirani Gauge, FRG730CF35S, Agilent Technologies). The bottom flange is connected to a T-valve (rated to 10^{-12} mbar) and to a TPS Compact (with TV81M turbo-molecular pump, TPS, Agilent Technologies) which is a combination of a scroll pump and a turbo molecular pump (TMP) via a flexible metal bellow. CF flanges and copper gaskets are used to seal the vacuum. All components are wiped with acetone using tissues before pumping.

The procedure to achieve ultrahigh vacuum is as follows: the T-valve in section D is connected to the TPS. Initially, when the system is turned on, the scroll pump is activated. Once the pressure reduces to $10^{-3} - 10^{-4}$ mbar from atmospheric pressure, the TMP turns on automatically. The TMP brings the pressure of the chamber down to 10^{-8} mbar. At this point, we bake the chamber to remove water traces and other hydrocarbons. We wrap the whole system with heating tapes (AS ONE ribbon heaters) and heat upto 125°C . We cover the system with aluminum foil to reduce the heat radiation and make the heating uniform. This baking procedure further reduces the chamber pressure to 10^{-9} mbar. When we are ready with a fibre to be mounted in the chamber, the TPS is switched off and the T-valve is connected to a nitrogen supply. The nitrogen keeps a positive pressure difference between the MOT chamber and the environment to ensure a clean environment.

3.3.1 Mounting the Optical Nanofibre

Once a good quality fibre is produced from the pulling process, with parameters optimised through several iterations, it must be mounted in the UHV. The fibre pigtailed are glued to the U-shaped mount with UHV compatible UV-cured polymer (Norland Optical Adhesive 61). The U-shaped mount along with a cylindrical base attached to the fibre feedthrough flange can be mounted in the MOT chamber.

The rig room where the fibre pulling setup is placed and the cold atom laboratory are different. After ONF preparation, it is a challenging task to transport the fibre to the MOT chamber without any contamination, which would lead to its degradation. Several aspects were crucial to achieve this, like lab cleanliness. We used a protective sleeve made from a PVC tube to transport the ONF to the MOT chamber. More details about the protective sleeve can be found in [147].

Once the fibre feedthrough flanges are sealed, the nitrogen supply is removed and the TPS is connected through a flexible bellows and turned on. The Rb dispensers (SAES alkali metal Dispenser FT type) are connected to an electrical feedthrough in section B. The rubidium getters are slotted metallic strips containing a mixture of rubidium chromate and a reducing agent. If the getter is heated to a high enough temperature, the process reduces chromate and rubidium is introduced in the chamber. Exploiting

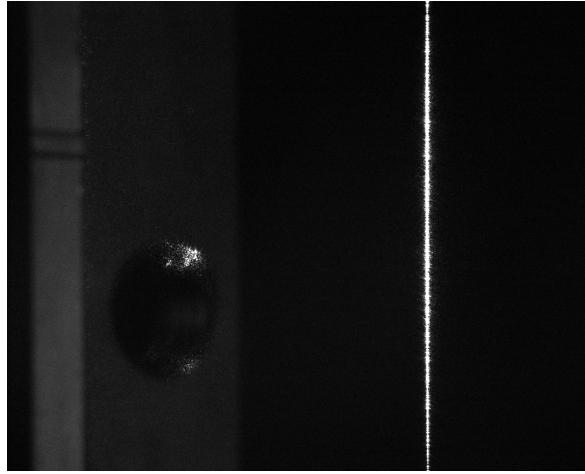


Figure 3.7: Image of an ONF installed in the UHV chamber with 30 mW of 780 nm light coupled into it as an initial test.

the Joule effect, current is applied through the electrical feedthrough to the getter. If we are activating a new getter, we increase the current to the activation current (as specified in the specification sheet) step by step, the metallic coating is evaporated and then Rb is introduced into the chamber. This process of burning a new dispenser may result in a slight increase of pressure due to the evaporated protective coating. Then the getter current is reduced to a lower value. Hence, the amount of rubidium in the UHV chamber can be controlled by the current.

At approximately 10^{-6} mbar, the ion pump is switched on. By combined action of the scroll pump, the TMP and the ion pump, the pressure of the chamber is brought down to 10^{-8} mbar. At this point, if the pressure is not restored the titanium sublimation pump is used, but it was not necessary during this work. The T-valve is closed and the TPS is removed. Then, the ion pump operates alone and the pressure is brought in the range of 10^{-9} mbar.

The fibre, which was installed in the MOT chamber, could carry at least 30 mW of 780 nm light with low loss. During the vacuum pumping process, a scattering point appeared on the ONF, but this does not affect the fibre transmission. An image of the fibre, which is currently mounted in the vacuum chamber, is given in Fig. 3.7. It has been in place since 2016.

3.4 Cold Atomic Ensemble of ^{87}Rb

The absolute temperature of the atomic ensemble is the measure of the average kinetic energy, which is proportional to the velocity. By controlling the velocity of atoms the temperature can be controlled. Laser cooling is one of the key methods to produce a trapped and cooled atomic ensemble. The MOT is widely used as a source of cold trapped atoms. Cold trapped atoms reduce effects due to the kinetic energy and also give longer interaction times and allow for more accurate tests of quantum mechanics. Isolation of an atom opens horizons for observing quantum properties of light-matter

interactions and such a system is an excellent candidate for quantum communication. Any standard atomic physics text explains the basics of magneto-optical trapping in detail [148–150].

Since the discovery of laser cooling and trapping of atoms, alkali metals have been the main elements of interest due to the availability of closed-cycle transitions, ease for accessing these transitions with commercially available diode lasers, their high scattering cross-sections, and the low vapour pressure which allows for alkali metal vapours to be produced easily. The alkali metals have only one valence electron with varying filled electronic shells, making them similar to hydrogen. We use the spectroscopic notation $n^{2s+1}L_J$ to denote the atomic levels, where n is the principal quantum number, L is the orbital angular momentum quantum number, s is the spin quantum number and J is the total angular momentum quantum number.

Natural rubidium is a mixture of 72.17% of ^{85}Rb and 27.83% ^{87}Rb . The ^{87}Rb is not a stable isotope, having a half-life of 4.88×10^{10} years and this slow decay rate makes it stable for practical considerations. ^{85}Rb is a stable isotope. The energy levels of the atoms are affected by the spin-orbit interaction, and for levels with different J values, degeneracy is lifted. This is fine structure splitting. In alkali metals, the ground state is S , and the excited state is P . The excited state has the fine structure $P_{1/2}$ and $P_{3/2}$. The degeneracy in the fine structure is lifted when one considers the nuclear magnetic moment and the total angular momentum interaction. This splitting is called hyperfine splitting. This interaction result in F states, where $F = |I - J|$ to $|I + J|$. The nuclear spin (I) for ^{85}Rb and ^{87}Rb is $5/2$ and $3/2$, respectively. We use ^{87}Rb for producing cold atoms. More details on ^{87}Rb can be found in [151]. In Fig. 3.8, a consolidated energy level diagram of ^{87}Rb and transitions involved in the course of the thesis work is given.

We chose the D_2 line at 780.241 nm of ^{87}Rb , shown in Fig. 3.9, as the closed-cycle cooling transition. The transition $5S_{1/2} F=2$ to $5P_{3/2} F'=3$, constitutes a closed-cycle, thus limiting losses during the loading of atoms into the MOT. If the excited level has many decay channels, they should be addressed with the help of an additional laser to repump these atoms to the excited level. For example, in our case, the atoms in $5P_{3/2} F'=3$ have a non-zero probability to decay back to $5S_{1/2} F=1$. Hence, we need two lasers, one addressing the cooling and one the repump transitions, to realise the MOT.

The cooling laser (Toptica TA pro), which should address the cooling transition of ^{87}Rb , is locked to the $5S_{1/2} F=2$ to $5P_{3/2} F'=(2,3)$ crossover peak of the spectrum using saturation absorption spectroscopy (Cosy, Toptica). Figure 3.10 shows the hyperfine resolved saturated absorption spectrum for the D_2 transition, three peaks correspond to the D_2 transitions and three are the so-called crossover peaks. Laser cooling requires the lasers to be red-detuned. The cooling laser is passed through a double-pass acousto optic modulator (AOM, ATM-602DA2B, IntraAction Corp, central frequency: 60 MHz)¹, which produces a shift of 120 MHz from the crossover peak towards the cooling transition (refer to Fig. 3.11(a)). We typically maintain the cooling lasers at 14 MHz red-detuned from the cooling transition. The repump laser (Toptica DL100 pro), locked to the $5S_{1/2} F=1$ to $5P_{3/2} F'=(0,2)$ crossover peak, is passed through a single-pass AOM of centre frequency 80 MHz. Figure 3.11(b) shows the frequency

¹In a double-pass AOM, the desired diffracted order from the AOM is reflected back to the AOM using a mirror. This configuration is desirable to compensate for beam deflections when the AOM is modulated.

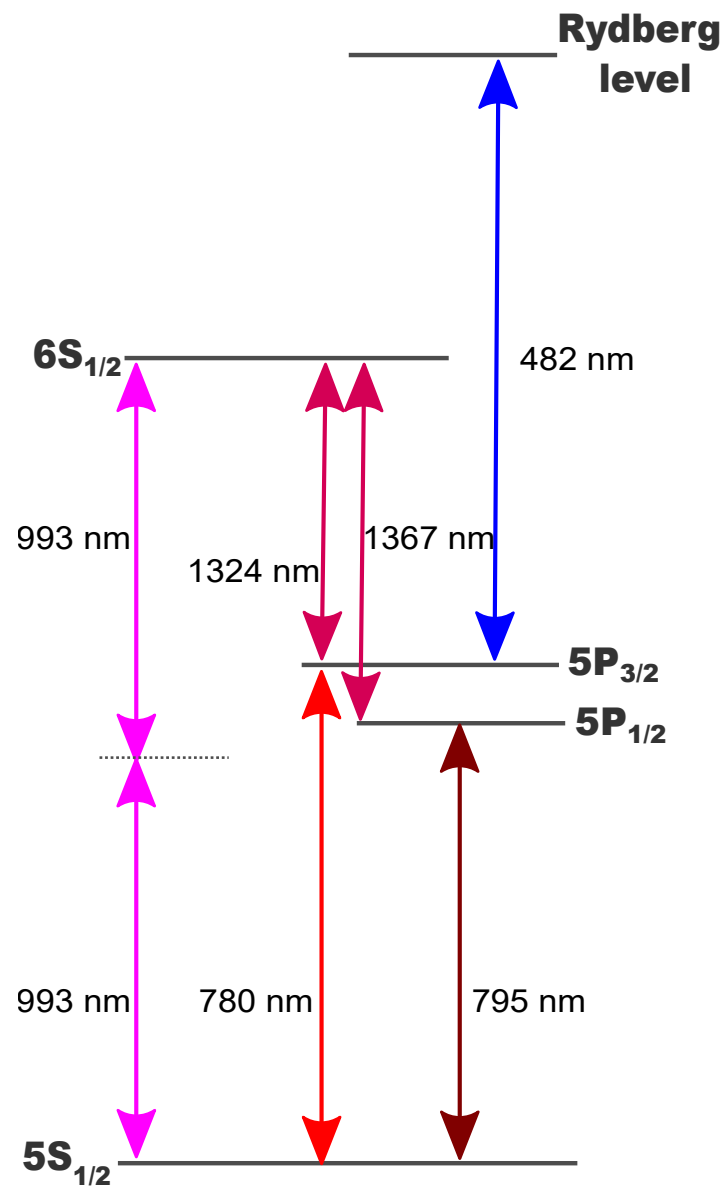


Figure 3.8: Energy levels of ^{87}Rb used in the works discussed in this thesis.

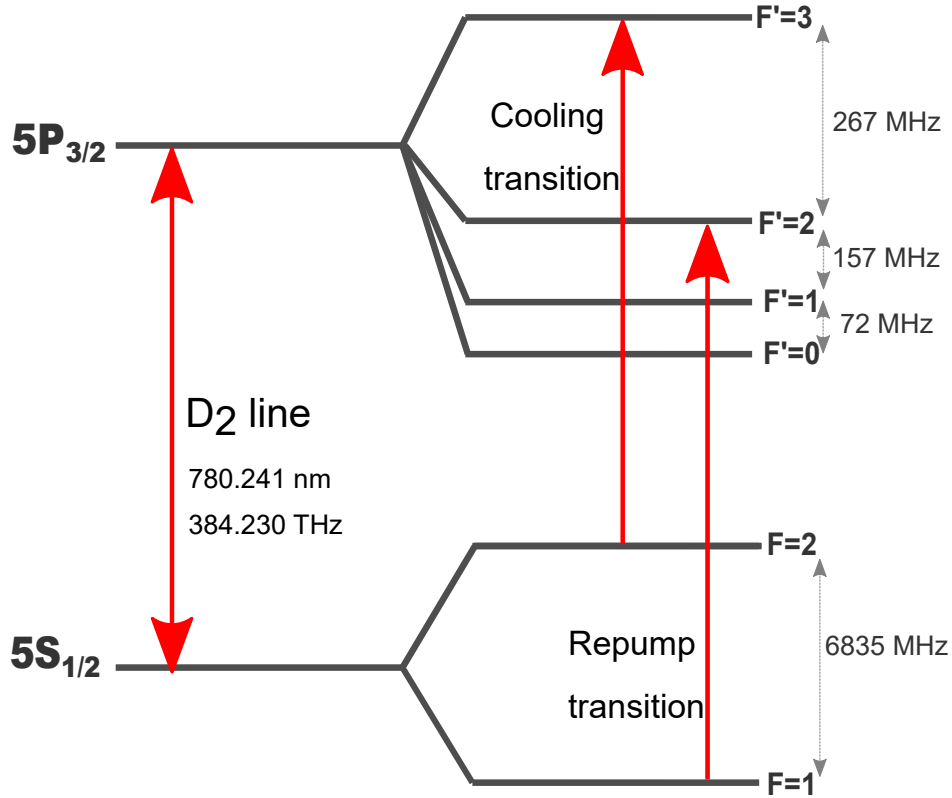


Figure 3.9: D₂ line manifold of ⁸⁷Rb used for the MOT implementation.

shifting setup for the repump light beam. The cooling beam and repump beam are then coupled to two separate commercially available polarisation maintaining fibres (PMF).

The outputs from the fibres are overlapped using half-wave plate polarising beam splitter (HWP-PBS) configuration and fed to a beam expander, shown in Fig. 3.11(c). Using a telescope arrangement (convex-concave lens combination convex lens: $f=100$ mm, concave lens: $f=-50$ mm), the diameter of the beam is expanded to 15 mm. The overlapped beam consists of 60 mW cooling beam and 2 mW repump beam and is then divided into three beams (C_x, C_y, C_z) of equal intensity with two HWP-PBS combinations.

The beams are passed through a quarter-wave plate (QWP) to make the polarisation circular. We then intersect these three beams coming from orthogonal directions at the centre of the vacuum chamber (see the Fig. 3.11(d)). The beams then pass through another QWP and are retro-reflected by a mirror. The QWP is used to restore the helicity of the polarisation of the beams, which is altered during reflection. The polarisation of the beams is maintained such that out of three, two axes are the same (say σ^+) and the third is orthogonal to the other (σ^-). The optical alignment is done such that the reflected beam overlaps with the source beam.

An inhomogeneous quadrupole magnetic field is created using two copper coils with current flowing in opposite directions, *i.e.*, in an anti-Helmholtz configuration. These coils are placed on either side of the trap centre. The two coils are identical with 200 turns and of 75 mm radii placed at a distance of 90 mm leading to a zero magnetic field at a half axial distance between the coils. We maintain a magnetic field gradient of

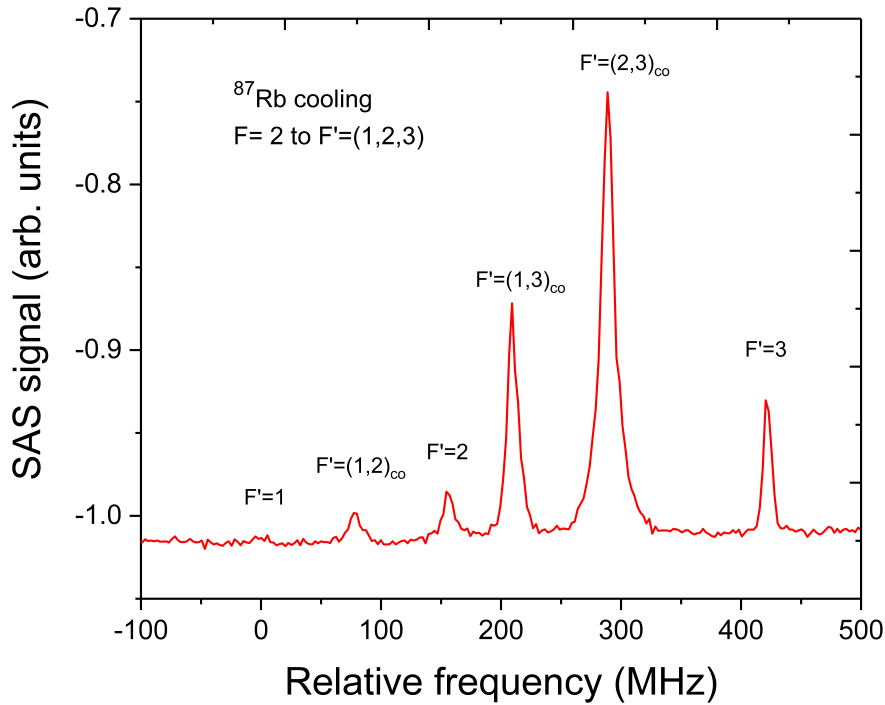


Figure 3.10: Saturated absorption spectrum of ^{87}Rb D_2 transition obtained from the locking interface (DigiLock, Toptica).

10-15 G/cm at the centre of the MOT by flowing 3.5 A of current through the coils. In addition to the anti-Helmholtz coils, we use compensation coils in all three directions. We generally use these compensation coils to adjust the overlap of the MOT atoms with the ONF.

3.5 Characterisation of the ^{87}Rb Atom Cloud

Imaging

We employ a 2:1 telescope arrangement composed of two lenses to collect fluorescence from the laser-cooled rubidium atoms. The schematic is shown in Fig. 3.12 and the lenses are achromatic doublets (L1, AC508-150B, $f_1=150$ mm and L2, AC508-300B, $f_2=300$ mm). The laser-cooled rubidium atoms scatter photons in all directions, but we collect the light passing through one of the viewports only. Using a beam splitter (BS), the collected fluorescence is sent to a camera (CCD, ANDOR Technology, Luca^{EM}R, DL-604M-OEM) and a photomultiplier tube (PMT, Hamamatsu, R636-10) in conjugation with a filter (FL, Thorlabs, FES800). Other than this imaging system, we use a Thorlabs USB3.0 camera to monitor the overlap of the atom cloud with the ONF in the orthogonal direction.

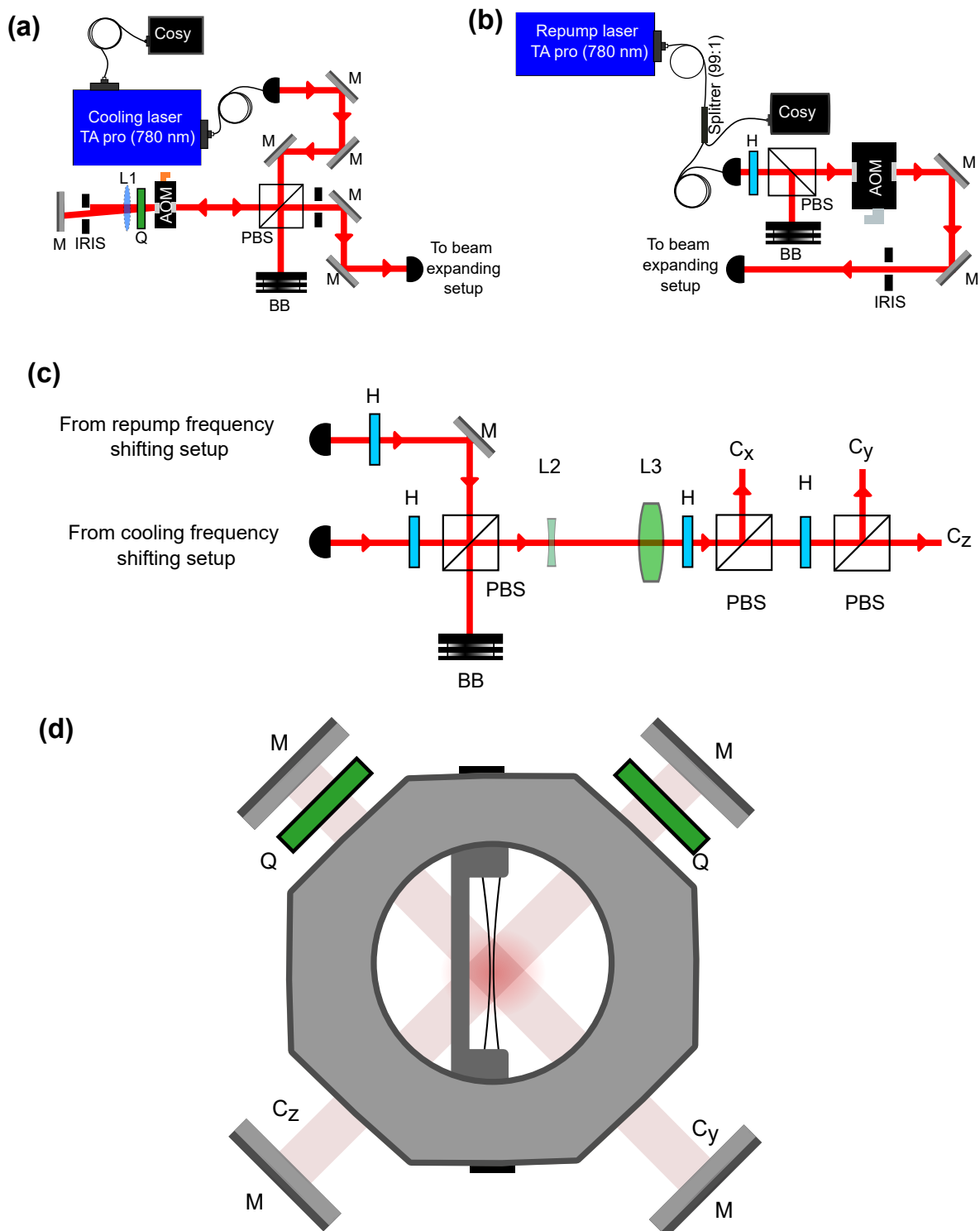


Figure 3.11: (a) Frequency shifting setup for cooling laser. (b) Frequency shifting setup for repump laser. (c) Beam expanding setup. The expanded beam is divided into three equal power beams (C_x, C_y, C_z) (d) Side view of ONF mounted vacuum chamber. M: Mirror. PBS: Polarising beam splitter. BB: Beam block. AOM: Acousto-optic modulator. Q: Quarter-wave plate. H: Half-wave plate. L: Lens. CoSy: Compact saturation spectroscopy.

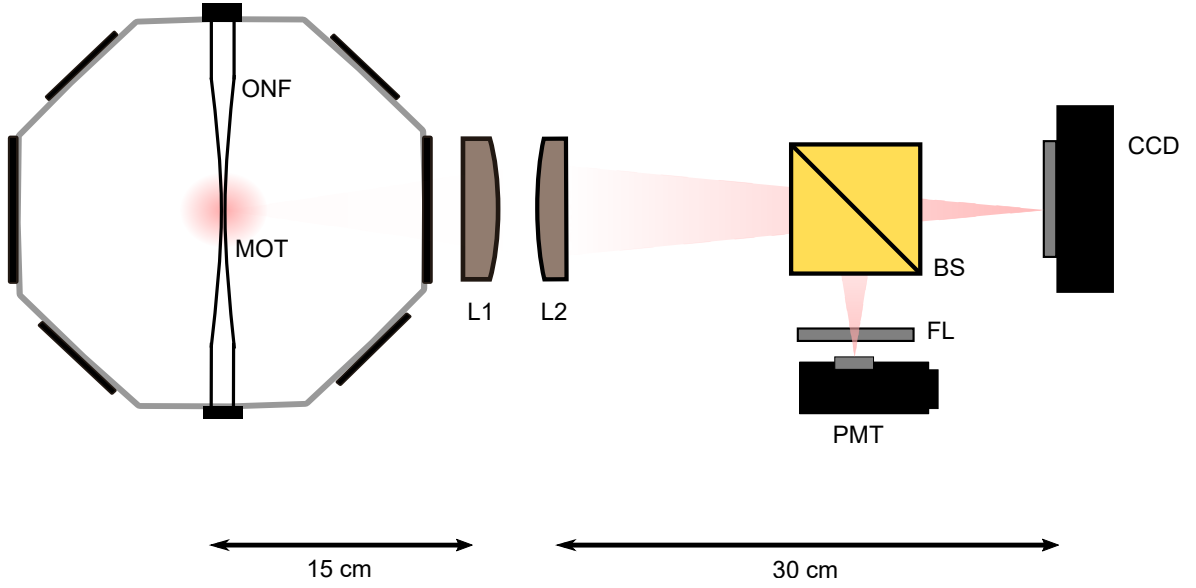


Figure 3.12: Sketch of the imaging of the fluorescence of the MOT. L1,L2: Achromatic doublets. BS: 50:50 beam splitter. FL: Filter. PMT: Photomultiplier tube. CCD: Charged coupled device.

Number of Atoms

To calculate the number of atoms, we rely on the signal we collect from the PMT. The PMT response curve was calibrated for different amplifier voltages and incident powers. From the calibrated PMT response, the obtained signal for laser-cooled atom is 1.462 V at 830 V. The number of atoms can be calculated with the following equation

$$N_{\text{atoms}} = \frac{2P\Theta}{\Gamma\hbar\omega} \left(\frac{I/I_s}{1 + I/I_s + (2\delta/\Gamma)^2} \right)^{-1}, \quad (3.5)$$

where P is the power corresponding to the obtained signal, Γ is the decay rate of the excited state, Θ gives the fraction of the solid angle from which the fluorescence is collected, I is the intensity of the cooling beam, I_s is the saturation intensity, δ is the detuning between the laser frequency and the atomic transition frequency. The number of atoms is calculated to be 1.872×10^6 atoms.

Atomic Density

The atomic density in the Rb cloud can be calculated directly from the image obtained from the CCD camera. The Andor camera detector area is composed of an array of 1004 (H) \times 1002 (V) pixels, with a pixel size of $8 \mu\text{m} \times 8 \mu\text{m}$. The number of atoms can be calculated from the following equation

$$\frac{N_{\text{counts}}}{\eta t_{\text{exp}}} = N_{\text{atoms}} \Theta \left(\frac{I/I_s}{1 + I/I_s + (2\delta/\Gamma)^2} \right), \quad (3.6)$$

where N_{counts} is the count collected by the camera and η is the quantum efficiency of the CCD (48% at 780 nm), t_{exp} is the exposure time. A sample fluorescence image of

the cloud of trapped atoms is given in the Fig. 3.13(a). The peak density is determined to be 14×10^9 atoms per cm^3 .

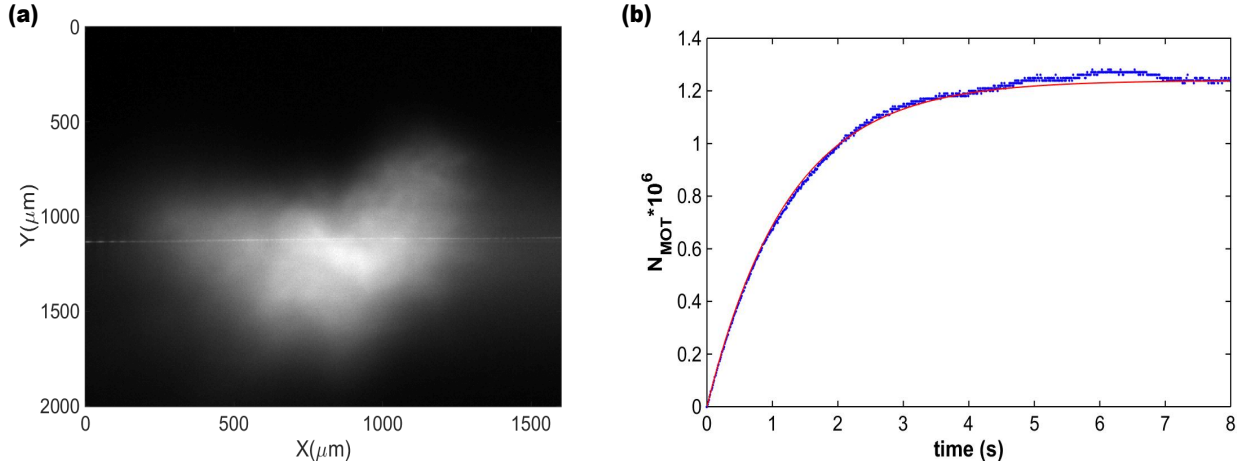


Figure 3.13: (a) Fluorescence image of the cold atom cloud around the nanofibre. (b) Loading of atoms in the MOT.

Trap Loading and Loss Rate

In our setup, atoms are loaded into the MOT from background Rb vapour. When the MOT is turned on, the number of trapped atoms increases initially. The loading rate of atoms, *i.e.*, the number of atoms that enter the trap per second [152], is given by

$$L_{\text{MOT}} = \frac{1}{2} n v_c^4 V^{2/3} \left(\frac{m_a}{2k_B T} \right)^{3/2}. \quad (3.7)$$

The loading rate depends on the atomic mass (m_a), density of the atoms (n), the capture velocity (v_c), the trapping volume (V) and the initial temperature of atoms in the background vapour (T) [153, 154]. The loss rate from the trap is mainly due to collisions with the background vapour and collisions between atoms in the trap. For magneto-optically trapped atoms, where the density is relatively low, the contributions from the collision of atoms within the trap can be neglected and the loss rate of atoms from the MOT is defined as [155]

$$\gamma_{ml} = n \sigma \left(\frac{3k_B T}{m_a} \right)^{1/2}. \quad (3.8)$$

In Eqn. 3.8, σ is the cross-section of an atom in the vapour to collide with a trapped atom causing it to be kicked out of the trap. The capture rate and loss rate find an equilibrium and a steady state is established. The rate of change in the number of MOT atoms (N_{MOT}) is defined by the differential equation

$$\frac{dN_{\text{MOT}}}{dt} = L_{\text{MOT}} - N_{\text{MOT}} \gamma_{ml}. \quad (3.9)$$

The time-dependent solution of Eqn. 3.9 is

$$N(t) = N_0(1 - e^{-\gamma_{ml}t}), \quad (3.10)$$

where $N_0 = L_{\text{MOT}}/\gamma_{ml}$ is the steady state atom number in the MOT. A typical MOT loading curve is shown in the Fig. 3.13(b). The loading curve is obtained from the MOT fluorescence detected with the PMT. From Fig. 3.13(b), N_0 is 1.2×10^6 atoms, γ_{ml} is 1.03844 per s and the loading rate is 9.72×10^5 atoms per s.

Temperature

There are different methods to find the average temperature of the trapped atoms. Here, we use the time-of-flight method, which relies on imaging the fluorescence of a thermally expanding atom cloud. The anti-Helmholtz coils, cooling and repump lasers are tuned off simultaneously. After a time, t , the cooling lasers are turned on. The fluorescence image is collected by varying t every millisecond. The temperature of the cloud can be calculated from the relation

$$T_{\text{cloud}} = \frac{m_a \Delta\tau}{k_B}, \quad (3.11)$$

where m_a is the mass of the atom, k_B is the Boltzmann constant and $\Delta\tau$ is the slope of the curve, when the cloud diameter squared is plotted against the expansion time squared. We found typical cloud temperature of $\sim 125 \mu\text{K}$.

3.6 Fluorescence Signal Coupled to the ONF

The coarse alignment of the MOT with the ONF is done using the imaging system explained in Section 3.5. The fine overlap of the cold atom with the ONF is done by monitoring the fluorescence count coupled to the ONF. Figure 3.14(a), is the arrangement used to direct the MOT fluorescence from the ONF to the detectors, which are single photon counting modules (SPCM, Excelitas Technologies, SPCM-AQRH-14-FC). We use a 780 nm filter (Thorlabs FB780-10) in conjugation with the SPCM to eliminate the background. The quantum efficiency of the SPCM for 780 nm is 60% and the dark count is 100 counts/s. A typical obtained loading curve coupled to the ONF in the SPCM is given in Fig. 3.14(b). Here, the cooling laser is switched on after 1.5 s, thereby initiating the loading of atoms into the MOT. LabVIEW is used to generate and control the timing sequence. The SPCM collects the signal at an integration time of 1 ms.

Note that we use an additional 1064 nm laser (Mephisto 1064 nm laser), which is a high power laser providing up to 450 mW. The 1064 nm laser is sent through an AOM (AA optoelectronics, MT80-A1-1064, centre frequency: 80 MHz) in order to achieve control over the trap by switching on and off the laser beams. During the experiment, 100 μW of 1064 nm light is passed through the ONF from each side to keep the fibre hot and avoid atom deposition on the ONF [156]. This light has the added advantage of attracting atoms toward the ONF surface, thereby increasing the number of atoms interacting with the evanescent field.

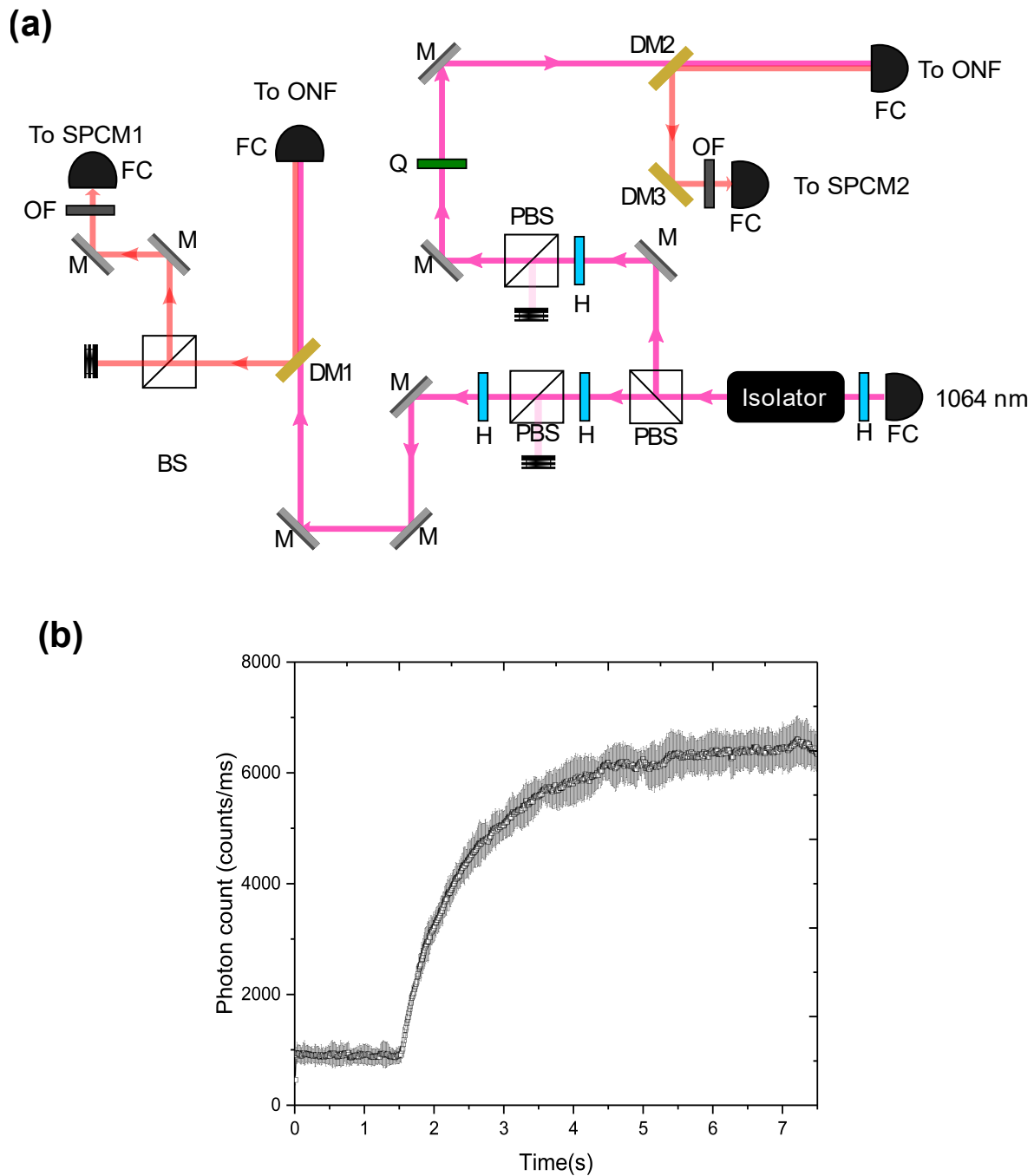


Figure 3.14: (a) Optical layout for detection of the fluorescence coupled to ONF. M: Mirror. BS: Beam splitter. DM: Dichroic mirror. H: Half-wave plate. Q: Quarter-wave plate. OF: Optical filter. PBS: Polarising beam splitter. SPCM: Single counting photon module. FC: Fibre coupler. The different coloured arrows indicate different wavelengths of light, 780 nm: Red and 1064 nm: Pink, respectively. (b) Fluorescence count rate (per ms) from the atom cloud as a function of time.

3.7 Conclusions

In this chapter, we have discussed briefly about the fibre pulling process to produce an ONF. We explained the details involved in mounting the fibre in the UHV chamber. We then described the experimental details involved in creating a magneto-optical trap for ^{87}Rb atoms. Next, we discussed the atom characteristics such as the number of atoms, atomic density, temperature and the loading and loss rates of the atoms to the trap. Note the numbers here are sample values and changed during the course of the experimental work.

Chapter 4

Cold Rubidium Rydberg Atoms near an Optical Nanofibre

The primary aim of this thesis work was to study the generation of Rydberg atoms within a few hundred nm of an ONF. To date, ground-state cold atom-ONF hybrid systems [52, 53] have shown tremendous potential for a new generation of quantum devices. The small cross-section of the evanescent field from an ONF, as a result of the exponential radial decay from the fibre waist as discussed in Chapter 1, leads to a large co-operativity [31, 33], the key to many quantum optics experiments. The high intensity and field gradient can be used to optically trap atoms in a one-dimensional array [48, 157], thereby enabling the study of one-dimensional, many-body physics, or can be exploited for quadrupole transition enhancement [158]. Recently, the quadrupole transition was demonstrated in a MOT-ONF system [3], see Appendix B.2. Cooperative effects, such as the generation of a collective entangled state [159], have also been demonstrated in such a system using ground-state neutral Cs atoms. In addition, atoms in the evanescent field region are intrinsically coupled to an optical bus in the form of the fibre-guided mode.

Rydberg atoms have been studied next to an atom chip [112], a μm -sized vapour cell [107], inside a hollow-core photonic crystal fibre [114, 116] and it has been proposed to use a superconducting resonator [160], with each platform having its own advantages and disadvantages. In this chapter we explore an alternative, but highly viable, platform for atom-based quantum networks by interfacing cold Rydberg atoms with an ONF. This could lead to low-loss transfer of information to and from the interaction region [20, 118], a prerequisite for Rydberg-based quantum repeaters in fibre-coupled cavities [21].

We employ a two-photon, ladder-type excitation using 780 nm and 482 nm lasers to excite the neutral ground state atoms to the Rydberg levels (for an energy level diagram see Fig. 4.1). In the first section, we introduce the 482 nm laser locking technique, which is based on vapour cell EIT. We then explain the electro-optic modulator based locking scheme where we achieved a frequency-stabilised 482 nm laser with a tunable central offset frequency. In the second section, the two-photon excitation to a Rydberg level in the MOT-ONF system is studied. Here, we used trap loss to study the Rydberg excitation. In the final sections, we discuss Rydberg EIT studies carried out in the ONF:atom system.

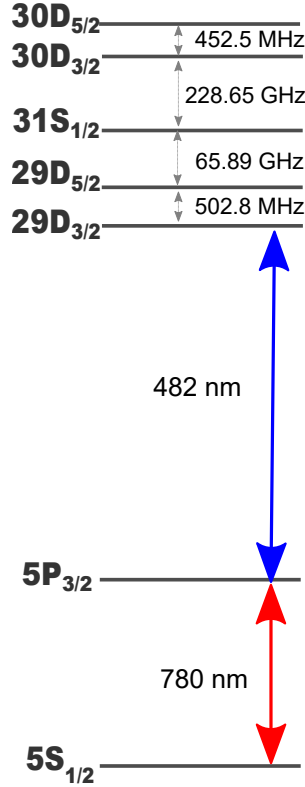


Figure 4.1: Two-photon transitions for Rydberg excitation discussed in this chapter.

4.1 Vapour Cell Rydberg EIT and Step Scanning with EOM Sideband Locking

Most atomic experiments rely on stable frequency lasers. Usually, we rely on optical transitions to lock the lasers to a particular frequency. In this thesis work, we have used saturated absorption spectroscopy to lock the cooling laser, repump laser, etc (refer to Chapter 3). In saturated absorption spectroscopy, we obtain a Doppler-free spectrum of the required transition which is used to lock the frequency of the laser. This requires a feedback, where an error signal proportional to the laser frequency detuning from the desired frequency is feedback to the controller which subsequently adjusts the frequency. In this section, we introduce the experimental setup and techniques implemented to lock the 482 nm laser to the Rydberg transition. This locking scheme is based on an EIT technique using a ladder-type scheme involving Rydberg states to produce the locking signal which is used to lock the laser [161]. This enables laser stabilisation to excited Rydberg state transitions based on atomic coherences.

The experimental schematic is given in Fig. 4.2. Light from a 780 nm laser (DL-pro, Toptica), locked to the $5S_{1/2}(F = 2) \rightarrow 5S_{3/2}(F' = 3)$ transition using saturated absorption spectroscopy (CoSy, Toptica), acts as the probe while the pump is at 482 nm. The 482 nm light is derived from a frequency-doubled high power laser (TA SHG pro, Toptica) and is scanned across the $5P_{3/2}$ to the desired Rydberg transition. Here, we show the results for $29D_{5/2}$. The Rydberg EIT experiments are done in a ^{87}Rb enriched vapour cell (TT-RB87-75-V-P, TRIAD technology) of dimensions 25 mm \times

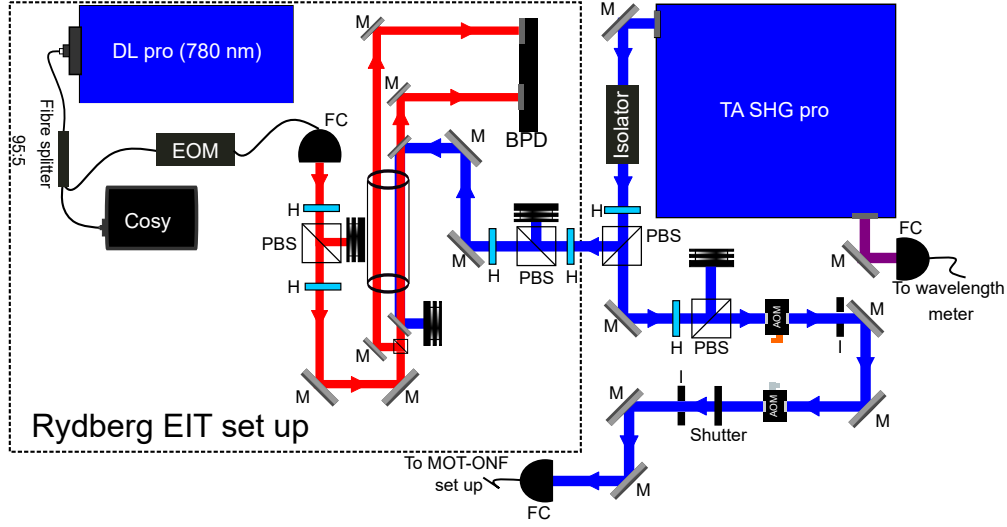


Figure 4.2: Vapour cell Rydberg EIT setup. EOM: Electro-optic modulator. H: Half-wave plate. PBS: Polarising beam splitter. M: Mirror. BPD: Balanced photodiode. I: Iris. AOM: Acousto-optic modulator. FC: Fibre coupler. The different coloured arrows indicate different wavelengths of light, 780 nm: red and 482 nm: blue, respectively.

7.5 mm, at room temperature. The transmission of the probe laser through the atomic vapour in the presence or absence of the pump is detected using a balanced photodiode (PDB210A/M, Thorlabs). When the 482 nm laser is resonant with the Rydberg transition, we see a peak in the probe transmission, which is the EIT signal. A typical Rydberg EIT signal and error signal is given in Fig. 4.2. This EIT signal is used for locking the frequency of the 482 nm laser. Here, in the EIT-based locking technique, the EIT signal is generated from a two-photon resonance, *i.e.*, the pump laser is locked relative to the probe laser.

When we need to step-wise scan the frequency of the pump laser (482 nm laser), the probe laser is locked on the $^{85}\text{Rb } 5S_{1/2}(F = 3) \rightarrow 5P_{3/2}(F' = 3, 4)_{co}$ using saturated absorption spectroscopy. Since the vapour cell is ^{87}Rb enriched, the EIT condition is not fulfilled. Thereby we do not observe an EIT peak. We connect the 95% end of the fibre splitter from the probe laser to a fibre electro-optic modulator (EOM, NIR-NPX800, Photline Technologies) and the output is connected to the Rydberg EIT setup (refer to Fig. 4.2). The EOM is connected to a radio frequency (RF) generator (E8257D, Keysight analog signal generator) which is used to produce a probe laser side-band at desired frequency. The frequency separation between the $^{85}\text{Rb } 5S_{1/2}(F = 3) \rightarrow 5P_{3/2}(F' = 3, 4)_{co}$ and $^{87}\text{Rb } 5S_{1/2}(F = 2) \rightarrow 5P_{3/2}(F' = 3)$ is 1.0662 GHz (see Fig. 4.4(left)). When we adjust the sideband frequency to 1.0662 GHz, the output satisfies the EIT condition for the same frequency of the 482 nm laser, thereby we obtain the EIT peak. We shift the sideband frequency of the EOM to produce the frequency shift in the 482 nm laser. An example of an error signal for the $29D_{5/2}$ EIT peak when the EOM is on and off is given in Fig. 4.4(right). Thus, we have performed laser frequency stabilisation to an excited Rydberg transition based on a ladder-type three-level EIT. To the best of our knowledge, this is the first demonstration of step scanning with EOM-based locking using Rydberg EIT.

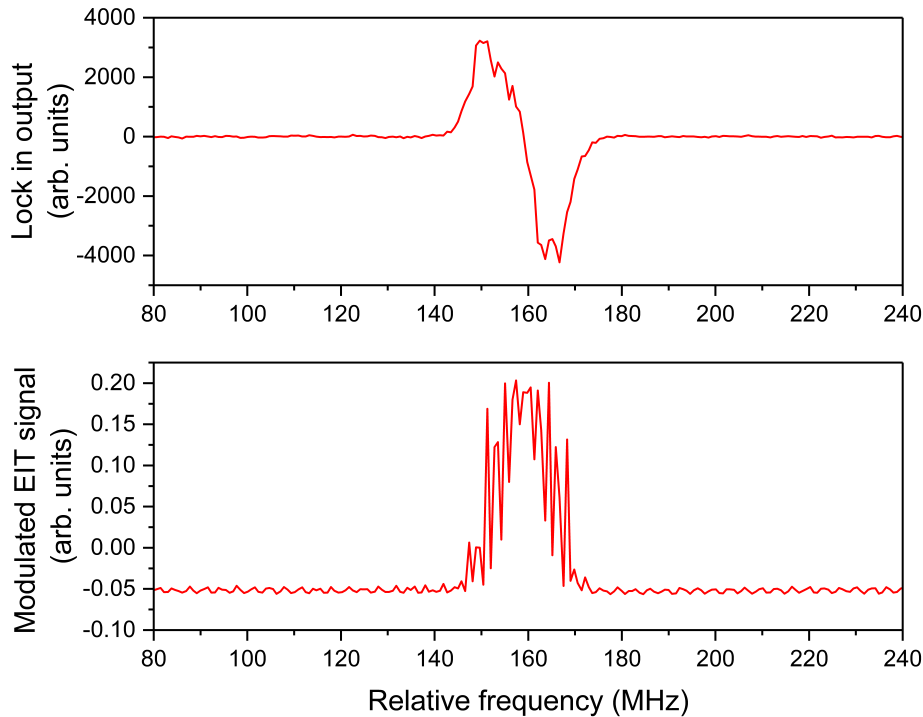


Figure 4.3: Modulated vapour cell Rydberg EIT spectrum of $29D_{5/2}$ (bottom panel) and the corresponding error signal (top panel) obtained from the locking interface (Digilock, Toptica).

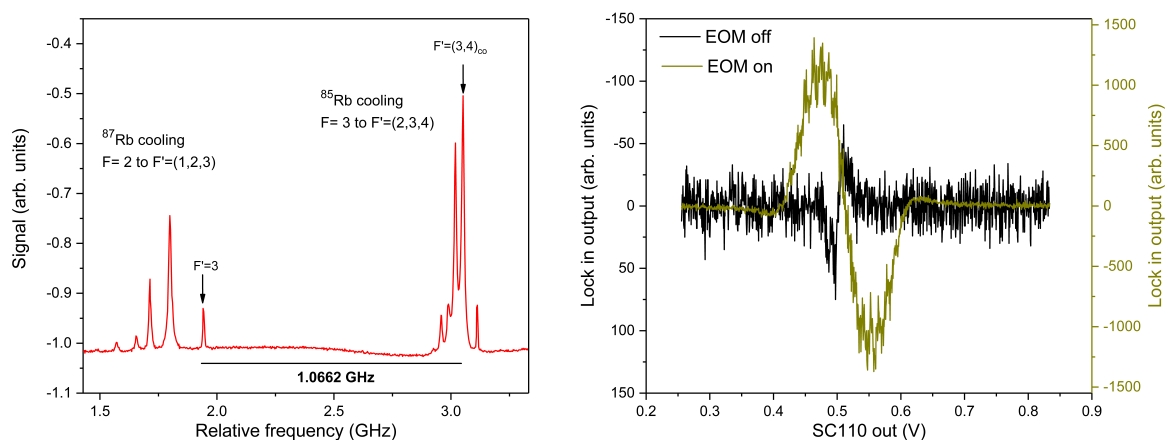


Figure 4.4: (Left) Saturated absorption spectrum of rubidium obtained from the locking interface (Digilock, Toptica). (right) Error signal obtained with the EOM on (green) and off (black).

4.2 Trap Loss Studies with $29D_{X/2}$ Rydberg Atoms¹

In this work, we studied on evanescent field assisted Rydberg excitation at submicron distances from the surface of an ONF, which was embedded in a ^{87}Rb atomic ensemble in a MOT. A ladder-type, two-photon excitation scheme was used to excite the atoms to the Rydberg state and a trap loss method [93] was used to probe the Rydberg excitation. We implemented a rate equation model [120] to determine the rate of population transfer to the Rydberg state. Both coherent two-photon excitation and incoherent two-step excitation was demonstrated. A density matrix based model was developed for the three-level ladder-type system interacting with the evanescent field of the ONF. The developed model explains the main features of our experimental results.

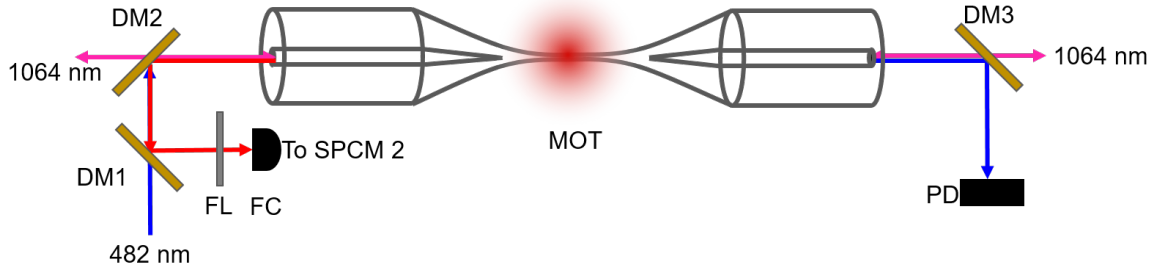


Figure 4.5: Experimental setup. DM: Dichroic Mirror. PD: Photodiode. SPCM: Single-photon counting module. FL: Optical Filter. The different coloured arrows indicate different wavelengths of light, 1064 nm: pink, 780 nm: red and 482 nm: blue, respectively.

The experiment system consists of an ONF, with a waist diameter of ~ 400 nm, that is single-mode for 780 nm, embedded in a cold atomic ensemble of ^{87}Rb , as described in Chapter 3. The ^{87}Rb atoms are cooled to ~ 120 μK using a standard MOT configuration of three pairs of retro-reflected cooling and repump beams. The 780 nm cooling beam is 14 MHz red-detuned from the $5S_{1/2}(F = 2) \rightarrow 5P_{3/2}(F' = 3)$ transition and the repump is on resonance with the $5S_{1/2}(F = 1) \rightarrow 5P_{3/2}(F' = 2)$ transition. The total powers in the cooling and repump beams are 42 mW and 2 mW, respectively. Using a magnetic field gradient of ~ 24 G/cm at the centre of the MOT, typically 10^7 atoms are trapped, and the typical Gaussian full-width-half-maximum of the MOT is 0.5 mm. The free-space MOT fluorescence is collected by the imaging system explained in Chapter 3. The MOT fluorescence that couples to the guided-mode of the ONF is separated from light of other wavelengths using an assembly of dichroic mirrors and bandpass filters, before being delivered to an SPCM. The overlap between the cold atom cloud and the ONF is optimised by maximising the photon count at the SPCM

¹This section is adapted from K.S. Rajasree, T. Ray, K. Karlsson, J.L. Everett and S. Nic Chormaic, "Generation of cold Rydberg atoms at submicron distances from an optical nanofiber", *Phys. Rev. Research* **2**, 012038 (R) (2020) *Rapid Communication* [2]. K.P. Subramonian Rajasree participated in all aspects of the experiments, collection and preparation of the data, and writing of the manuscript.

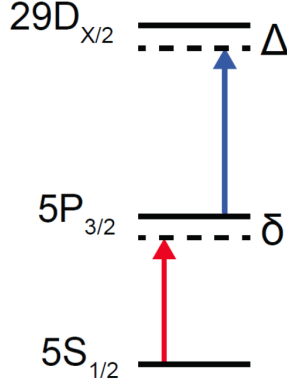


Figure 4.6: Simplified ^{87}Rb energy diagram. Atoms trapped in the MOT are excited to the $n = 29$ level by a two-photon process involving the cooling laser at 780 nm and 482 nm light in the evanescent field of the ONF.

using three pairs of Helmholtz coils. With an optimised overlap, the SPCM count is proportional to the atom density, and, hence, the PMT signal, for a given Gaussian full-width-half-maximum.

A schematic of the experimental setup is given in Fig. 4.5. During the experiment, $100 \mu\text{W}$ of 1064 nm light is passed through the ONF from each side. The Rydberg excitation is driven by a ladder-type, two-photon process, shown in Fig. 4.6. The 780 nm light is provided by the cooling beams, while the 482 nm light is derived from a Toptica TA SHG Pro system and coupled into the nanofibre. The frequency of the 482 nm laser is stabilised to a vapour cell EIT signal [78, 161] and step scanned as explained in Section 4.1.

The 482 nm light can be switched on and off using a combination of an AOM and a mechanical shutter (Thorlabs, SH1) to ensure complete cut-off (refer to Fig. 4.2). There are two AOMs in the Fig. 4.2, one of which AOM (IntraAction Corp., ATM-802DA1) is controlled by LabVIEW for switching the pump laser. This light is coupled to the ONF using a pair of dichroic mirrors (DMLP650) and interacts with the atoms in the MOT via the evanescent field. The coupling efficiencies for light of different wavelengths into the fibre patch cable differ, as do the losses at any splice regions, making it difficult to determine the exact transmission through the ONF for each wavelength used in the experiment. We, therefore, measure the power at the output pigtail of the ONF in order to estimate the power at the nanofibre waist. Unless another power is explicitly mentioned, we maintain an output power of $16 \mu\text{W}$ for the 482 nm light for all measurements. Note that, at 482 nm, the ONF supports the fundamental mode, HE_{11} , as well as the TE_{01} , TM_{01} , and HE_{21} higher order modes. The ONF is single-mode for all other wavelengths used.

The experimental sequence is simple. First, the MOT is loaded to saturation for 8 seconds. The population of the MOT at any time, t , as a fraction of the undisturbed equilibrium population, can be obtained from the PMT signal and is expressed as

$$N(t) = \frac{N_{\text{MOT}}(t)}{N_0} = (1 - e^{-\gamma_{\text{MOT}} t}), \quad (4.1)$$

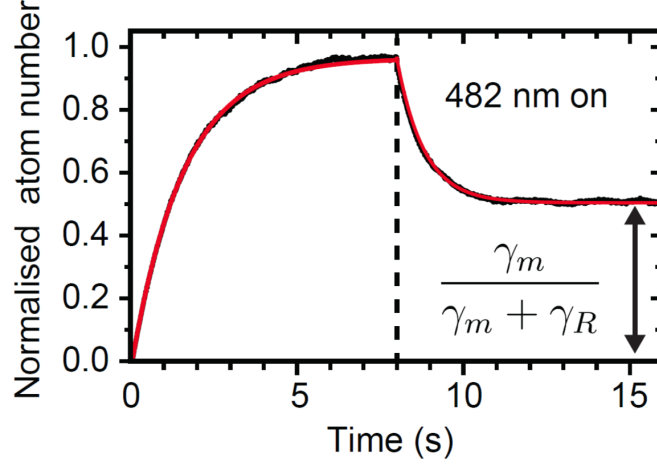


Figure 4.7: Typical loading of the MOT to a steady-state for 8 s and subsequent decay to a new equilibrium for 8 s after the 482 nm laser has been switched on.

where $N_{\text{MOT}}(t)$ is the total number of atoms in the MOT at time t and $N_0 = L_{\text{MOT}}/\gamma_{ml}$ is the steady-state number of atoms in the MOT. L_{MOT} is the loading rate of atoms into the MOT from the background vapour and γ_{ml} is the population loss rate of the MOT (for more details see Chapter 3.5). A typical loading curve is shown in Fig. 4.7 and γ_{ml} is obtained by fitting the PMT signal to Eqn. 4.1.

When the MOT is loaded to saturation, the 482 nm laser propagating in the ONF is turned on. Only those atoms in the evanescent field of the nanofibre can interact with both the 780 nm and 480 nm light and, therefore, participate in the two-photon Rydberg excitation. The newly formed Rydberg atoms leave the cooling cycle and escape from the MOT - this introduces a new population loss rate, γ_R , which includes any other loss processes, such as ionisation of atoms post Rydberg excitation. The new loss mechanism starts bleeding the MOT of atoms and a new equilibrium is established over time, determined by the total loss rate, $\gamma_t = \gamma_{ml} + \gamma_R$. The time-dependent population of the MOT can be written as

$$N(t) = 1 - \frac{\gamma_R}{\gamma_t}(1 - e^{-\gamma_t(t-t_0)}), \quad (4.2)$$

where t_0 is the time at which the 482 nm laser is switched on. The time evolution of the MOT population is fitted to Eqn. 4.2 to obtain γ_R . Assuming all atoms excited to the Rydberg state are lost from the cooling cycle, $N_0\gamma_R$ is the rate of formation of the Rydberg atoms at the moment the 482 nm laser is switched on.

For a given detuning, Δ , of the 482 nm laser from the $5P_{3/2}$ to the $29D_{X/2}$ Rydberg level, the experiment is repeated for 8 cycles to obtain mean values of γ_m and γ_R . The variation of γ_m and γ_R as a function of Δ is investigated for two Rydberg levels, namely $29D_{5/2}$ and $29D_{3/2}$. The results are presented in Fig. 4.8. Note that γ_m does not change during the experiment, ensuring that the experimental conditions also do not change. We can clearly see that γ_R shows two peaks as a function of Δ for both of the 29D levels. The two peaks, *i.e.*, P1 at $\Delta = 11.7$ MHz and P2 at $\Delta = -4.3$ MHz, correspond to two different mechanisms for the Rydberg excitation. P1 is obtained from a coherent, two-photon excitation, where a fraction of the ground-state atom population

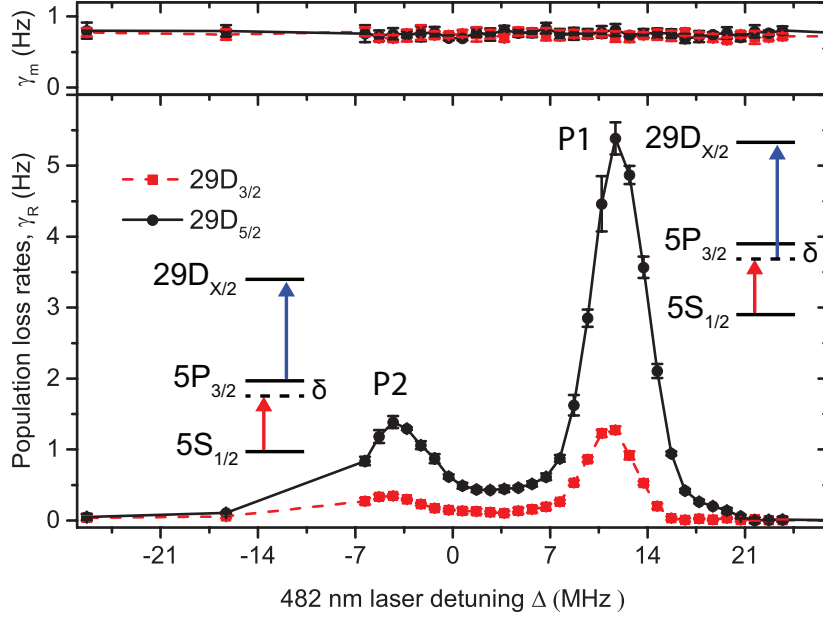


Figure 4.8: Dependence of the population loss rates, γ_m (top) and γ_R (bottom), on the 482 nm laser detuning, Δ , for a fixed detuning of $\delta = 14$ MHz for the 780 nm laser. For both levels, $29D_{3/2}$ and $29D_{5/2}$, γ_m does not change while γ_R shows two peaks. The peaks are labeled with the level schemes to indicate the coherent (P1) and the incoherent (P2) processes [134].

is coherently transferred to the Rydberg state without populating the intermediate, $P_{3/2}$, excited state. In contrast, P2 corresponds to an incoherent, two-step excitation process. The cooling laser transfers a fraction of the ground-state population to the intermediate state, $P_{3/2}$. The second photon, at 482 nm, then transfers a fraction of the $P_{3/2}$ population to the Rydberg state. In this process, the intermediate state is populated and there is no coherence established between the ground and Rydberg states. A detailed explanation of the mechanism affecting the ratio between coherent and incoherent excitations can be found in Ref. [134]. Ideally, the peaks should appear at $\Delta = 0$ and δ (the detuning of the 780 nm cooling laser). The deviation of the peaks from the expected position and separation values may arise from many factors, such as a light shift, a van der Waal's shift due to the fibre surface [30, 37, 162, 163], or a shift due to stray electric charge on the fibre surface [116], experienced by the energy levels involved in the excitation process. These effects have not been incorporated in the model presented herein. An estimate of the electric field present and its influence on the Rydberg atom lifetime is highly desirable and will be the focus of the next generation of experiments. For now, we can assume that the charge per unit length of the tapered fibre is no more than 2×10^{11} C/m [40]. This number could increase when light propagates through the fibre [41], but the polarisability of the $29D$ state indicates that the field must be limited to only a few V/cm in order to generate the Rydberg atoms at the right laser detuning. A systematic study related to the Rydberg atom formation and lifetime as a function of power in the blue beam is also desirable.

Figure 4.9 shows the variation of γ_R as a function of Δ , for three different values of the cooling laser detuning, δ . The position of the coherent peak, P1, changes with δ

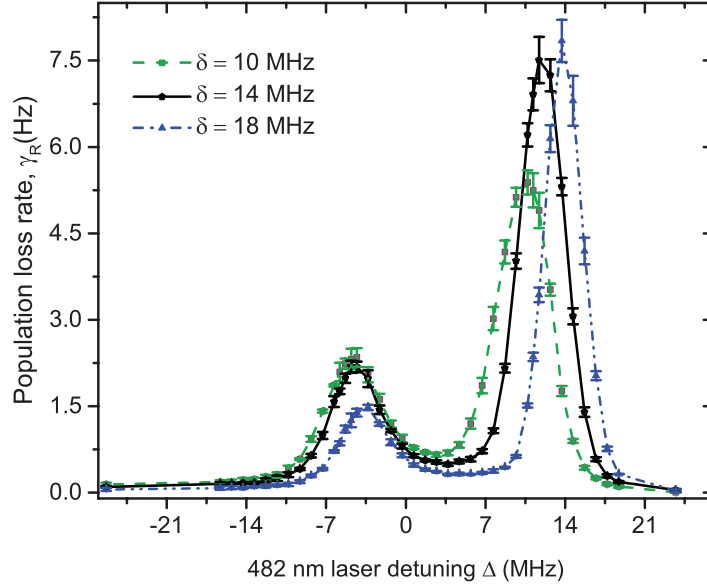


Figure 4.9: Dependence of the population loss rate, γ_R , on the 482 nm laser detuning, Δ , for three different detunings of 780 nm, i.e. $\delta = 10, 14,$ and 18 MHz, for the $29D_{5/2}$ level.

to satisfy the two-photon resonance condition. In this process, the sum of the energies of the 780 nm photon and the 482 nm photon should be equal to the energy difference between the ground and Rydberg state. The $5P_{3/2}$ intermediate state is always populated following a small change in detuning of the cooling laser. Therefore, the peak position should not change since the 482 nm photon should always have the same energy in order to couple the $5P_{3/2}$ intermediate state to the Rydberg level; however, this argument ignores other effects that could lead to energy level shifts in the experiment. As we expect, the position of P2 does not noticeably change for $\delta = 10$ MHz and 14 MHz; however, there is a small, observable shift when $\delta = 18$ MHz. A model accounting for surface and charge effects in a more realistic geometry would be needed to determine the reason for this observed shift.

Finally, we investigated the dependence of γ_R on the effective Rabi frequency of the $5P_{3/2} \rightarrow 29D_{X/2}$ transition for both the coherent and incoherent processes. To perform this experiment, δ was set to 14 MHz and Δ was set to the maximum of either P1 or P2. The power of the 482 nm laser was then varied and γ_R was measured for both peaks and both transitions. The results are shown in Fig. 4.10. We compare the dependence of the observed loss rates on the frequencies and intensities of the driving optical fields by considering a three-level density matrix model for a population of atoms driven by two coherent optical fields of constant intensity as given in Chapter 2.1.1. We use the Maxwell-Bloch equations for thermal atoms in a small interaction volume. Here, in this experiment the 482 nm laser is guided through the ONF to the MOT atoms and as the atoms interact with different intensities of the evanescent field at different distances from the ONF surface, the Rabi frequency is position dependent. We define an effective Rabi frequency, Ω_r , averaged over the atom ensemble interacting with the evanescent

field for the $5P_{3/2} \rightarrow 29D_{X/2}$ transition. We also introduce a parameter, \mathcal{A} , to represent the atoms in the interaction volume which will be discussed in detail in the following paragraphs. Using the definitions of the Rabi frequency, Ω_p , for the cooling transition, the effective Rabi frequency, Ω_r , for the Rydberg transition, detunings from resonance, Δ_p and Δ_r , and atomic operators, σ_{ij} , representing populations and coherences of all three levels, we can write:

$$\begin{aligned}
\dot{\sigma}_{ss} &= \left[i \frac{\Omega_p}{2} \sigma_{ps} + H.c. \right] + \Gamma_p \sigma_{pp} + \Gamma_r \sigma_{rr} - \mathcal{A} \left(\sigma_{ss} - \frac{1}{2} \right), \\
\dot{\sigma}_{pp} &= \left[i \left(\frac{\Omega_r}{2} \sigma_{rp} - \frac{\Omega_p}{2} \sigma_{ps} \right) + H.c. \right] - \Gamma_p \sigma_{pp} - \mathcal{A} \left(\sigma_{pp} - \frac{1}{2} \right), \\
\dot{\sigma}_{rr} &= \left[i \frac{\Omega_r}{2} \sigma_{rp} + H.c. \right] - (\Gamma_r + \mathcal{A}) \sigma_{rr}, \\
\dot{\sigma}_{ps} &= -i \Delta_p \sigma_{ps} + i \frac{\Omega_p}{2} (\sigma_{ss} - \sigma_{pp}) + i \frac{\Omega_r}{2} \sigma_{rs} - \left(\frac{\Gamma_p}{2} + \mathcal{A} \right) \sigma_{ps}, \\
\dot{\sigma}_{rp} &= -i \Delta_r \sigma_{rp} + i \frac{\Omega_r}{2} (\sigma_{pp} - \sigma_{rr}) - i \frac{\Omega_r}{2} \sigma_{rs} - \left(\frac{\Gamma_p + \Gamma_r}{2} + \mathcal{A} \right) \sigma_{rp}, \\
\dot{\sigma}_{rs} &= -i (\Delta_p + \Delta_r) \sigma_{rp} + i \frac{\Omega_r}{2} \sigma_{ps} - i \frac{\Omega_p}{2} \sigma_{rp} - \left(\frac{\Gamma_r}{2} + \mathcal{A} + \gamma_0 \right) \sigma_{rs}.
\end{aligned} \tag{4.3}$$

Here, γ_0 is the motional dephasing of the coherence, σ_{rs} . For a MOT temperature of 120 μK and a coherence generated by a cooling beam perpendicular to the nanofibre axis, $\gamma_0 = 600 \pm 200$ kHz. Other motional dephasings are ignored. The $+H.c.$ terms indicate that the Hermitian conjugates of the terms in $[\]$ are also included. The thermal motion of atoms into and out of the interaction volume removes atoms from the populations and coherences at a rate \mathcal{A} and places them in a mixture of roughly $s\sigma_{ss} + p\sigma_{pp}$ with s and p determined by Ω_p and Δ_p . The model ignores other aspects of the experimental geometry. Ω_p is fitted from the splitting of P1 and P2, and Ω_r is fitted to the P1 and P2 height data. The decoherence rates are fitted to the widths of P1 and P2.

The mixing rate, \mathcal{A} , is an important parameter for describing this experiment. The introduction of atoms in a mixed state to the interaction region boosts the incoherent production of Rydberg atoms well beyond that expected in a coherently driven system. The mixing rate may be changed experimentally by changing the cooling field detuning and thus the temperature of the atoms. The effect of this can be seen in Fig. 4.9, where a closer detuned trap with hotter atoms has a higher mixing rate and a larger incoherent peak to coherent peak height ratio than a further detuned, cooler trap.

The population of Rydberg atoms in the model, σ_{rr} , is related to the experimental loss rate, γ_R , by estimating the proportion, \mathcal{P} , of atoms in the MOT that are also in the evanescent field and multiplying by the mixing rate: $\mathcal{P}\mathcal{A}\sigma_{rr} \approx \gamma_R$. The value of \mathcal{P} is set to $\mathcal{P} = (3 \pm 1) \times 10^{-4}$ to fit the model to the experimental data in Fig. 4.10, and this value also agrees with other experimental observations. It corresponds to an interaction region extending about 100 - 200 nm from the fibre surface, noting that the $1/e$ decay length of the evanescent field of the fundamental mode of 482 nm light is 125 nm. The mixing rate, \mathcal{A} , is set to 0.6 MHz to fit the ratio of the incoherent to

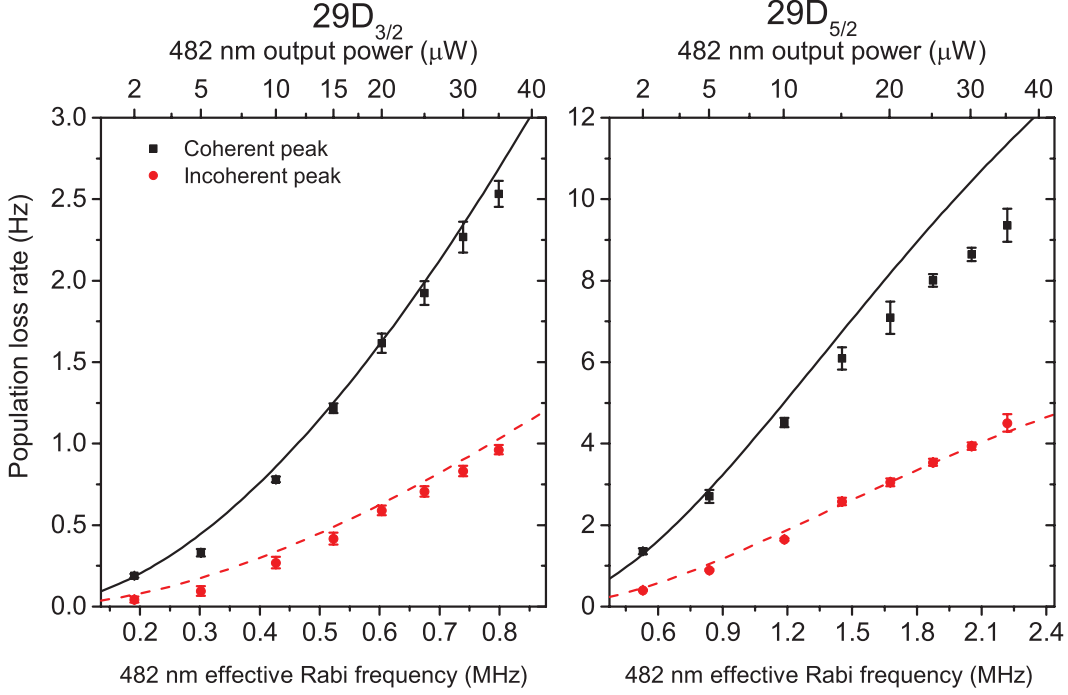


Figure 4.10: The dependence of γ_R for the coherent (P1 black) and incoherent (P2 red) excitation on the power of the 482 nm pump laser and, hence, the effective Rabi frequency for $29D_{3/2}$ (left) and $29D_{5/2}$ (right). The solid lines are solutions to the three-level model.

coherent peak heights in Fig. 4.10. This value is also consistent with the average flight time of atoms at $120 \mu\text{K}$ through an interaction region with a diameter, $d = 200 \text{ nm}$, where $\mathcal{A} \approx \bar{v}/d$, with \bar{v} the average speed of the atoms.

The experimental loss rate clearly follows the theoretical curve at low γ_R , but diverges from the model above rates of 5 Hz. This may be due to production of Rydberg atoms beginning to saturate as $\sigma_{rr} \rightarrow 1$. This is not observed in the model, with a Rydberg population at P1 of $\sigma_{rr} = 0.033$ for $\Omega_r = 1.25 \text{ MHz}$, which is well below saturation. The model only includes one cooling field, with a Rabi frequency equal to that of one cooling beam. Ω_r is assumed to be constant, whereas, in the experiment, atoms are subject to a time-varying interaction as they travel through the evanescent field. Averaging over these trajectories may give a more accurate relationship between the 482 nm intensity and the effective Ω_r . The model also assumes that all atoms leaving the interaction region while in the Rydberg state are lost from the MOT. However, considering the lifetime of the Rydberg states and the temperature of the atoms, a significant proportion of these atoms could actually be recaptured directly into the MOT if they decay into the cooling cycle. Experimental determination of the saturated loss rates under different conditions and for different \mathbf{n} levels could allow any processes interfering with recapture, such as ionisation, to be observed. However, despite its simplicity, the model explains most of our observations and confirms the production of Rydberg atoms in the evanescent field of the nanofibre.

4.3 Trap Loss Studies with $31S_{1/2}$ Rydberg Atoms

In this section, we study the results obtained when the Rydberg laser is addressing the $31S_{1/2}$ level rather than the $29D_{X/2}$ level as discussed in Section 4.2. The methods are as discussed in the previous section. The MOT was loaded to saturation for 8 s and the 482 nm laser was turned on. The trap loss was monitored when the 482 nm laser was step-scanned around $31S_{1/2}$. When the 482 nm laser detuning (Δ) is 11.7 MHz, *i.e.*, around the peak, P1, we observed for $29D_{X/2}$, we see a difference in the trap loss curve. For different 482 nm laser detunings (see Fig. 4.11), this behaviour is observed till the detuning of the 482 nm laser is 14.3 MHz. As the detuning increases, we see the delay to initiate the decay gets longer. The delay is not repeatable for higher detunings and as the detuning decreases then the delays are same, as seen from Fig. 4.11. There is the possibility of two decay processes, where one causes slow decay of the atoms and the other is a sudden decay of atoms from the trap.

Except for these range of values of frequency detunings (11.7 MHz to 14.3 MHz) of the 482 nm laser, we obtain similar curves for the trap loss rate with the 482 nm laser detuning (see Fig. 4.8). However, it is interesting to note that this discrepancy near the coherent Rydberg excitation peak. The possible reasons for the behaviour could be either Rydberg blockade or ionisation. Studies have shown ionisation affects the Rydberg population. The ion accumulation produces an electron trap, which restricts further production of Rydberg atoms. The authors of [164] experimentally showed that Rydberg atoms excited to S-levels are less likely to collide and ionise compared to D-level Rydberg atoms. This might be a reason accounting for the delayed decay we observe for the S-level compared to the D-level experiments.

The trap loss measurements we performed relies on atoms lost from the MOT. A study should be done to find the influences of the ONF on the Rydberg level to analyse the different possible reasons. Rydberg EIT could be a helpful tool to help answer the question.

4.4 Dual-Scan Rydberg EIT in Cold Atom-ONF System

From the experiments already discussed in this chapter, we concluded that the excitation of a neutral ground state atom to a Rydberg state can result in a loss from the trap. In [165], the authors studied Rydberg EIT in cold atomic sample, where they show that the interactions among Rydberg atoms can manifest as a depopulation of the Rydberg state. They used nonlinear Bloch equations with density dependent decay terms to model the losses from the Rydberg state. In the following series of experiments, we were motivated to study the ONF:atom system using Rydberg EIT and to find the role of the ONF interaction with the Rydberg level and how it influences the properties of the Rydberg atom. The ONF may be an important factor resulting in the depopulation of atoms.

In a typical EIT experiment, the pump is locked to the resonance and the probe light is scanned around the resonance. Here, we use a 482 nm laser as pump and the probe laser is 780 nm. Information on the atomic population can be studied by using a

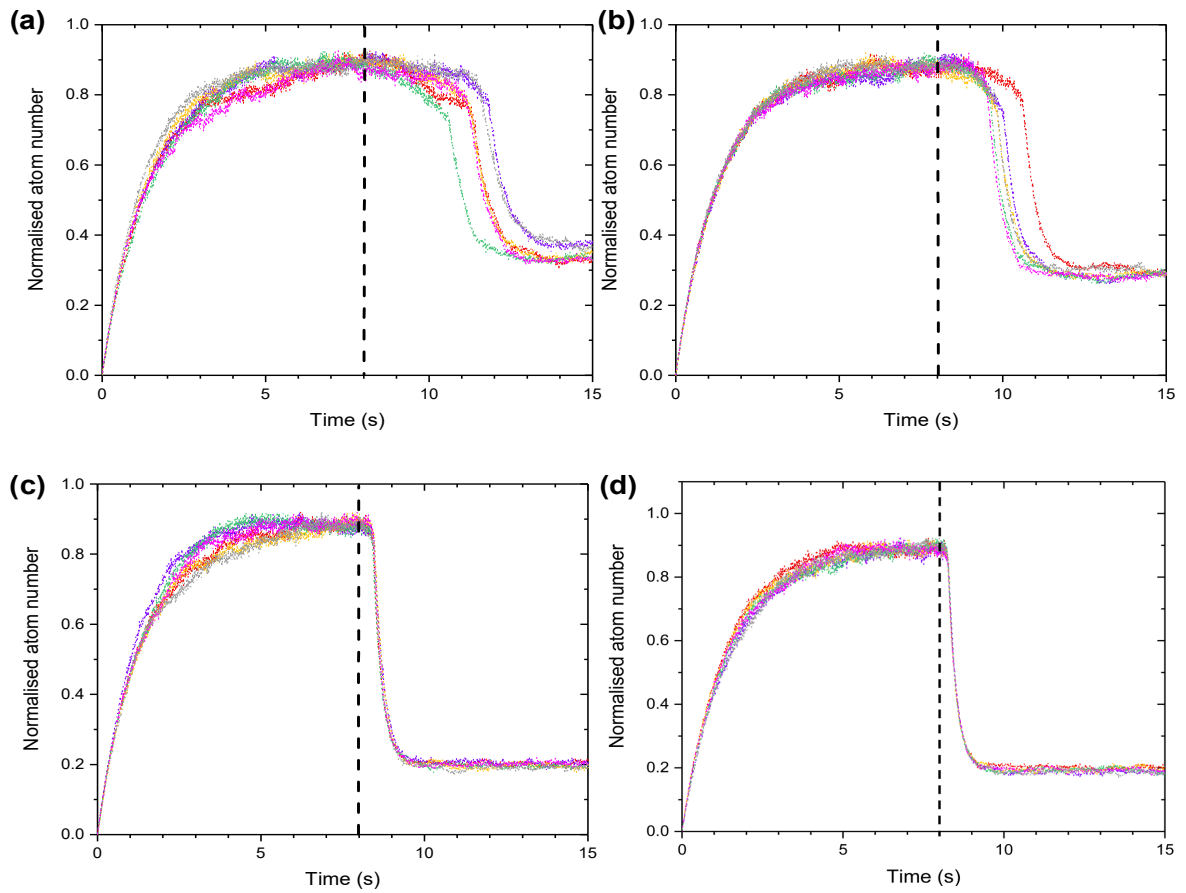


Figure 4.11: Loading of the MOT to a steady-state for 8 s and decay to a new equilibrium for 8 s after the 482 nm laser has been switched on (indicated by dashed vertical line). The 482 nm laser detuning (Δ) is (a) 14.3 MHz (b) 13.7 MHz (c) 12.5 MHz (d) 11.7 MHz.

dual-scan of the probe detuning as it is ramped up and down at a faster rate. A series of experiments were planned to study this scenario in our system. The initial idea was to realise the experiment in the cold atom system and then to move to the ONF-based experiments, allowing us to compare free-space with the role of the ONF. In this series of experiment, we use an optical molasses (OM) technique, an additional step to cool the atoms.

The atoms were loaded to the OM from the MOT. The cold atoms in the MOT stage were prepared as described in Chapter 3 and we ensured a good overlap between the MOT and the ONF before the molasses stage. The timing sequence to prepare OM is given in Fig. 4.12. Using this technique, the ^{87}Rb are cooled down to $20\ \mu\text{K}$. We observed the position of the optical molasses with respect to the nanofibre via two cameras and monitored the fluorescence coupled through the ONF via an SPCM. Isotropic expansion of the cold atomic cloud is ensured as otherwise atoms may leave the nanofibre region.

After 30 ms of molasses, the cooling laser is turned off. The pump and probe are turned on simultaneously. We use the same 482 nm laser as pump, as explained in Section 4.1. The pump laser is turned on with an AOM (IntraAction Crop., ATM-802DA1) and a mechanical shutter (Thorlabs, SH1) (see Fig. 4.2). The probe, 780 nm light, is derived from an ECDL (DL100, Toptica) and the frequency is locked to $5S_{1/2} (F = 3) \leftrightarrow 5P_{3/2} (F' = 2)$ using saturation absorption spectroscopy (Cosy, Toptica). The 780 nm light is fed to a double-pass AOM (IntraAction Crop., ATM-1102DA2B) configuration. The 482 nm laser is frequency locked to the $5P_{3/2} \leftrightarrow 30D_{X/2}$ transition using the vapour cell EIT setup explained in Section 4.1. The 780 nm laser is scanned in frequency (± 16 MHz) around the $5S_{1/2} \leftrightarrow 5P_{3/2}$ resonance twice, *i.e.*, a ramp up and a ramp down in 2 ms. The faster scan is preferred to discard the possibility of the atoms being lost from the OM. The power variation due to frequency scanning of the probe light is compensated by giving an amplitude modulation input to the AOM of the probe light. We used a custom-built saturated absorption spectroscopy setup to obtain the reference signal for the experiment.

Initially, we sent both the probe and pump through free-space to the cold atoms. This set of experiments will be referred to as the free-space experiments. In the ONF-based excitation scheme, we studied Rydberg EIT in two steps. In the first set of fibre-based experiments, the probe light was sent through the ONF and the 482 nm laser was delivered to the interaction region through free-space. In the second case, we sent both the light beams through the ONF.

4.4.1 Free-Space, Dual-Scan Rydberg EIT Experiment

The schematic of the setup is given in Fig. 4.13. The 780 nm light is sent through the cloud of atoms. Alignment with the MOT is done while monitoring the absorption spectrum signal of the 780 nm light. A collimated beam of 482 nm light of radius 4 mm is also sent through the atom cloud and reflected back through it using a mirror. The transmission of the 780 nm beam is studied using an avalanche photodiode (APD120A, Thorlabs). The background on the avalanche photodiode is eliminated using dichroic mirrors (DMLP650), which reflect the 482 nm light, and a 780 nm filter (Thorlabs FB780-10).

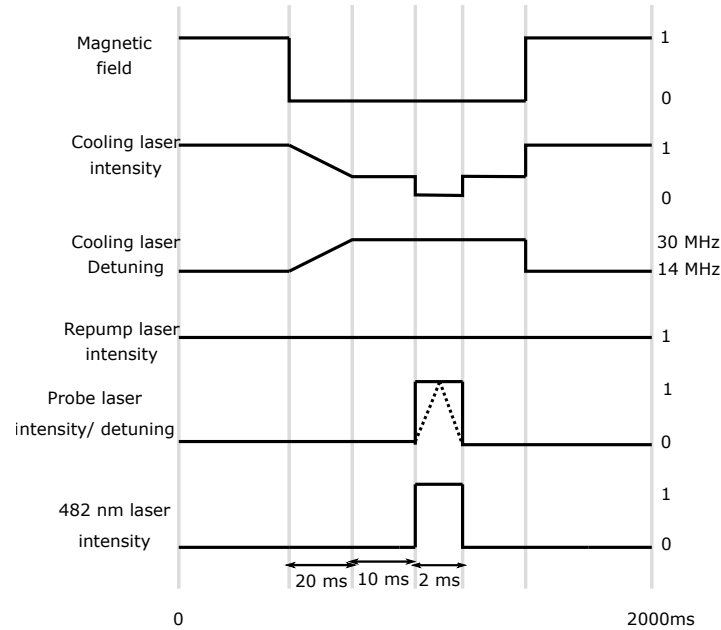


Figure 4.12: Experimental sequence for the dual-scan Rydberg EIT experiments. Note that the time intervals are not to scale.

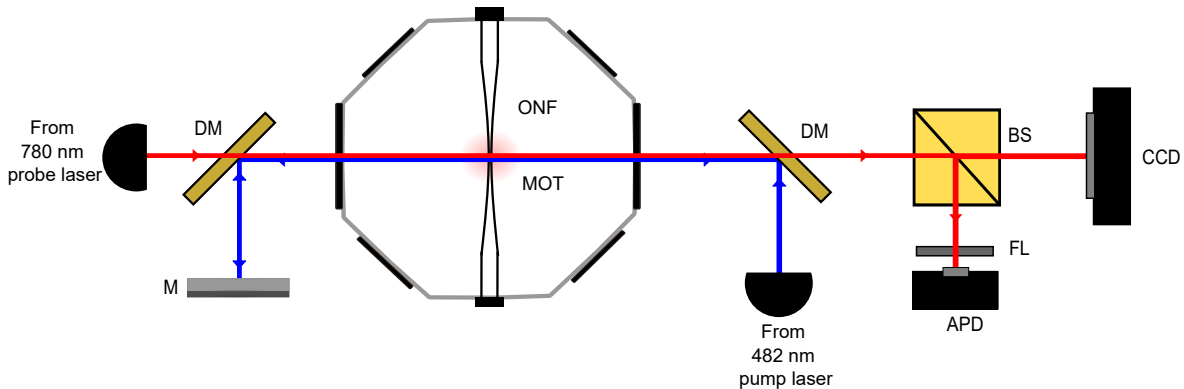


Figure 4.13: Schematic of the free-space Rydberg EIT experiment: Pump and probe are propagating in free-space. M: Mirror. DM: Dichroic mirror. BS: Beam splitter. FL: Filter. APD: Avalanche Photodiode. CCD: Charged coupled device. The different coloured arrows indicate different wavelengths of light, 780 nm: red and 482 nm: blue, respectively.

The transmission of the probe is modified in the presence of the pump light. A typical EIT spectrum obtained for a pump power of 80 mW and probe power of $1\mu\text{W}$ is given in Fig. 4.14. The shown spectra are averages of 20 experimental runs. We define the EIT ratio as the transmission of 780 nm light in the absence of pump light divided by the transmission of 780 nm light in the presence of pump light. Using the dual-scan technique, we can observe the EIT ratio is reduced in the second scan. This reduction indicates that atoms excited to the Rydberg levels are lost. The trend of the loss with

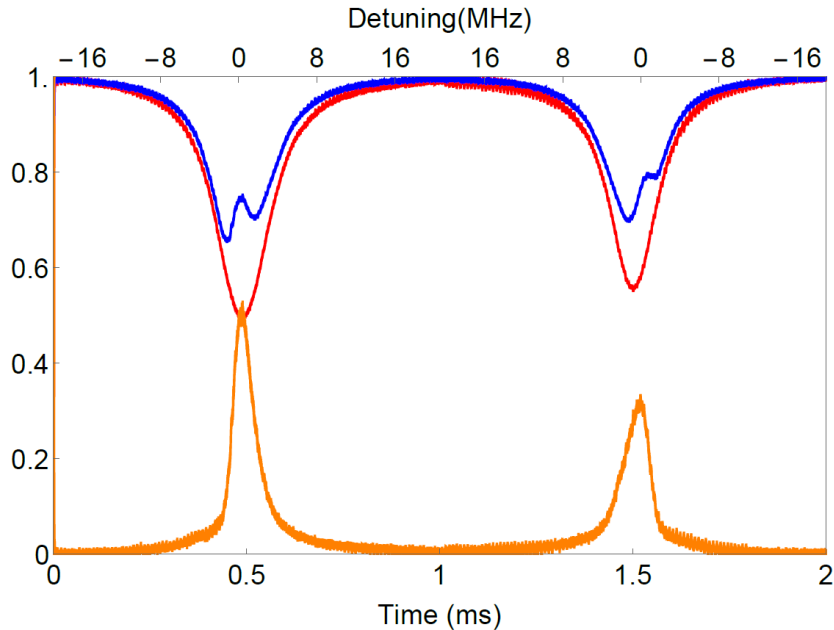


Figure 4.14: Typical free-space, dual-scan Rydberg EIT spectrum obtained as 780 nm laser is scanned. Transmission spectrum of the 780 nm light in the absence (red curve) and in the presence of the 482 nm pump light (blue curve). The orange curve is the EIT ratio, which is an indication of the population of the Rydberg level.

respect to the probe power is shown in Fig. 4.15. We observe that the lower probe power facilitates low population loss. The population loss was modelled using time-dependent, four-level Bloch equations. Preliminary theoretical modelling was done by Dr. Albert Benseny, Quantum Systems Unit in OIST. This set of observations act as the control set where the ONF interaction is negligible.

4.4.2 ONF-Based, Dual-scan Rydberg EIT Experiments

Once the free-space experiments were completed, the next step was to add the ONF into the experiment. In the first case of the ONF-based experiments, the nanofibre delivers the probe light to the atoms. The probe light's evanescent field extends ~ 200 nm from the fibre surface. As in the free-space experiments, the retro-reflecting pump beam passes through the nanofibre field region, so that there will be a region created where both pump and probe light overlap and interact with the cold rubidium atoms. Only those atoms in the evanescent field can contribute to the process.

This Rydberg EIT experiment was carried out in a similar fashion to the free-space experiment from Section 4.4.1. The probe was detuned ± 16 MHz around the resonance in 1 ms. The probe light transmission was detected with an SPCM at an integration time of $10 \mu\text{s}$. The transmitted 780 nm light on the SPCM in the presence of the pump is given in Fig. 4.16. Even though no Rydberg EIT signal was observed the absorption of the 780 nm light is clearly reduced. The effect was studied when the pump laser was addressing either $30D_{5/2}$ or $30D_{3/2}$. The reduction of the absorption was less when the pump was locked to $30D_{3/2}$ reflecting the different transition probabilities from $5P_{3/2}$.

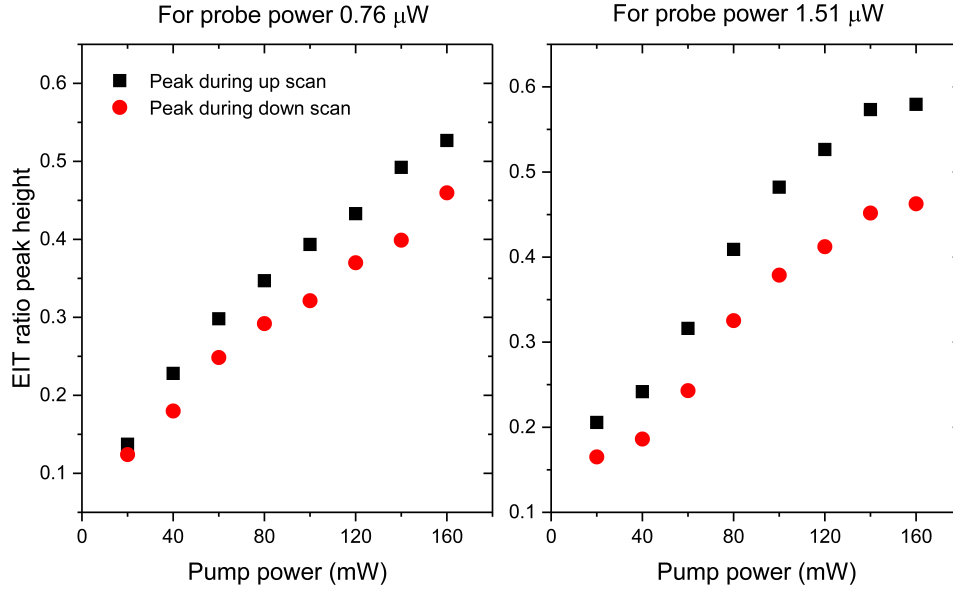


Figure 4.15: The dependence of the EIT ratio peaks as a function of the 482 nm pump power and for different probe powers: $0.76 \mu\text{W}$ (left) and $1.51 \mu\text{W}$ (right).

We see that the absorption of 780 nm decreases with pump power (see Fig. 4.17). One of the drawbacks of this experiment is that the overlap between the pump and probe light is small and the next logical step was to send the pump light through the ONF to increase the overlap.

In the second set of ONF-based Rydberg excitation experiments, the light from both the 780 nm and 482 nm lasers was sent through the fibre along with the 1064 nm light. When initial tests were done with only the pump and probe through the ONF, the probe light transmission started diminishing. The probe light transmission recovered when 1064 nm light was sent through the ONF ($100 \mu\text{W}$ at output). Dichroic mirrors (DMLP650, DMLP950) were used at the output of the ONF to suppress the 482 nm and 1064 nm light from the detected signal. However, despite several attempts, the experiments did not yield a clear Rydberg EIT signal. A possible reason could be the position of the atoms is not well-defined. The pump beam and probe beams overlap and the effective Rabi frequency is crucial in realising the Rydberg EIT. Hence, deterministically placing the atoms at a defined distance from the nanofibre surface via nanofibre-based dipole trapping may help in obtaining a better signal.

4.5 Conclusions

We have reported on the generation of Rydberg atoms in a ^{87}Rb cold atom ensemble surrounding an ONF, for first time to our knowledge. By comparing the atom loss rate to the Rydberg population using a simple 3-level density matrix model, we were able to closely model the experimental data and estimate the size of the interaction region. Excitation of the Rydberg atoms was mediated via the ONF and they were generated at no more than a couple of 100 nm from the fibre surface where overlap between the two

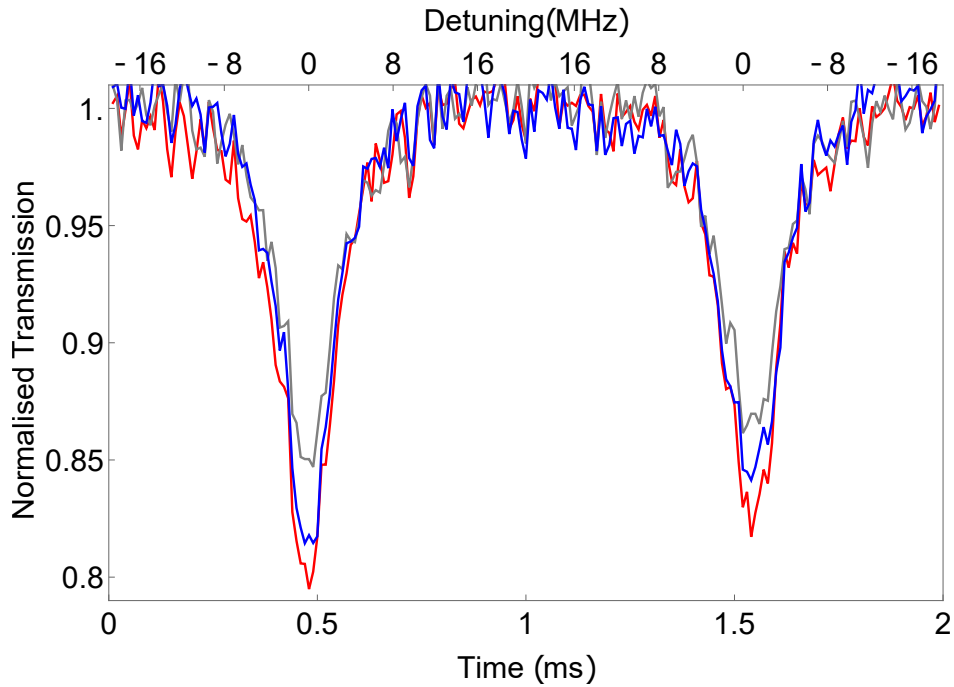


Figure 4.16: Transmission of the 780 nm light through the ONF in the absence of pump light (red curve). The transmission is modified when the pump laser is locked to $5P_{3/2} \leftrightarrow 30D_{3/2}$ (blue curve) and $5P_{3/2} \leftrightarrow 30D_{5/2}$ (grey curve).

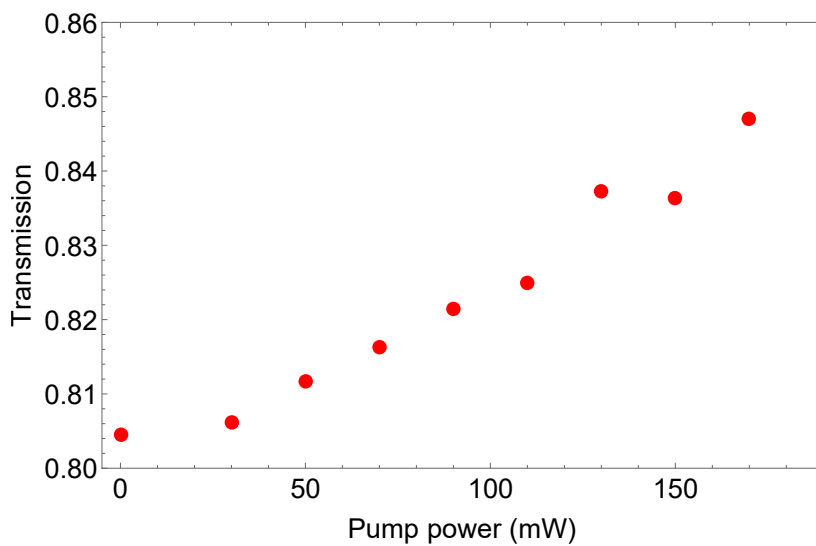


Figure 4.17: Transmission of 780 nm light through the ONF as a function of different pump powers. The pump 482 nm laser, is locked to $5P_{3/2} \leftrightarrow 30D_{5/2}$ transition.

excitation fields (780 nm and 482 nm) is maximum. This is an important advancement on earlier experiments related to Rydberg atom generation close to dielectric surfaces [108, 117] and opens up many avenues of research, such as all-fibred quantum networks using Rydberg atoms, excited atom-surface interactions at submicron distances, including van der Waal's interactions, effects on the Rydberg blockade [166] in this new regime, stray electric field effects from the dielectric nanofibre on energy levels and lifetimes of the atom, and the limitation of the maximum excited state (n value) that can be generated close to the nanofibre due to the atom size increasing quadratically with n .

The versatility of this atom-nanofibre hybrid system could be extended to explore three-step Rydberg excitations [167] where the fibre would be single-mode for the wavelengths of light used to drive the atomic transitions. Hence, the mode overlap in the evanescent field would be increased and Rydberg generation efficiency should be improved. In addition, a comprehensive study of the coherent interactions in a MOT-ONF system could extend this experimental technique beyond a qualitative confirmation towards an investigation of the behaviour of Rydberg or other exotic states, *e.g.* Rydberg polarons [168], adjacent to ONFs.

The Rydberg EIT experiment maps the properties of the Rydberg level onto the optical signals and can be used to study interactions between atoms or atoms and surfaces. Initial steps to study Rydberg EIT were carried out in the ONF:atom system. Preliminary studies indicate that the Rydberg EIT signals could be improved by controlling the distance of the atoms from the fibre. This can be achieved either by employing nanofibre-based dipole traps or having a single atom optical tweezers setup and bringing the atom closer to the ONF [169, 170].

Chapter 5

Single-Frequency, Two-Photon Transition in Rubidium using 993 nm

In Chapter 4, we concluded that nanofibre trapping may help to increase the signal quality coupled from Rydberg atoms to an optical nanofibre. One of the crucial parameters of ONF-guided light that we need to control for experiments like ONF-based atom trapping, is the polarisation at the fibre waist. In this chapter, we introduce a method that achieves polarisation compensation for the ONF-guided light when in a vacuum chamber. In order to test the polarisation compensation, we relied on a polarisation-dependent atomic process, which is based on a single-frequency, two-photon process. We start with a discussion of the two-photon process excited with light of single frequency tuned between two S levels in rubidium. Next, we demonstrate two-photon absorption in hot Rb vapour and in cold ^{87}Rb atoms mediated via the ONF. We discuss the theoretical predictions for the polarisation-dependency of the single-frequency, two-photon transition when the exciting light is sent through ONF and verify the polarisation compensation scheme via the theoretical study.

5.1 S \rightarrow S Two-Photon Transition in Rubidium¹

Two-photon processes in atomic systems have several distinct advantages over single-photon processes. For example, two-photon processes can give direct access to optical excitations that would be electric-dipole forbidden for a single-photon process [171]. Furthermore, when the two photons are derived from two laser beams in a counter-propagating configuration, a judicious choice of the polarisations can yield background-less, Doppler-free spectra [172, 173]. In addition, two-photon transition frequencies for S \rightarrow S transitions are insensitive to magnetic fields below the Paschen-Back domain [174], while two-photon transitions to metastable states have extremely

¹This section and the following section are based on "Simple, narrow and robust atomic frequency reference at 993 nm exploiting the rubidium (Rb) $5S_{1/2}$ to $6S_{1/2}$ transition using one-colour two-photon excitation", T. Nieddu, T. Ray, K.S. Rajasree, R. Roy and S. Nic Chormaic, *Opt. Express* **27**, 6528 (2019) [1]. The data shown in Section 5.2 were collected by T. Nieddu and plotted by K.P. Subramonian Rajasree. The paper is given in Appendix B.2. The results which are important for the thesis are discussed herein.

narrow linewidths compared to those for single-photon processes [175, 176]. These unique features make two-photon spectroscopy a powerful tool for precision measurements. Following the first observation of a two-photon transition in an atomic system containing caesium [177], numerous different atomic transitions have been investigated [178–184]. The technique has been extensively used for metrology and the accurate determination of fundamental constants [185, 186], as a frequency reference [187], and in quantum telecommunications [188].

The $5S_{1/2} \rightarrow 6S_{1/2}$ transition in Rb has been previously accessed with a two-frequency, two-photon excitation scheme, *i.e.*, using 795 nm and 1324 nm [189, 190]. Accessing the $6S_{1/2}$ level via the single-frequency two-photon method should help to improve the accuracy, since only a single laser is necessary for the excitation. In this chapter, we explore the single-frequency, two-photon $5S_{1/2} \rightarrow 6S_{1/2}$ transition initiated with 993 nm light. The atomic level diagram is shown in the Fig. 5.1. The excited atoms from $6S_{1/2}$ decay to $5S_{1/2}$ through two routes either through $5P_{1/2}$, emitting 1324 nm and 795 nm or $5P_{3/2}$, emitting 1367 nm and 780 nm. The hyperfine splitting of $6S_{1/2}$ is 0.7 GHz for ^{85}Rb and 1.6 GHz for ^{87}Rb . As dictated by the selection rules for a two-photon transition between two S-levels, $\Delta F=0$ and $\Delta m_F=0$. The allowed transitions for ^{85}Rb are $F=2 \rightarrow F'=2$ and $F=3 \rightarrow F'=3$. For ^{87}Rb , the allowed transitions are $F=1 \rightarrow F'=1$ and $F=2 \rightarrow F'=2$. The detection scheme employed in the series of experiments reported here is done by collecting the spontaneously emitted photons from $5P_{3/2}$ and $5P_{1/2}$.

The first order Zeeman shifts experienced by the same hyperfine states of the $5S_{1/2}$ and $6S_{1/2}$ levels are identical since they have the same hyperfine Landé g-factors. This feature renders the frequency of the $5S_{1/2} \rightarrow 6S_{1/2}$ transition insensitive to stray magnetic fields. The transition frequency is also less sensitive to electric fields compared to transitions to nonzero angular momentum states (where $L > 0$). These features make the transition an attractive choice for a frequency reference. The excitation scheme presented herein enables the conversion of two near-infrared photons at 993 nm into a telecommunication a O-band photon, at either 1324 nm or 1367 nm, and another near-infrared photon, at 795 nm or 780 nm, respectively.

5.2 Single-Frequency, Two-Photon Spectroscopy in a Rubidium Vapour Cell

In this section, we demonstrate the observation and Doppler free spectroscopic study of the $5S_{1/2} \rightarrow 6S_{1/2}$ two-photon transition in a hot Rb-atom vapour using a single-frequency laser beam. To our knowledge, this was the first observation of this particular Rb transition using single-frequency, two-photon excitation.

Doppler-free two-photon spectroscopy

Atoms in thermal motion causes Doppler broadening of spectroscopy signals. Atoms moving at different velocities see light of a fixed frequency at different frequencies due to the Doppler effect, thereby increasing the absorption linewidth. In one-photon pro-

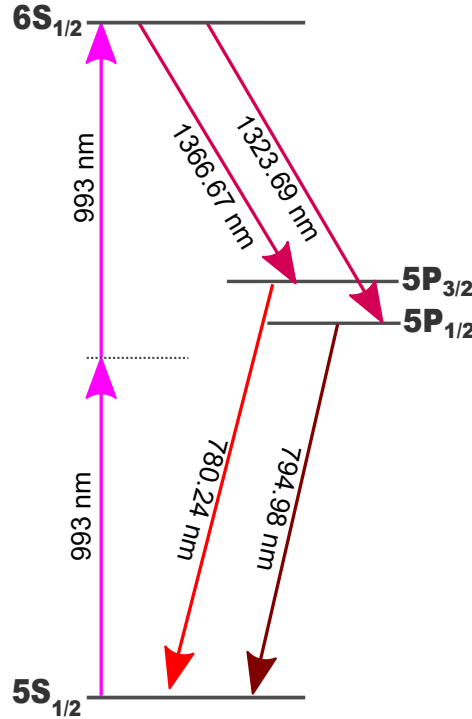


Figure 5.1: Energy level diagram for the 993 nm two-photon absorption between $5S_{1/2}$ and $6S_{1/2}$.

cesses, this broadening is overcome by using techniques such as Lamb dip spectroscopy. In two-photon spectroscopy, the Doppler effect can be eliminated easily by introducing a counter-propagating beam. To understand the method, let us consider an atomic two-photon transition, which is initiated with a laser of frequency ω and wave vector k . Assuming the atom is moving with velocity, v , then the Doppler shift is given by $k \cdot v$. An atom moving towards the beam sees the laser beam frequency as $(\omega + k \cdot v)$ and an atom moving in the same direction as the laser sees $(\omega - k \cdot v)$. The resonance condition to excite the atom from the ground state to the excited state is given as

$$E_e - E_g = \hbar(\omega + k \cdot v) + \hbar(\omega - k \cdot v) = 2\hbar\omega. \quad (5.1)$$

Hence, the atoms in the sample encountering the counter-propagating signal contribute to the spectroscopy signal regardless of their velocities. Generally, the lineshape of the Doppler two-photon transition is Lorentzian. When the speed of an atom is low, it can simultaneously absorb two photons which are co-propagating. Here, the Doppler shift of the photons does not cancel and results in a Doppler background. Atoms with low speed are few in number, hence the number of atoms contributing to the Doppler-broadened signal is less than to the Lorentzian lineshape and this can be observed in the spectra. Appropriate selection of the polarisation of the light can eliminate the Doppler background [129].

The schematic of the vapour cell experiment is given in Fig. 5.2. A continuous wave (CW) Ti-Sapphire laser (M Squared SolsTiS) is used as the source for 993 nm light, where the frequency is stabilised using a reference cavity and monitored using a wavelength meter (HighFinesse, WS-6). An optical isolator placed in front of the

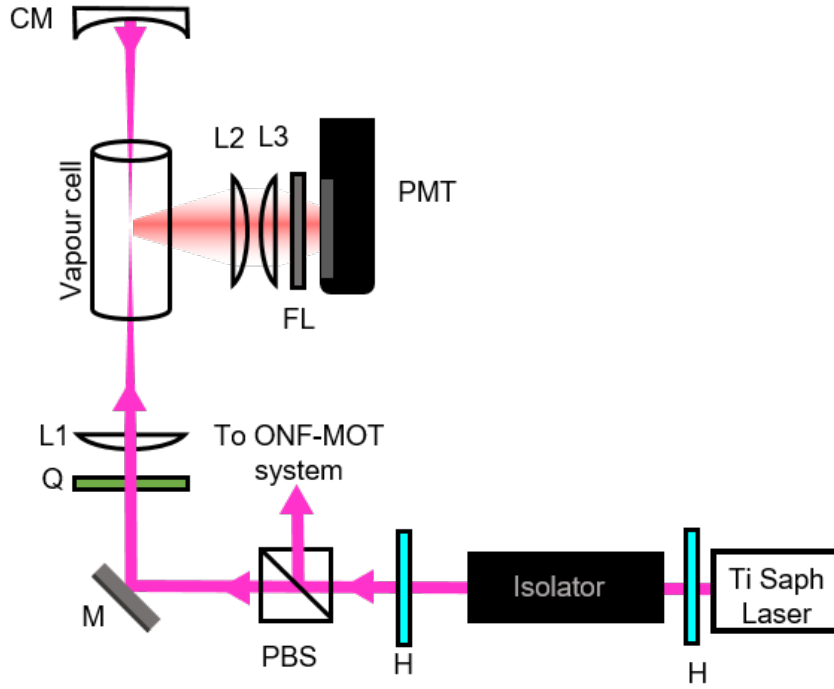


Figure 5.2: Schematic of the experimental setup. M: Mirror. L1-L3 Plano-convex lens. H: Half-wave plate. Q: Quarter-wave plate. PBS: Polarising beam splitter. CM: Concave mirror. PMT: Photomultiplier tube. FL: Optical filter.

laser ensures there are no back reflections into the laser. A part of the 993 nm light from the laser is sent to the vapour cell containing a mixture of ^{85}Rb and ^{87}Rb in their natural abundances, whereas the other part of the 993 nm light is fed to the ONF. The experiments involving the ONF will be discussed in later sections. During the experiment, the vapour cell is maintained at 130°C . A 993 nm laser of 150 mW is focussed on to the vapour cell using L1 ($f=150$ mm). The beam diameter is $128\ \mu\text{m}$, measured using a beam profiler (Thorlabs, BC106VIS). Using a concave mirror (CM, $f_{\text{CM}}=75$ mm), placed at $2f_{\text{CM}}$ from lens L1, the beam is retro-reflected. A quarter-wave plate (QWP) is used at the input to control the polarisation of the 993 nm light. The emitted 780 nm and 795 nm fluorescence is collected using the telescope assembly made from lenses (L2, L3, $f=50$ mm) and a photomultiplier tube (PMT, Hamamatsu, R636-10) in conjugation with a filter (FL, FESH0800). The fluorescence intensity is a measure of the two-photon transition rate. The quantum efficiencies of the PMT at 780 nm and 795 nm are 9% and 8% respectively. The setup is also used to obtain a reference signal for the experiments explained later in this chapter.

Electric dipole allowed, two-photon transitions from S to S levels obey the selection rules $\Delta F = 0$ and $\Delta m_F = 0$ [191]. This results in only two allowed transitions for each Rb isotope, *i.e.*, $^{87}\text{Rb } F = 2 \rightarrow F' = 2$, $^{85}\text{Rb } F = 3 \rightarrow F' = 3$, $^{85}\text{Rb } F = 2 \rightarrow F' = 2$, and $^{87}\text{Rb } F = 1 \rightarrow F' = 1$. A typical spectrum obtained is shown in Fig. 5.3. Here, excitation to the $6S_{1/2}$ level is obtained by scanning the frequency of the 993 nm laser. Doppler broadened spectrum is obtained when we block the retro-reflected beam (see Fig. 5.3 top panel), whereas using the same linear polarisation for the forward and

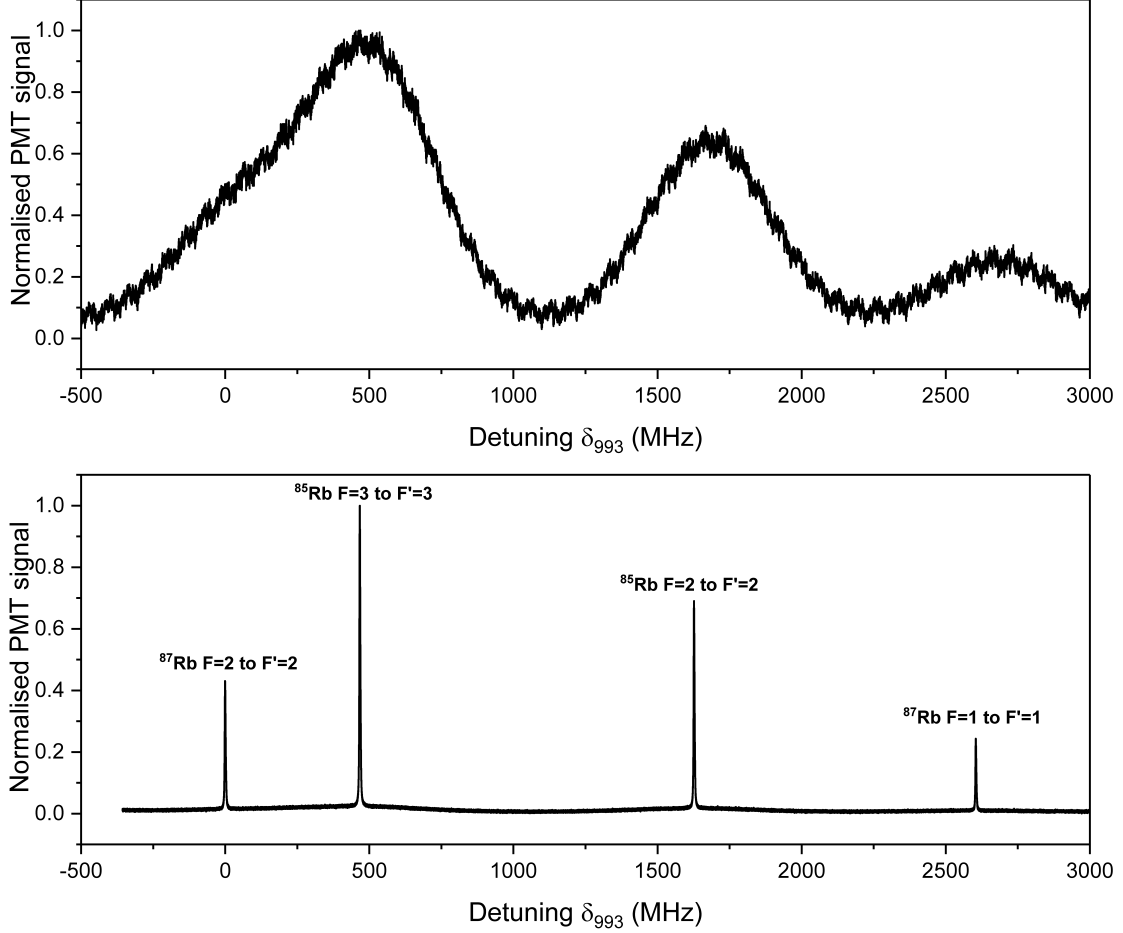


Figure 5.3: Typical Doppler-broadened signal (top) and Doppler-free (bottom) signals obtained by scanning the frequency of the 993 nm pump beam and recording the signal on the PMT. Each peak indicates a hyperfine transition as labeled.

retro-reflected beams to generate the two-photon process, we observe Doppler-free, two-photon spectrum (see Fig. 5.3 bottom panel). Note that the simple setup presented here does not measure the absolute frequency of the transition. The hyperfine splitting of the $6S_{1/2}$ level is obtained from Ref. [189] using a resonant intermediate level. The relative frequency difference is obtained by setting the frequency of the first peak, *i.e.*, the ^{87}Rb $5S_{1/2}, F = 2 \rightarrow 6S_{1/2}, F' = 2$ transition, to zero, see Fig. 5.3.

5.3 Single-Frequency, Two-Photon Spectroscopy in a MOT-ONF system

Once the vapour spectroscopy, as described in Section 5.2, was established, the next step was to study the single-frequency, two-photon excitation mediated by an ONF in

cold atoms. The experiment is carried out in the ONF- MOT system introduced in Chapter 3. The MOT is prepared with a typical average density of 10^{10} atoms per cm^3 and a temperature of $120 \mu\text{K}$. Fine overlap of the MOT with the ONF is ensured by checking the fluorescence coupled to the ONF. Recalling that the combined action of the cooling and repump lasers causes the number of atoms to cycle between $5S_{1/2}F = 2 \rightarrow 6S_{1/2}F' = 2$, the atoms in the level $5S_{1/2}F = 1$ get depleted with time. Hence, we focus on the transition $5S_{1/2}F = 2 \rightarrow 6S_{1/2}F' = 2$ in ^{87}Rb for the rest of the experiments discussed in this chapter.

The 993 nm light, which is derived from the Ti:Saph laser, is divided with one part going to the vapour cell spectroscopy setup as already discussed and the other arm going to the ONF as shown in Fig. 5.4. The signal from the vapour spectroscopy setup serves as a reference for the cold atom experiment. Each pigtail of the ONF is spliced to patch fibres. The 993 nm beams are coupled into the ONF assembly. The fluorescence from the atom cloud coupled into the ONF is detected on an SPCM (Excelitas Technologies, SPCM-AQRH-14-FC) at either end of the ONF assembly using dichroic mirrors (DMLP900), which reflect 795 nm light and transmit at 993 nm. Narrowband filters (Alluxa-795) at 795 nm are used with SPCM1 to suppress any background light. At the other end, the 780 nm is detected with SPCM2 in conjugation with a 780 nm filter (Thorlabs FB780-10). The transmission of the coupled 993 nm light through the ONF assembly is 30%, since the nanofibre is prepared with its parameters optimised for 780 nm. Approximately $300 \mu\text{W}$ (measured at the output) of 993 nm light is sent through the ONF, from both sides (*i.e.*, $600 \mu\text{W}$ in total), for a few hours prior to the experiment so as to heat the ONF to avoid deposition of atoms on its surface.

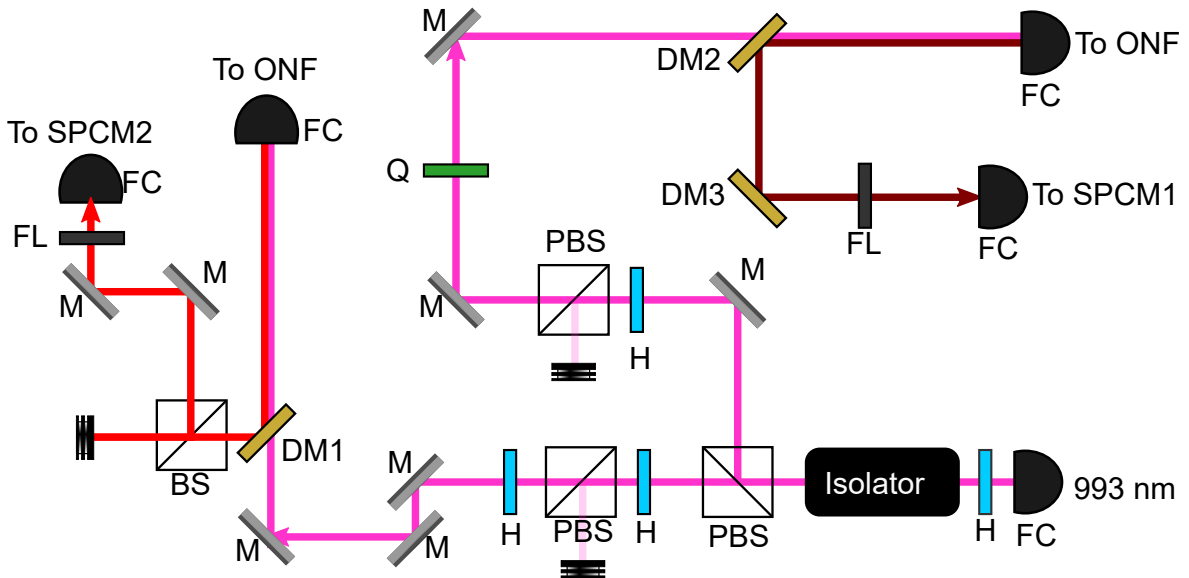


Figure 5.4: Schematic of the setup. M: Mirror. PBS: Polarising beam splitter. DM: Dichroic mirror. BS: Beam splitter. FL: Optical filter. H: Half-wave plate. Q: Quarter-wave plate. SPCM: Single-photon counting module. FC: Fibre coupler. The different coloured arrows indicate different wavelengths of light, 993 nm: pink, 780 nm: red and 795 nm: brown respectively.

5.3 Single-Frequency, Two-Photon Spectroscopy in a MOT-ONF system 71

In a typical experimental sequence, the atom cloud is loaded to saturation and then the 993 nm light coupled into the ONF is scanned ± 40 MHz across the $5S_{1/2}F = 2 \rightarrow 6S_{1/2}F' = 2$ transition. The 993 nm light interacts with the atoms at the nanofibre waist and initiates the two-photon excitation. The 795 nm and 780 nm fluorescence emitted by the atoms during decay to the ground state are coupled to the guided modes of the ONF. We detect the 780 nm and 795 nm separately and the resultant fluorescence signals collected by SPCM1 (795 nm) and SPCM2 (780 nm) are given in Fig. 5.5. The given data is the average of 40 experimental cycles. The 795 nm peak appears close to the frequency detuning of the peak of the vapour cell reference. We can observe a dip at the same detuning in the collected 780 nm fluorescence; this could be due to the transfer of atoms from the MOT cycle to the two-photon transition. The $6S_{1/2} \rightarrow 5P_{1/2}$ decay channel has a higher probability to occur than the $6S_{1/2} \rightarrow 5P_{3/2}$ channel, resulting in a higher signal. Due to the above reasons, we focus our discussion on the results for 795 nm fluorescence.

Focussing on the 795 nm fluorescence observed, the linewidth of the spectrum is larger than that for the vapour cell reference. The presence of the MOT beams during the experiment may contribute to the broadening due to power broadening and the AC Stark effect [149]. We observe asymmetry in the 795 nm signal which could be due to the van der Waals [36, 192]. The shift of the resonance in the MOT-ONF system can be accounted by the light-shifts induced by the intense field of the 993 nm beams at the nanofibre [119, 157].

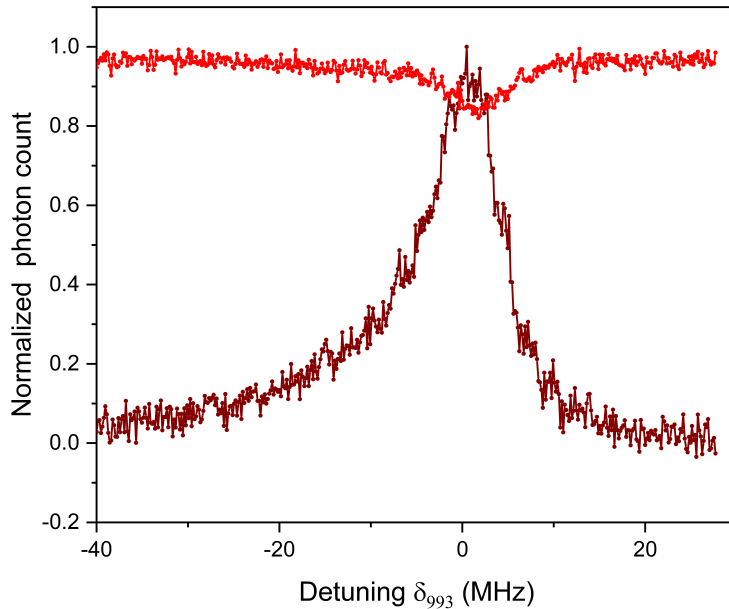


Figure 5.5: Evidence of ONF-mediated, two-photon excitation in cold atoms. The 993 nm laser is scanned in frequency and launched into the ONF with $600 \mu\text{W}$ of power detected at the output of the pigtails. Normalised 795 nm (brown) and 780 nm (red) fluorescence output detected at SPCM1 and SPCM2 respectively.

Once the signature of two-photon absorption was observed, the influence of the 993 nm beam power on the TPA strength in the system was investigated. For this study, we started with no 993 nm power and no 795 nm signal was observed. Then, step-by-step, we increased the 993 nm power; at $50 \mu\text{W}$ per beam we started to observe the 795 nm peak close to resonance. Up to $800 \mu\text{W}$ per beam, we can see the signal broadens with power (refer to Fig. 5.6(left)). With microWatts of 993 nm powers we could obtain saturation of the TPA in the MOT-ONF system (refer to Fig. 5.6(left)).

Further increasing the 993 nm power to 1 mW per beam, we see a shoulder appearing in the blue detuning of the signal (see to Fig. 5.6(right)). Two distinct peaks are observed in the 795 nm spectra, with increasing power. The frequency separation between the peaks increases linearly with the 993 nm power (see Fig. 5.7). The physics behind splitting of the peak or the possible presence of an extra peak in the spectrum is still under consideration. Initially, the reason for the splitting was attributed to Autler-Townes splitting of the $6S_{1/2}$ level. In Autler-Townes splitting, the level splitting is proportional to the square root of the light beam. In our experiment we observe a linear dependence on the 993 nm power. We are working with theoreticians to develop a model of the system to help us determine the reason for the observed splitting. To date, no explanation has been found.

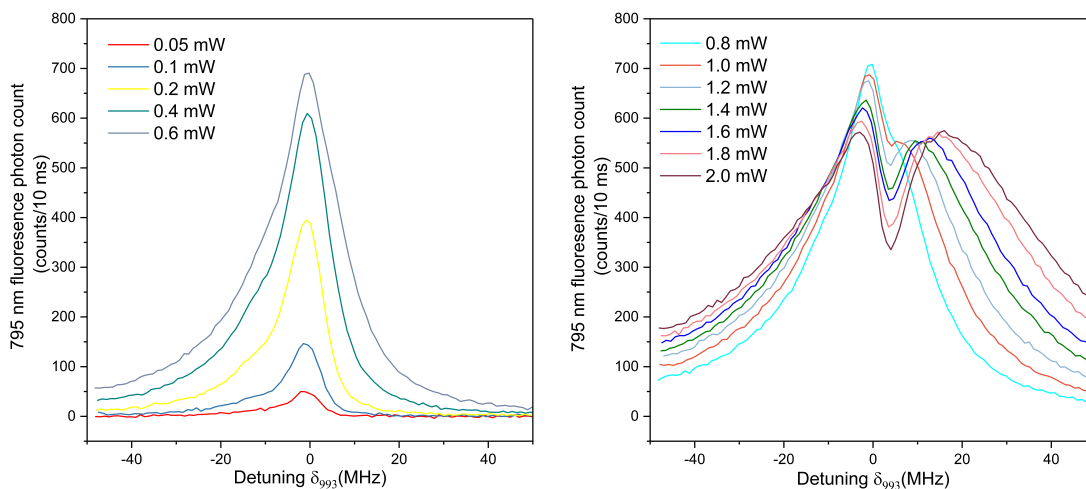


Figure 5.6: The 795 nm fluorescence obtained in the SPCM1 with increasing 993 nm power (left) as a function of 993 nm detuning. Increase in splitting of the 795 nm fluorescence spectra as the power per 993 nm beam is increased, as a function of 993 nm detuning (right).

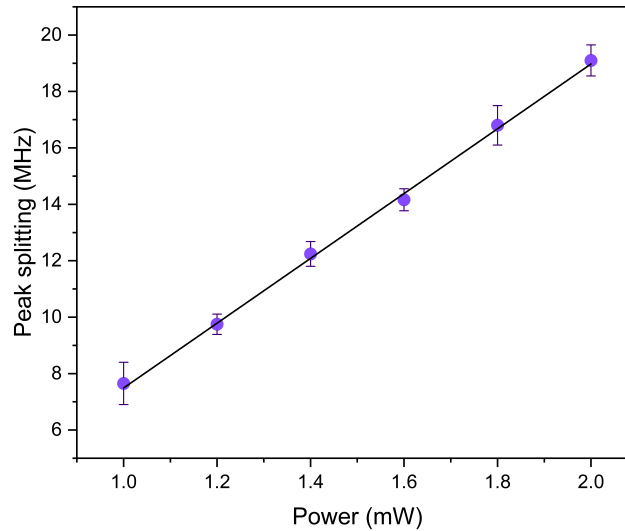


Figure 5.7: Linear dependence of the separation between the split peaks in Fig. 5.6(right) on the power of the 993 nm. The line represents a linear fit.

5.4 Polarisation Control by Imaging for an ONF Installed in a Vacuum Chamber ²

In the ONF-atom system, since the polarisation of the light at the waist of the nanofibre is crucial, we adapted the polarisation control technique for light in optical nanofibres [193] developed in our group to the case of a nanofibre installed in the vacuum chamber. In typical atom experiments mediated by an ONF, the polarisation is studied using a Rayleigh scattering method or simply by adjusting the input polarisation so that the light atom interaction is ideal. Tkachenko *et al.* [193] developed a technique for polarisation control that relies on imaging the scattered light from the fibre surface using a camera and a single lens to detect its polarisation. The guided light in an ONF has a significant electric field component along the direction of propagation which makes the scattering images of horizontally and vertically polarised light similar. They used a polariser oriented perpendicular to the direction of the propagation, therefore the imaging system consisted of a polariser, a filter and a convex lens which collects the scattered light. To implement the same technique in our experiment, we used a combination of two lenses L1 ($f=125$ mm) and L2 ($f=75$ mm) to image the scattered light from the nanofibre on a camera (ANDOR Technology, Luca^{EM}R, DL-604M-OEM) (see Fig. 5.8(a)). The errors in the state identification are expected to be less than 10° on the Poincaré sphere [121].

²This section is based on "Spin selection in single-frequency two-photon excitation of alkali-metal atoms", K.S. Rajasree, R.K. Gupta, V. Gokhroo, F. Le Kien, T. Nieddu, T. Ray, S. Nic Chormaic and G. Tkachenko, *Phys. Rev. Research* **2**, 033341 (2020) [4]. K.P. Subramonian Rajasree has contributed to all aspects of the cold atom experiment and paper writing.

Tkachenko *et al.* [193], relied on a blurred image taken at the plane y' (see Fig. 5.8(b)), where a difference of brightness sums when $x' < 0$ (Σ_1) and $x' > 0$ (Σ_2) is clearly visible. To quantify this brightness difference, two quantities are defined, $\Sigma = \Sigma_1 + \Sigma_2$ and $\Delta = \Sigma_1 - \Sigma_2$. The quantity Σ has a maximum value when the light is horizontally polarised and minimum when light is vertically polarised and Δ has maximum when the light is diagonally linear polarised and minimum when the light is antidiagonal. Let the polarisation state of the light at the input be $S_{\text{in}} = (1, S_1, S_2, S_3)$, where $S_{1,2,3}$ are the Stokes parameters. The polarisation state of light at the nanofibre waist can be written as

$$S_w = M_- S_{\text{in}}, \quad (5.2)$$

where M_- is the Mueller matrix of the down taper, which transforms the Stokes vector, S_{in} , to S_w . The down taper adiabaticity and ferrules, plus splicing can influence this transformation matrix. Polarisation compensation is performed such that $S_w = S_{\text{in}}$. The polarisation compensation optics were introduced at the input of the ONF and consist of a pair of QWP and a variable retarder (VR, liquid crystal type, Thorlabs, LCC1111-C). The influence of the compensation optics can be added to Eqn. 5.2 and it can be modified as $S_w = M_- M_{\text{PC}} S_{\text{in}}$. The polarisation compensation is achieved in two steps. First, the input polarisation of 993 nm is initially made to be horizontally polarised and the quarter-wave plate is independently rotated to maximise the total scattering Σ . This ensures that the light at the nanofibre waist is horizontally polarised, thus mapping the input light polarisation. In the next step, the polarisation at the input is made to be diagonally polarised; then the VR is rotated to maximise the scattering difference, Δ . This confirms that the light is diagonally polarised at the waist. These steps ensure the compensation optics will transform, for any polarisation of input light, $S_{\text{in}} \rightarrow S_w$.

5.4.1 Verification of the Polarisation Control with Spin-Selection Rule

To verify the polarisation compensation, we propose to study the polarisation dependence of the single-frequency, two-photon transition $5S_{1/2} \rightarrow 6S_{1/2}$. Recalling, the total electronic angular momentum quantum numbers of this transition are $\Delta J = 0$ and we have the selection rules $\Delta F = 0$ and $\Delta m_F = 0$ [129], meaning that the total spin of the atom must be preserved. If we assume that the spin of light is well-defined, conservation of angular momentum in the excitation process requires that the two photons must have mutually cancelling spin projections along the quantisation axis. This principle has already been verified experimentally using sodium [194, 195] and rubidium [1, 196] vapour illuminated by counter-propagating Gaussian beams. Doppler-free transition peaks were observed when the beams had equal linear polarisations or opposite circular polarisations in the laboratory frame, but the peaks disappeared for circular polarisations of the same handedness. When the excitation light is elliptically polarised, two-photon transitions are not completely absent, but occur at a rate that depends on the shape of the polarisation ellipse, as demonstrated experimentally [196]. It is important to note that the aforementioned spectroscopy experiments are vapour

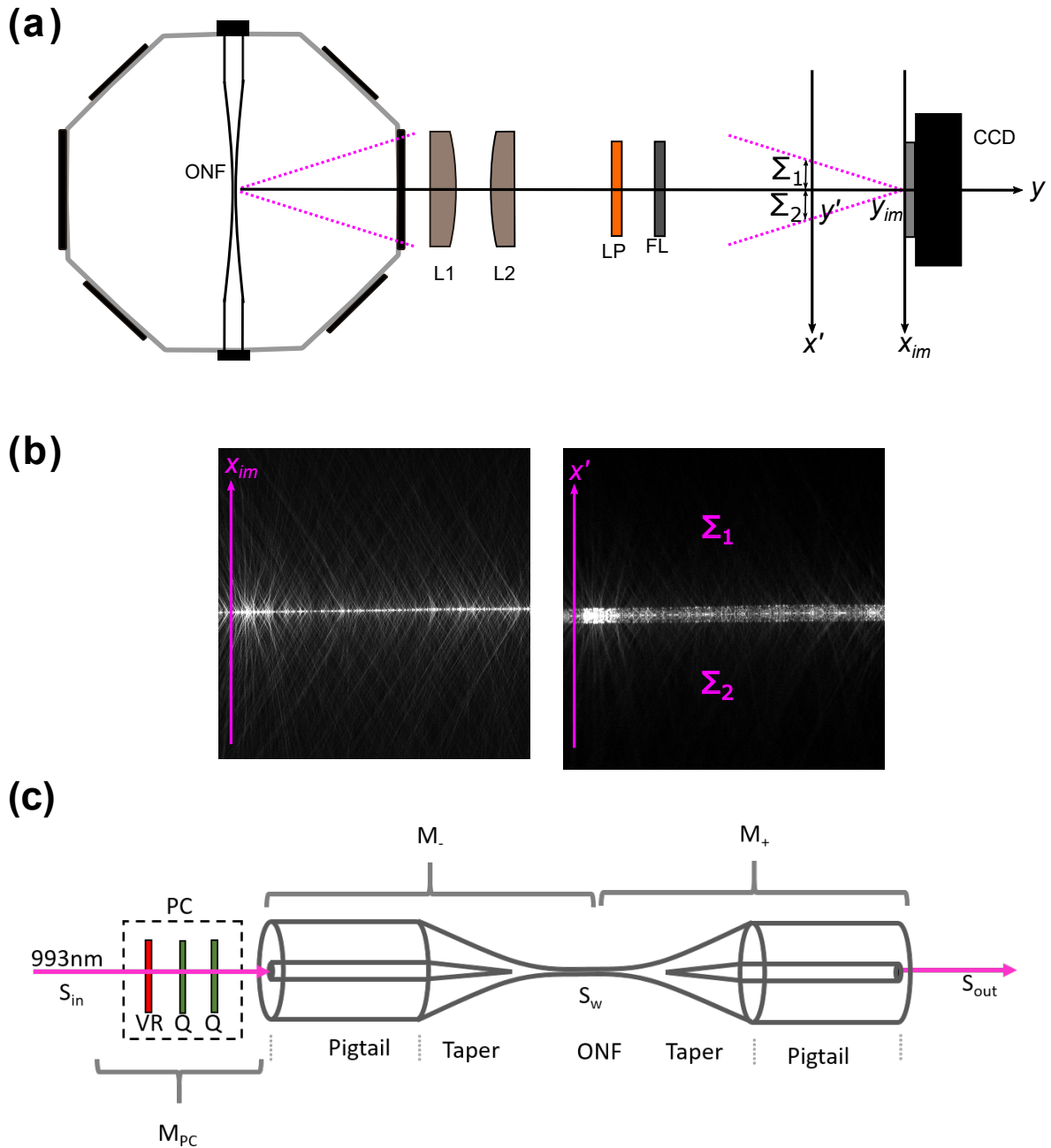


Figure 5.8: (a) Imaging system used for polarisation identification. LP: Linear polariser. FL: Filter. CCD: Charged couple device. L1,L2: Convex lenses. (b) Sharp and blurred image of the ONF at y_{im} and y' respectively. Σ_1 and Σ_2 cannot be distinguished in the sharp image and, hence, the blurred image is used for polarisation identification. (c) The polarisation of the input light (S_{in}) transforms to a different polarisation defined by S_w . The polarisation compensator (PC) setup is used to restore the polarisation of the light at the waist so it matches that at the input.

cell based experiments. In our system, cold neutral atoms are coupled to the evanescent field of an ONF, and the polarisation dependency of such a two-photon transition have not been studied before.

A theoretical model to describe the spin selection for two-photon transitions as a function of the polarisation of the excitation light to go beyond the limiting cases of purely linear or purely circular polarisation. As a verification tool, we experimentally studied the polarisation dependency of an S \rightarrow S two-photon transition in a ^{87}Rb gas for two conceptually different excitation conditions: (i) warm atoms in a vapour cell with Gaussian beam illumination and (ii) laser-cooled atoms in the evanescent field of a single-mode ONF, where the light is strongly nonparaxial. In [4], we have presented the vapour cell measurements for the polarisation dependency of the two-photon absorption.

Theory

The excitation field in terms of the helicity parameter (σ) is given by [193, 197]:

$$\mathcal{E} = \frac{1}{\sqrt{2}} \left(\sqrt{1 + \sigma} \mathcal{E}_{+1} + \sqrt{1 - \sigma} \mathcal{E}_{-1} \right), \quad (5.3)$$

where $-1 \leq \sigma \leq 1$, $\mathcal{E}_p = (e_r \hat{r} + p e_\varphi \hat{\varphi} + e_z \hat{z}) e^{i(p\varphi + \beta z)}$, $p = \pm 1$ is the polarisation index for quasi-circularly polarised fundamental guided modes [198], β is the propagation constant, and e_r , e_φ , e_z are the reduced cylindrical components of the mode function and they are independent of φ and the z direction [199–201]. Note that, if the field is retro-reflected, one must change the sign for β , σ , and p . After statistical averaging of ξ over the atomic position, we find the two-photon transition rate defined by 2.11 can be written as,

$$P_{13} \propto \bar{\xi} = A - \sigma^2 B, \quad (5.4)$$

where

$$\begin{aligned} A &= \langle (|e_r|^2 + |e_\varphi|^2 - |e_z|^2)^2 \rangle_r \\ &\quad + 0.5 \langle (|e_r|^2 - |e_\varphi|^2 - |e_z|^2)^2 \rangle_r, \\ B &= \langle (|e_r|^2 + |e_\varphi|^2 - |e_z|^2)^2 \rangle_r \\ &\quad - 0.5 \langle (|e_r|^2 - |e_\varphi|^2 - |e_z|^2)^2 \rangle_r, \end{aligned} \quad (5.5)$$

and $\langle \dots \rangle_r$ stands for statistical averaging over the radial distance r from the nanofibre. The quadratic Eqn. 5.4 predicts that the transition rate is maximum for linearly polarised ($\sigma = 0$) and minimum (but, in general, *nonzero*) for circularly polarised ($\sigma = \pm 1$) excitation. Thence, we theoretically predict that the two-photon strength depends on the square of the intensity of the exciting beam and the square of the helicity. We test the proposed theory in our nanofibre-cold atom system.

Experiment

The experimental setup is given in Fig. 5.9. The experiment sequence is as described in Section 5.3. Initially, the 993 nm light is sent through the fibre for 2 hours

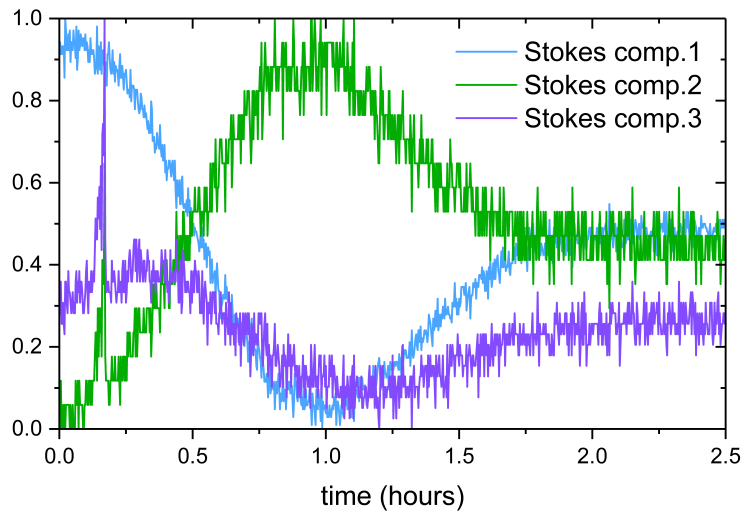


Figure 5.10: The variation of the normalised Stokes' parameters during the heating stage.

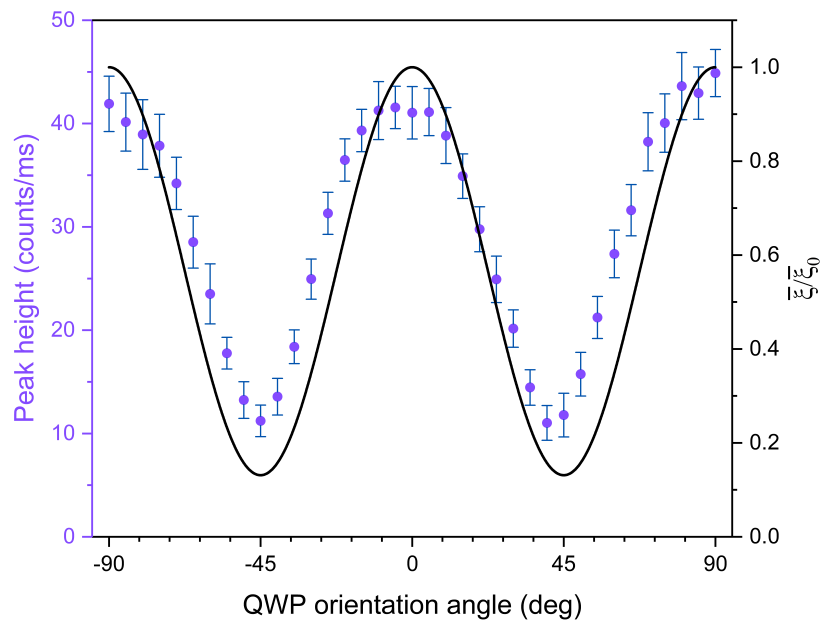


Figure 5.11: Polarisation dependence of the 795 nm fluorescence. Here, when Q_C is set so that $\theta = 0^\circ$, $\sigma = 0$, the light is linearly polarised and circularly polarised when $\theta = 45^\circ$, $\sigma = 1$. The solid line represents the theoretical prediction.

The lateral shift of the rising slopes seen in both periods of the θ dependence in Fig. 5.11 is likely to be an experimental artefact such as imperfection of the waveplate,

enhanced by coupling of light into the fibre. Other effects not taken into account are possible polarisation-dependent saturation [202] of the transition in the atomic cloud, a polarisation-induced inhomogeneity in the intensity profile [199] and the related change in the local atomic density due to the dipole force, and position-dependent Stark shifts in the atomic energy levels [149]. We also note that the relation $\sigma = \sin(2\theta)$ may not be exactly fulfilled for ONF-mediated excitation. For instance, the generation of orbital angular momentum in the evanescent field which is more significant for quasi-circular polarisation [31, 193], effectively changes the helicity and its relation to the polarisation of light sent into the fibre. This invites further studies on two-photon processes under nonparaxial fields, inclusive of the orbital degree-of-freedom.

5.5 Conclusions

Two-photon transition in a hot Rb vapour and cold atom system. The effects of excitation laser power and beam polarisation on the observed spectroscopy signals were investigated. The observations at higher 993 nm power are still being studied. We have observed the spin selection rule as applied to an $S \rightarrow S$ two-photon atomic transition in an MOT-ONF system. Owing to the accurate polarisation control at the nanofibre waist, we were able to study the transition rate as a function of helicity of the excitation. The two-photon transition in the evanescent field could not be extinguished by simply varying the polarisation of the coupled light; we observed a minimum rate of 25%. These findings are expected to have impact in atom-based hybrid quantum technologies where full control on quantum state selection is vital and could open new ways of selecting transition pathways for frequency references and atomic clocks, transfer of spin or orbital angular momentum between light and atoms [203, 204], chiral nanophotonics [205], and for fundamental precision tests in parity non-conservation [206, 207]. Apart from these applications, polarisation-control in the ONF is a significant step in realising the nanofibre trap for the ground state atoms or for studying Rydberg transitions which are polarisation dependent.

Chapter 6

Stimulated Four-Wave Mixing in a MOT-ONF System

The strong interactions between Rydberg atoms make them an interesting platform, for example, to realise single photon sources [74, 208, 209], single-photon transistors [210, 211], and strongly correlated photon pairs using a four-wave mixing (FWM) scheme. In our system we are motivated to explore the two-photon resonant FWM solely by exploiting the directional nature of the generated FWM light. In [118], Stroum *et al.* theoretically studied the scenario where Rb Rydberg atoms are prepared in a specific state next to the ONF. They showed that only a small percentage of spontaneous emitted light from the Rydberg level is coupled to the ONF if one limits the discussion to fundamental guided modes. If the Rydberg atoms are prepared with a two-photon excitation scheme with two-step decay to the ground state, using an additional seed light, which is resonant with one of the decay channels, could stimulate the FWM process. This would benefit the detection of the Rydberg states mediated with the ONF. Stimulated FWM has not yet been explored in the MOT-ONF system. To eliminate the complications arising from the Rydberg states, in this chapter we explore the FWM process based on the $5S_{1/2} \rightarrow 6S_{1/2}$ two-photon excitation scheme presented in the Chapter 5. Before discussing the experiments and observations, we briefly introduce the concepts of four-wave mixing and stimulated four-wave mixing.

6.1 Four-Wave Mixing

Four-wave mixing is a nonlinear optical phenomenon arising from the third order optical susceptibility. In the process of spontaneous FWM, four electromagnetic fields interact in a medium, when the matching conditions for wave vectors and frequencies are valid. To explain the phase matching conditions, let us consider a four-wave mixing process. The intensity of the fourth field generated from the interaction of three electromagnetic fields can be written as [212]

$$I(\omega_4) \propto |\chi^3(-\omega_4, \omega_1, \omega_2, \omega_3)|^2 G, \quad (6.1)$$

here $\omega_1, \omega_2, \omega_3$ are the input frequencies, ω_4 is the generated field and χ^3 is the nonlinear susceptibility. The factor, G , is the phase matching factor which is given by

$$G(\alpha_i L_{\text{eff}}) = \frac{1 + \exp(-\Delta\alpha_i L_{\text{eff}}) - 2 \exp(-\frac{1}{2}\alpha_i L_{\text{eff}}) \cos(\Delta k L_{\text{eff}})}{(L_{\text{eff}}^2/4) (\Delta k^2 + (\Delta\alpha_i^2/4))}. \quad (6.2)$$

The phase matching factor is dependent on the α_i , which are frequency dependent absorption coefficients, L_{eff} is the effective length where the four fields overlap and $\Delta k = k_4 - k_1 - k_2 + k_3$, is the wave vector mismatch. When there is no absorption of the fields, Eqn. 6.2 reduces to $\text{sinc}^2(\Delta k L_{\text{eff}}/2)$. The value of G is maximum when $\Delta k L_{\text{eff}}$ is zero, *i.e.*, either zero overlap length or no wave vector mismatch [212]. The process of the maintaining a small wave vector mismatch is known as the *phase matching condition*. The highly directional nature of the signals produced by FWM is a consequence of this phase matching condition. Since energy and momentum are conserved in this process, the generated photons are correlated. Hence, it is a promising method in quantum information science and quantum meteorology for practical purposes. The FWM process has found its way into applications like parametric amplification [213], phase conjugation [214, 215], real-time holographic imaging [216, 217], spatial filtering [218], etc. Focussing on the FWM in atomic systems, the Λ , double- Λ and the ladder type systems have been exploited to produce a photon pair [219–223], optical memory [224, 225], and squeezed states [226, 227] via spontaneous FWM.

If we send low power light, in addition to the strong exciting light, into the medium, different types of FWM are observed. One such example is stimulated four-wave mixing (StFWM) [228–230], which we explored in the experiment discussed in this chapter. We relied on the same ladder-type, two-photon excitation between $5S_{1/2}$ and $6S_{1/2}$ as discussed in Chapter 5. In this experiment, the $5P_{1/2}$ level is populated from $5S_{1/2}$ via two routes, *i.e.*, indirectly through 993 nm light and directly with 795 nm light (refer to Fig. 6.1). We addressed the $5S_{1/2} \rightarrow 6S_{1/2}$ transition using 993 nm light. From $6S_{1/2}$, the atoms can decay back to $5S_{1/2}$ either via $5P_{1/2}$, emitting 1324 nm and 795 nm or $5P_{3/2}$, emitting 1367 nm and 780 nm. The seed laser at 795 nm directly addressed the $5S_{1/2} \rightarrow 5P_{1/2}$ transition.

6.2 Experimental Details

As previously discussed in Chapter 5, the 993 nm light is derived from a CW Ti-saph laser and sent through the ONF as in the experimental schematic given in Fig. 6.2. The 795 nm seed light is derived from an ECDL (Toptica, DL100 pro) and the frequency is locked to the $5S_{1/2}$ ($F = 2$) \leftrightarrow $5P_{1/2}$ ($F' = 2$) transition using saturated absorption spectroscopy (CoSy, Toptica). The 795 nm light is fed to two double-pass AOM (ATM-602DA2B, IntraAction Corp, central frequency: 60 MHz) configurations, where in one double-pass AOM configuration the +1 order is selected and in the other the -1 order is selected, thereby cancelling the frequency shift. The frequency modulation input of one of the AOMs is adjusted to compensate the AC Stark shift from the 993 nm light. The 795 nm output from the AOM assembly is overlapped with 993 nm and fed to the ONF. An atom cloud with a typical average density of 10^{10} atoms per cm^3 is formed. The MOT-ONF system is explained in Chapter 3. The temperature of the

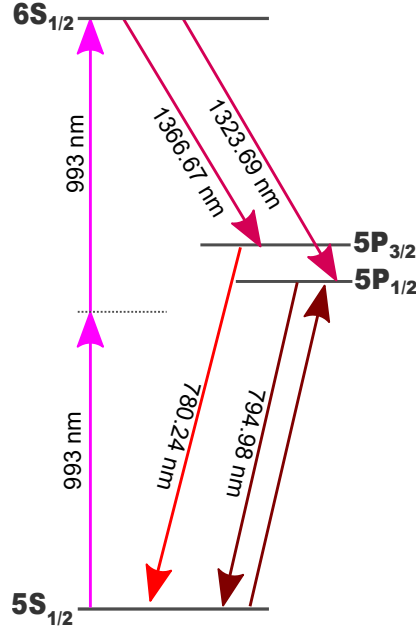


Figure 6.1: The energy level diagram relevant to the stimulated four-wave mixing process. The 794.98 nm beam is a weak seed laser.

ONF-embedded atom cloud is $\sim 150 \mu\text{K}$. The prepared ONF supports the fundamental mode for both 993 nm and 795 nm light. The transmission of the 993 nm light through the system is 30%. The transmission for 795 nm light is 60%.

As in earlier experiments, the 993 nm light is sent through the ONF prior to taking measurements to heat the ONF. A typical experimental sequence is that the MOT is loaded to saturation and then the 993 nm laser is scanned 50 MHz around the centre frequency in 1 second, whereas the frequency of the 795 nm laser is locked. The 795 nm light emitted by the atoms is coupled back into the ONF and is at both ends of the ONF using single-photon counting modules, SPCM1 (forward) and SPCM2 (backward) through narrowband filters (Alluxa 794.9-1 OD4) and dichroic mirrors (DM1, DM2, DM3: DMLP950).

For given powers of 795 nm and 993 nm, the 795 nm output is collected in the presence and in absence of the seed laser (see Fig. 6.3), as 993 nm light is scanned across resonance. Without the seed laser, the 795 nm fluorescence coupled in both directions is approximately the same at about 400-600 photon counts/10 ms. With the 795 nm seed laser at 70 pW, we see a stimulated FWM signal under the condition of two-photon resonance. We observe enhancement of the 795 nm photon emission in the forward direction (3000 photon counts/10 ms) and suppression in the backward direction (300 counts/10 ms). Owing to the directional nature of the output we observe, we explore the possibility of FWM light generation from the atoms excited by two-photon coherence using the seed laser.

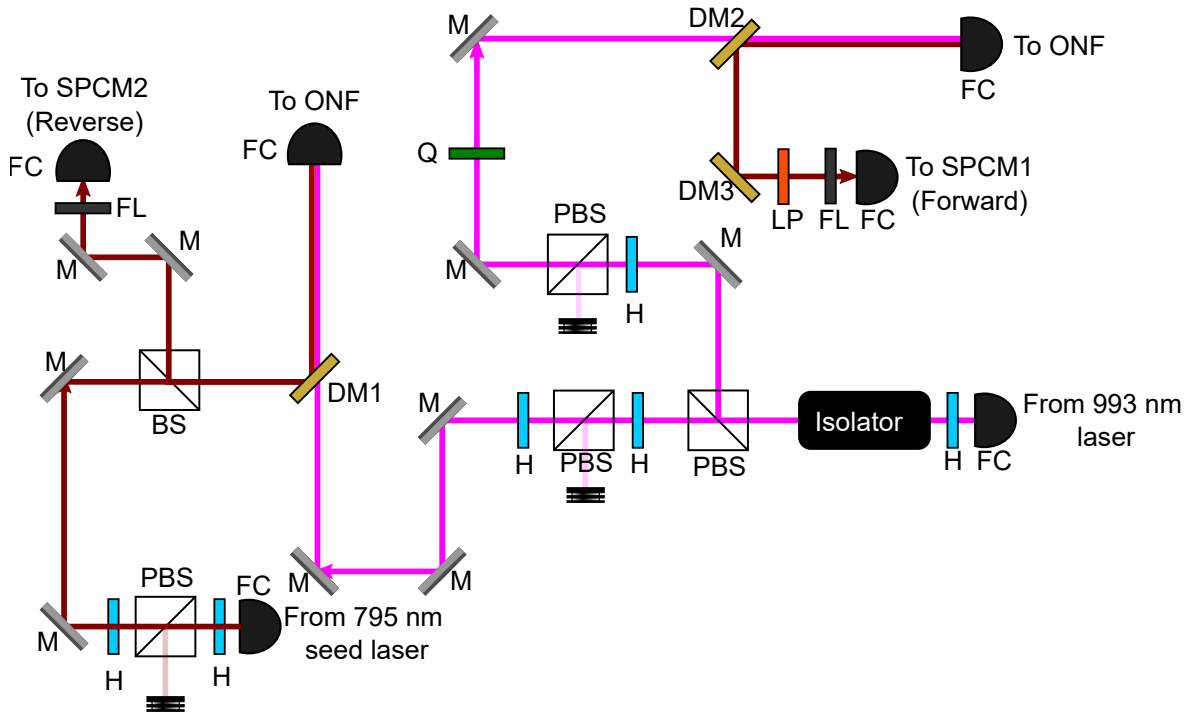


Figure 6.2: Simplified experimental schematic. M: Mirror. PBS: Polarising beam splitter. DM: Dichroic mirror. BS: Beam splitter. FL: Optical filter. DM1-DM3: Dichroic mirror. H: Half-wave plate. Q: Quarter-wave plate. SPCM: Single-photon counting module. LP: Linear polariser. FC: Fibre coupler. The different coloured arrows indicate different wavelengths of light, 993 nm: pink and 795 nm: brown respectively.

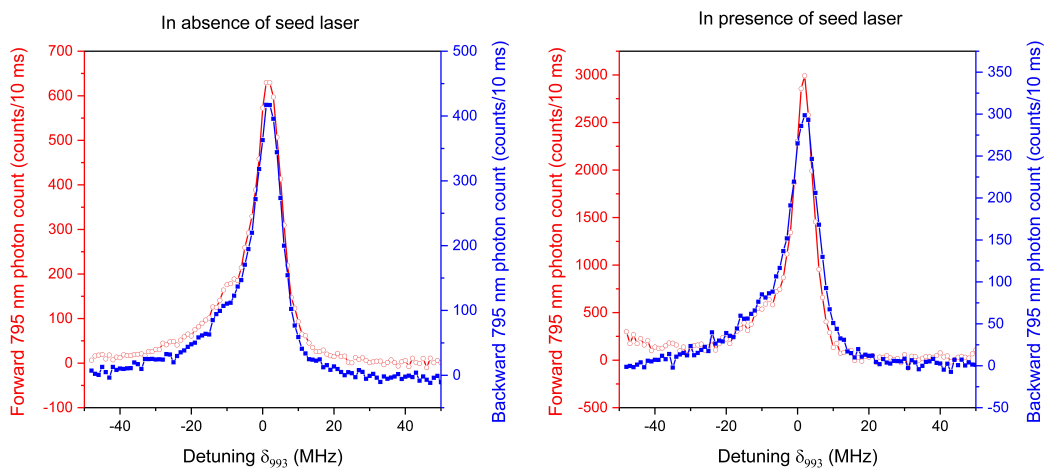


Figure 6.3: 795 nm photon count coupled into the ONF in the absence of the seed laser (left). 795 nm photon count coupled into the ONF in the presence of the seed laser (right). Blue curve represents the 795 nm spectrum obtained in the backward direction with respect to seed laser propagation and red curve represents the 795 nm spectrum in the forward direction.

6.3 Results and Discussion

The generated and the detected 795 nm light is a result of atoms decaying back to $5S_{1/2}$ from $5P_{1/2}$ (see Fig. 6.1). The atoms are pumped to the $5P_{1/2}$ level by (i) the two-photon process initiated by 993 nm and (ii) direct excitation by the 795 nm seed laser. In the following series of experiments we study the dependence of the generated FWM light coupled to the ONF on both the 993 nm and the 795 nm light properties. FWM generation is dependent on the laser intensities due to the nonlinear phenomenon in the atomic medium.

Varying Seed Laser Power at a Fixed 993 nm Laser Power

To elucidate the influence of the seed laser, its power was varied starting from 0 pW to 60 pW, while the 993 nm laser power was maintained at $800 \mu\text{W}$. The transmitted seed laser and 993 nm power were measured at the output of the ONF-patch cable assembly. From Fig. 6.4, we can observe that the forward photon count increases and the reverse photon count reduces when the seed laser power is varied from 0 to 30 pW.

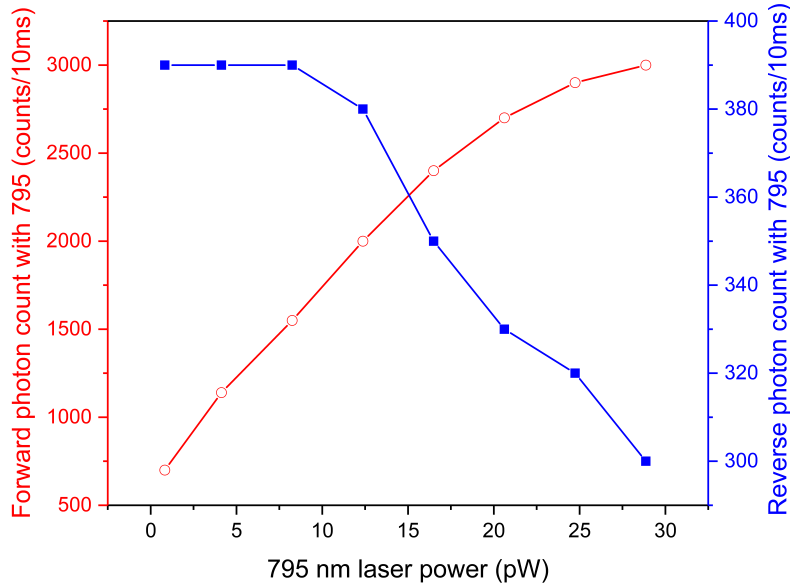


Figure 6.4: The maximum forward photon count (red) and reverse 795 nm photon count (blue) as a function of increasing seed laser (795 nm) power (measured at output) for a fixed 993 nm power of $800 \mu\text{W}$.

Figure 6.5 shows the 795 nm spectra obtained at SPCM1 and SPCM2. Note that the forward count increases by a factor of 6 whereas the reverse reduces by about 0.25 times only. When the seed laser power is increased beyond 30 pW, the forward signal starts to reduce with increasing seed laser power. The signal obtained on SPCM2, *i.e.*, 795 nm light coupled in the reverse direction, starts to broaden and eventually a dip appears in the spectrum (see Fig. 6.6). Possible reasons for the dip could be a multiphoton

process initiated when the seed laser is strong enough. Similar observations have been demonstrated by Park and Moon [228].

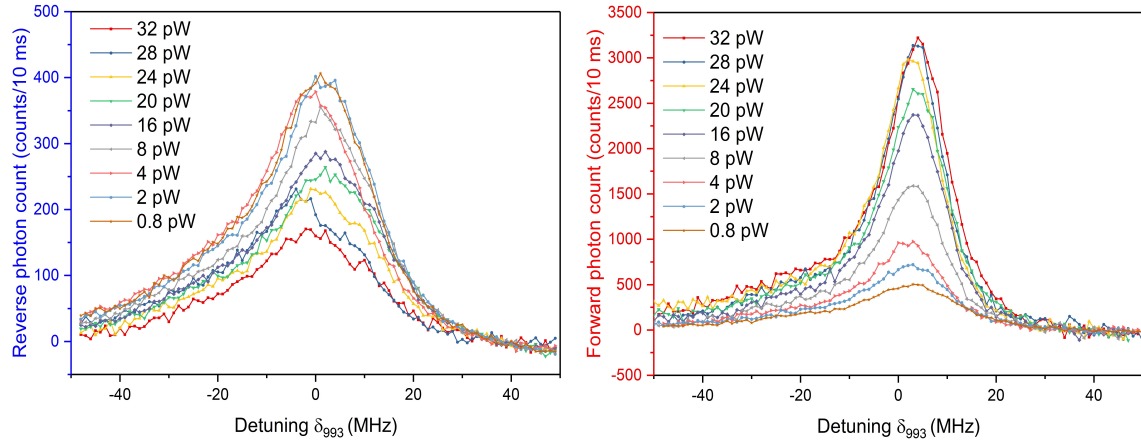


Figure 6.5: (Left) The reverse (SPCM2) and (right) forward (SPCM1) 795 nm spectra for seed laser power ranging from 0.8 to 32 pW. Note that the seed laser power is measured at the fibre output end.

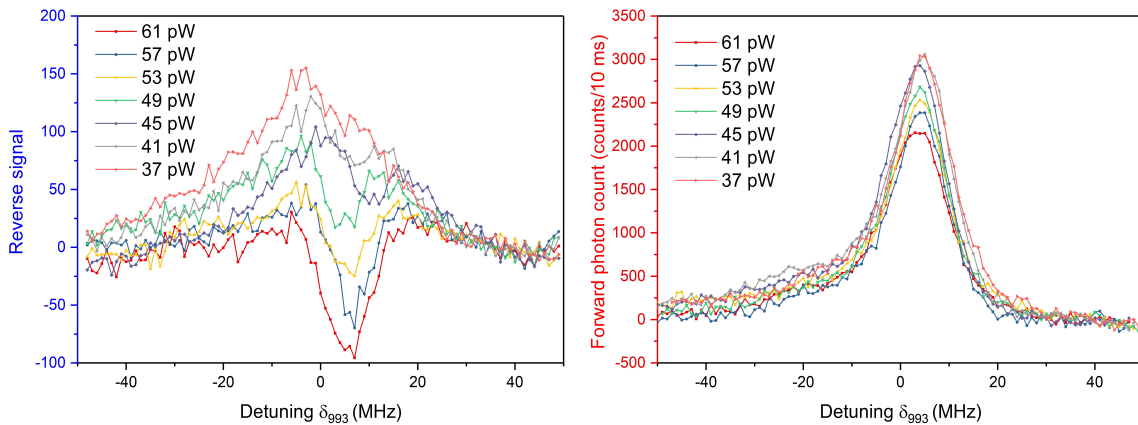


Figure 6.6: (Left) The reverse (SPCM2) and (right) forward (SPCM1) 795 nm spectra for seed laser power ranging from 37 to 61 pW. Note that the seed laser power is measured at the fibre output end.

Varying 993 nm Laser Power for a Fixed Seed Laser Power

The next experiment was to demonstrate the role of the 993 nm laser power in generating the FWM light. In this set of experiments, the seed laser was maintained at 12 pW, while the power of 993 nm was varied. Figure 6.7 shows the maximum 795 nm photon count obtained in the forward and reverse directions with varying 993 nm power from 600 μ W to 1.2 mW. Here, with the increase of the 993 nm power, we can see that the number of photons coupled in both directions increases in the presence

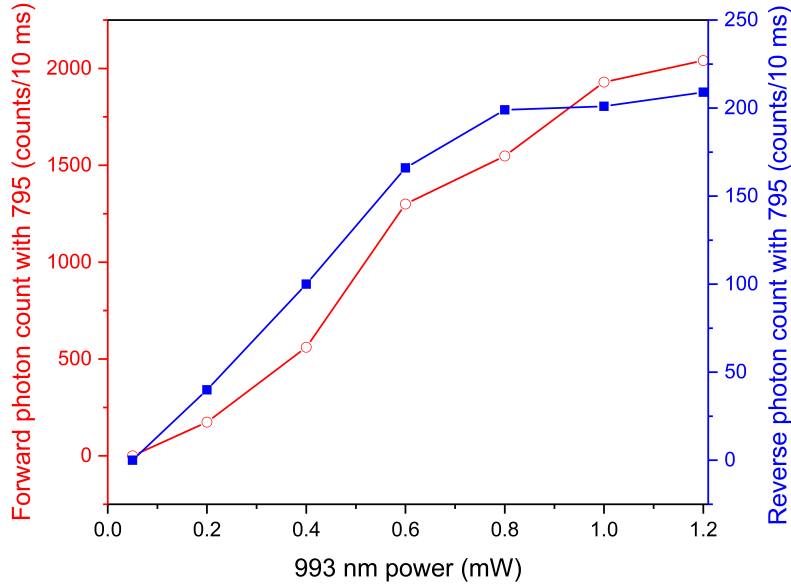


Figure 6.7: The maximum forward photon count (red) and reverse photon count (blue) as a function of increasing 993 power. The 795 nm seed laser is kept at 12 pW, as measured at the fibre output end.

of the weak seed laser. At 50 μW of 993 nm light, there is no 795 nm signal since the two-photon process is not initiated. With a further increase of the 993 nm power to 200 μW , we can see there is directional emission in the forward direction with the count rate being about a factor of 10 higher than the reverse. We can observe that the forward and backward count rate increases with the 993 nm power (see Fig. 6.8 for individual spectra). Once the 993 nm laser power is increased beyond 1.2 mW, as shown in Fig. 6.9, we observe splitting in the reverse coupled signal. This feature is discussed in Chapter 5. Once the splitting is observed, the forward-coupled photon count starts to reduce. The spectra for different 993 nm powers as a function of the 993 nm detuning is given in Fig. 6.9.

Polarisation Dependency

The next set of experiments was carried out to study the polarisation of the FWM generated light at 795 nm. We used a linear polariser (LPVISO50) at the output (see in Fig. 6.2). Here, we fix the power of 993 nm to 1 mW and the seed laser to 12 pW. The angle of the polariser (refer to Fig. 6.2) is varied. We measured the photon count in the forward direction for the FWM light stimulated by the seed light and the off-resonant seed light. From the obtained behaviour plotted in Fig. 6.10 we can see they follow the same trend. Thereby, we can conclude that the FWM light coupled from the atoms in the forward direction has the same polarisation as the input 795 nm light.

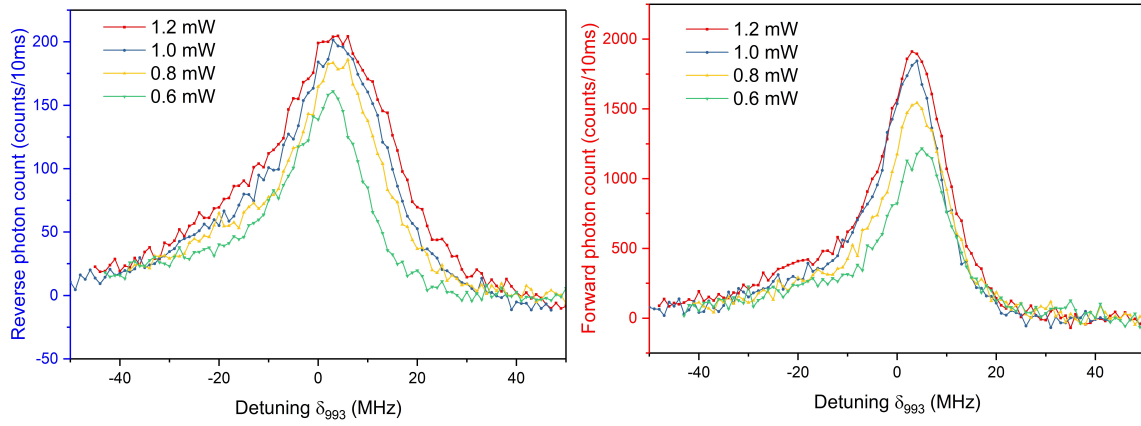


Figure 6.8: (Left) The reverse (SPCM2) and (right) forward (SPCM1) 795 nm spectra for 993 nm laser power ranging from 0.6 to 1.2 mW. Note that the 993 nm laser power is measured at the fibre output end.

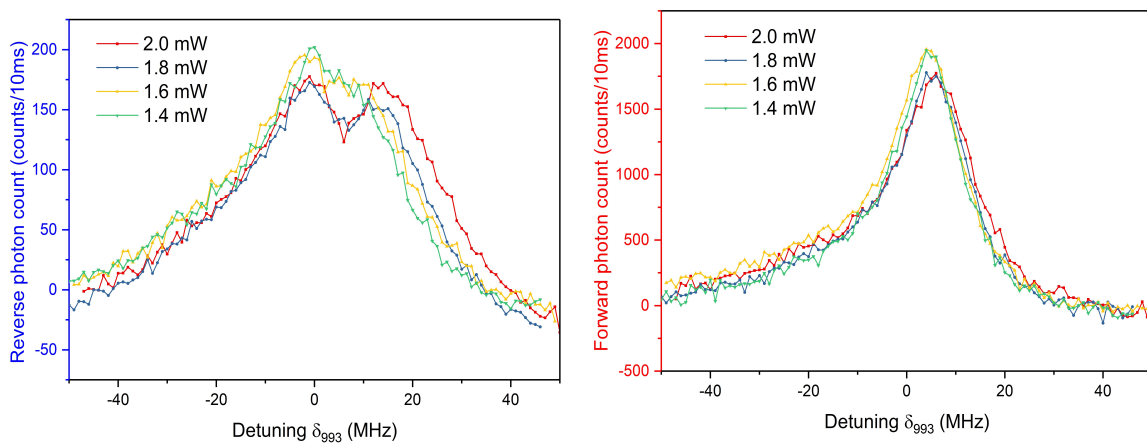


Figure 6.9: (Left) The reverse (SPCM2) and (right) forward (SPCM1) 795 nm spectra for 993 nm laser power ranging from 1.4 to 2.0 mW. Note that the 993 nm laser powers is measured at the fibre output end.

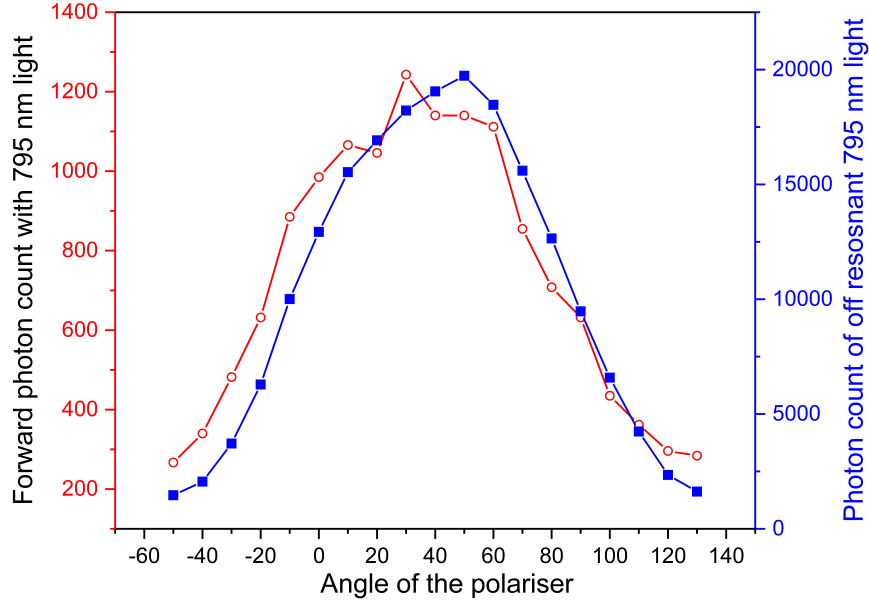


Figure 6.10: The variation of the polarisation of the generated FWM 795 nm light (red) and the seed 795 nm light (blue).

6.4 Conclusions

With the above experiments we can conclude the following. The ladder-type two-photon resonance condition should be satisfied to generate a FWM signal. The seed laser at 795 nm stimulates the FWM light from the ladder two-photon absorption initiated by 993 nm light. A weak seed light is preferred, since a stronger seed can induce a multiphoton process and disturb the two-photon coherence created using 993 nm [229]. The FWM generated light at 795 nm and coupled to the ONF is observed in the forward direction detector. The multiphoton process signatures are observed at the detector in the reverse direction.

To our knowledge, stimulated four-wave mixing mediated by an ONF is observed for the first time in this work. We have attempted to develop a theory to explain the observation, but the system defined using the four-level optical Bloch equations could not match the observations despite intense efforts by several theory groups at OIST and in UAB (Spain). Future theoretical efforts involve simplifying the model by reducing it to a two-level system and studying the directional coupling to the ONF. Focussing on the unanswered questions in the experimental observations, the appearance of the dip in the strong seed laser regime is one of the more interesting questions. Observation of the spectra with the seed laser detuned while the two-photon excitation laser is locked, may yield the answer.

Chapter 7

Conclusions and Outlook

The work presented in the thesis focussed on developing the experimental tools for studying Rydberg atom generation next to optical nanofibres. We have discussed the developments in creating Rydberg atoms with surfaces and how the ONF could be an interesting candidate for exploring sub-micron generation of highly excited atoms near dielectrics. A hybrid quantum system consisting of cold Rydberg atoms and an optical nanofibre interface was demonstrated. Using a two-photon, ladder-type excitation in ^{87}Rb , we demonstrated both coherent and incoherent Rydberg excitation at submicron distances from the nanofibre surface [2]. The population loss rate of the cold atom ensemble was used to measure the Rydberg population rate.

To study the influence of the nanofibre on the Rydberg atoms more precisely, we did a step-by-step approach to realise Rydberg EIT in the system. However, we failed to obtain meaningful observations when both the excitation beams were sent through the ONF. As the theoretical study indicates, the distance of the Rydberg atom from the ONF can influence the light coupling into the guided modes and there are significant chances that the Rydberg atom crashes into the ONF. Hence, ONF based trapping for the ground state could be used to deterministically fix the distance and an ONF trapping scheme based on the ponderomotive force [98] or magic wavelengths for Rydberg atoms could prevent the atom from sticking to the fibre. By appropriate combination of polarisation and intensity of the red- and blue-detuned light, the strength and the position of the atom trap can be fixed. Even though the trapping must be turned off during Rydberg excitation, the distance can be approximately fixed for fast processes.

For ONF-based traps, one of the important and non-trivial parameters of the nanofibre guided light is the polarisation. Hence, to gain access to the polarisation information of the nanofibre installed in a vacuum chamber, we implemented polarisation compensation based on imaging of the scattered light from the nanofibre [4]. To test the compensation we developed a theoretical framework for the probability of excitation in a single-frequency, two-photon excitation of alkali-metal atoms as a function of polarisation. We experimentally demonstrated a single-frequency, two-photon transition from the $5S_{1/2}$ ground state to the $6S_{1/2}$ excited state in vapour [1] and cold ^{87}Rb atoms using a continuous wave laser at 993 nm. We verified the theory by experimentally probing the $5S_{1/2} \rightarrow 6S_{1/2}$ transition rate. Thereby we gained deterministic control of the polarisation of the light in the nanofibre region. Experiments were later carried out by other group members to use the polarisation compensation for creat-

ing a nanofibre trap. It has been successfully demonstrated that compensation helps in controlling the polarisation of the nanofibre guided light and improving the trap efficiency. Typically, in a MOT-ONF system, 1-3 atoms contributes to signal, with improved nanofibre trap it was about 70 [231].

The splitting observations for the 993 nm spectroscopy in the nanofibre system at higher 993 nm powers are still being investigated. In the new experiment scheme, to rule out the influence of the cooling light in the two photon excitation, the cooling light is turned off *i.e.*, the two-photon excitation is being investigated in optical molasses. Future investigation of the enhanced nonlinear process by embedding an optical nanofibre will open up new possibilities for the generation of a fibre-integrated photon-pair source for quantum key distribution.

One technique that could be implemented to increase the fluorescence coupling to the ONF from a Rydberg atom would be to use an additional probe along with two-photon excitation lasers. Driving a stimulated four-wave mixing process could benefit in detecting and studying Rydberg atoms near to an ONF. StFWM was experimentally demonstrated in the MOT-ONF system for non-Rydberg atoms to simplify the initial tests. Aside from the endeavours to integrate the Rydberg atoms to the ONF, the work involving non-Rydberg levels is an attractive platform to generate correlated photon pairs [232]. The detection of 1324 nm light has been incorporated into the MOT-ONF system. The possibility to develop entangled photon pairs at wavelengths relevant to telecommunications and atomic transitions in the MOT-ONF system should be further investigated.

The works discussed in this dissertation make headway in the study of Rydberg atom-surface interactions at submicron distances. It has also contributed significantly to polarisation control in an ONF:atom system and towards exploiting the ONF:atom system for building quantum repeaters using cascaded atomic transitions involving non-Rydberg states. Thereby the work has answered several non-trivial questions that needed to be addressed in studying the excitation of a ground state neutral atom to a Rydberg state at a given distance from an optical nanofibre and the studies are substantial groundwork for any future endeavours.

Bibliography

- [1] T. Nieddu, T. Ray, K. S. Rajasree, R. Roy, and S. Nic Chormaic, *Opt. Express* **27**, 6528–6535 (2019).
- [2] K. S. Rajasree, T. Ray, K. Karlsson, J. L. Everett, and S. Nic Chormaic, *Phys. Rev. Research* **2**, 012038 (2020).
- [3] T. Ray, R. K. Gupta, V. Gokhroo, J. L. Everett, T. Nieddu, K. S. Rajasree, and S. Nic Chormaic, *New J. Phys.* **22**, 062001 (2020).
- [4] K. S. Rajasree, R. K. Gupta, V. Gokhroo, F. Le Kien, T. Nieddu, T. Ray, S. Nic Chormaic, and G. Tkachenko, *Phys. Rev. Research* **2**, 033341 (2020).
- [5] I. Bloch, *Nature* **453**, 1016–1022 (2008).
- [6] C. Weitenberg, S. Kuhr, K. Mølmer, and J. F. Sherson, *Phys. Rev. A* **84**, 032322 (2011).
- [7] I. Buluta, S. Ashhab, and F. Nori, *Rep. Prog. Phys.* **74**, 104401 (2011).
- [8] D. Jaksch, J. Cirac, P. Zoller, S. Rolston, R. Côté, and M. Lukin, *Phys. Rev. Lett.* **85**, 2208 (2000).
- [9] M. D. Lukin, M. Fleischhauer, R. Côté, L. M. Duan, D. Jaksch, J. I. Cirac, and P. Zoller, *Phys. Rev. Lett.* **87**, 037901 (2001).
- [10] M. Saffman, T. G. Walker, and K. Mølmer, *Rev. Mod. Phys.* **82**, 2313–2363 (2010).
- [11] C. S. Adams, J. D. Pritchard, and J. P. Shaffer, *J. Phys. B-At. Mol. Opt.* **53**, 012002 (2019).
- [12] H. Weimer, M. Müller, I. Lesanovsky, P. Zoller, and H. P. Büchler, *Nat. Phys.* **6**, 382 (2010).
- [13] H. Labuhn, D. Barredo, S. Ravets, S. de Léséleuc, T. Macrì, T. Lahaye, and A. Browaeys, *Nature* **534**, 667 (2016).
- [14] H. Bernien, S. Schwartz, A. Keesling, H. Levine, A. Omran, H. Pichler, S. Choi, A. S. Zibrov, M. Endres, M. Greiner, V. Vuletić, and M. D. Lukin, *Nature* **551**, 579 (2017).

-
- [15] O. Firstenberg, C. S. Adams, and S. Hofferberth, *J. Phys. B-At. Mol. Opt.* **49**, 152003 (2016).
- [16] J. Schmidt, Y. Münzenmaier, P. Kaspar, P. Schalberger, H. Baur, R. Löw, N. Fruehauf, T. Pfau, and H. Kübler, *J. Phys. B: At. Mol. Opt. Phys.* **53**, 094001 (2020).
- [17] D. Tong, S. M. Farooqi, J. Stanojevic, S. Krishnan, Y. P. Zhang, R. Côté, E. E. Eyler, and P. L. Gould, *Phys. Rev. Lett.* **93**, 063001 (2004).
- [18] T. Wilk, A. Gaëtan, C. Evellin, J. Wolters, Y. Miroshnychenko, P. Grangier, and A. Browaeys, *Phys. Rev. Lett.* **104**, 010502 (2010).
- [19] L. Isenhower, E. Urban, X. L. Zhang, A. T. Gill, T. Henage, T. A. Johnson, T. G. Walker, and M. Saffman, *Phys. Rev. Lett.* **104**, 010503 (2010).
- [20] E. Stourm, Y. Zhang, M. Lepers, R. Guérout, J. Robert, S. Nic Chormaic, K. Mølmer, and E. Brion, *J. Phys. B-At. Mol. Opt.* **52**, 045503 (2019).
- [21] E. Brion, F. Carlier, V. M. Akulin, and K. Mølmer, *Phys. Rev. A* **85**, 042324 (2012).
- [22] S. Spillane, G. Pati, K. Salit, M. Hall, P. Kumar, R. Beausoleil, and M. Shahriar, *Phys. Rev. Lett.* **100**, 233602 (2008).
- [23] S. Hendrickson, M. Lai, T. Pittman, and J. Franson, *Phys. Rev. Lett.* **105**, 173602 (2010).
- [24] T. Pittman, D. Jones, and J. Franson, *Phys. Rev. A* **88**, 053804 (2013).
- [25] D. Jones, J. Franson, and T. Pittman, *J. Opt. Soc. Am. B* **31**, 1997 (2014).
- [26] D. Jones, J. Franson, and T. Pittman, *Phys. Rev. A* **92**, 043806 (2015).
- [27] C. Foot, *Atomic Physics*, Oxford University Press (2005).
- [28] D. Alton, N. Stern, T. Aoki, H. Lee, E. Ostby, K. Vahala, and H. Kimble, *Nat. Phys.* **7**, 159 (2011).
- [29] K. Nayak, M. Das, F. Le Kien, and K. Hakuta, *Opt. Commun.* **285**, 4698 (2012).
- [30] M. Frawley, S. Nic Chormaic, and V. Minogin, *Phys. Scripta* **85**, 058103 (2012).
- [31] F. Le Kien, V. Balykin, and K. Hakuta, *Phys. Rev. A* **73**, 013819 (2006).
- [32] F. Le Kien and A. Rauschenbeutel, *Phys. Rev. A* **90**, 023805 (2014).
- [33] F. Le Kien, S. Gupta, V. Balykin, and K. Hakuta, *Phys. Rev. A* **72**, 032509 (2005).
- [34] K. Nayak, P. Melentiev, M. Morinaga, F. Le Kien, V. Balykin, and K. Hakuta, *Opt. Express* **15**, 5431 (2007).

-
- [35] A. Masalov and V. Minogin, *J. Exp. Theor. Phys*, **118**, 714 (2014).
- [36] L. Russell, D. Gleeson, V. Minogin, and S. Nic Chormaic, *J. Phys. B-At. Mol. Opt.* **42**, 185006 (2009).
- [37] V. G. Minogin and S. Nic Chormaic, *Laser Phys.* **20**, 32–37 (2010).
- [38] S. K. Ruddell, K. E. Webb, I. Herrera, A. S. Parkins, and M. D. Hoogerland, *Optica* **4**, 576–579 (2017).
- [39] J. Grover, P. Solano, L. Orozco, and S. Rolston, *Phys. Rev. A* **92**, 013850 (2015).
- [40] K. Kamitani, T. Muranaka, H. Takashima, M. Fujiwara, U. Tanaka, S. Takeuchi, and S. Urabe, *Opt. Express* **24**, 4672–4679 (2016).
- [41] M. Harlander, M. Brownnutt, W. Hänsel, and R. Blatt, *New J. Phys.* **12**, 093035 (2010).
- [42] F. L. Kien and K. Hakuta, *Adv. Nat. Sci.: Nanosci. Nanotechnol.* **3**, 035001 (2012).
- [43] M. Morrissey, K. Deasy, M. Frawley, R. Kumar, E. Prel, L. Russell, V. Truong, and S. Nic Chormaic, *Sensors* **13**, 10449 (2013).
- [44] R. Garcia-Fernandez, W. Alt, F. Bruse, C. Dan, K. Karapetyan, O. Rehband, A. Stiebeiner, U. Wiedemann, D. Meschede, and A. Rauschenbeutel, *Appl. Phys. B* **105**, 3 (2011).
- [45] L. Russell, K. Deasy, M. Daly, M. Morrissey, and S. Nic Chormaic, *Meas. Sci. Technol.* **23**, 015201 (2012).
- [46] M. Morrissey, K. Deasy, W. Yuqiang, S. Chakrabarti, and S. Nic Chormaic, *Rev. Sci. Instrum.* **80** (2009).
- [47] V. Balykin, K. Hakuta, F. Le Kien, J. Liang, and M. Morinaga, *Phys. Rev. A* **70**, 011401 (2004).
- [48] F. Le Kien, V. Balykin, and K. Hakuta, *Phys. Rev. A* **70**, 063403 (2004).
- [49] S. T. Dawkins, R. Mitsch, D. Reitz, E. Vetsch, and A. Rauschenbeutel, *Phys. Rev. Lett.* **107**, 243601 (2011).
- [50] E. Vetsch, S. Dawkins, R. Mitsch, D. Reitz, P. Schneeweiss, and A. Rauschenbeutel, *IEEE J. Sel. Top. Quant.* **18**, 1763 (2012).
- [51] A. Goban, K. Choi, D. Alton, D. Ding, C. Lacroûte, M. Pototschnig, T. Thiele, N. Stern, and H. Kimble, *Phys. Rev. Lett.* **109**, 033603 (2012).
- [52] T. Nieddu, V. Gokhroo, and S. Nic Chormaic, *J. Opt.* **18**, 053001 (2016).

- [53] P. Solano, J. A. Grover, J. E. Hoffman, S. Ravets, F. K. Fatemi, L. A. Orozco, and S. L. Rolston. *Chapter Seven - Optical Nanofibers: A New Platform for Quantum Optics*. In E. Arimondo, C. C. Lin, and S. F. Yelin, editors, *Advances In Atomic, Molecular, and Optical Physics*, volume 66, pages 439 – 505. Academic Press, (2017).
- [54] K. P. Nayak, M. Sadgrove, R. Yalla, F. L. Kien, and K. Hakuta, *J. Opt.* **20**, 073001 (2018).
- [55] C. Sayrin, C. Clausen, B. Albrecht, P. Schneeweiss, and A. Rauschenbeutel, *Optica* **2**, 353 (2015).
- [56] P. Solano, F. K. Fatemi, L. A. Orozco, and S. L. Rolston, *Opt. Lett.* **42**, 2283–2286 (2017).
- [57] J. Fu, X. Yin, and L. Tong, *J. Phys. B-At. Mol. Opt.* **40**, 4195–4210 (2007).
- [58] G. Sagué, A. Baade, and A. Rauschenbeutel, *New J. Phys.* **10**, 113008 (2008).
- [59] R. Yalla, F. Le Kien, M. Morinaga, and K. Hakuta, *Phys. Rev. Lett.* **109**, 063602 (2012).
- [60] R. Yalla, K. Nayak, and K. Hakuta, *Opt. Express* **20**, 2932 (2012).
- [61] K. M. Shafi, W. Luo, R. Yalla, K. Iida, E. Tsutsumi, A. Miyanaga, and K. Hakuta, *Sci. Rep.* **8**, 13494 (2018).
- [62] F. Le Kien and K. Hakuta, *Phys. Rev. A* **81**, 023812 (2010).
- [63] F. Le Kien and K. Hakuta, *Phys. Rev. A* **84**, 053801 (2011).
- [64] M. Fleischhauer, A. Imamoglu, and J. Marangos, *Rev. Mod. Phys.* **77**, 633 (2005).
- [65] F. Le Kien and K. Hakuta, *Phys. Rev. A* **79**, 013818 (2009).
- [66] R. Kumar, V. Gokhroo, and S. Nic Chormaic, *New J. Phys.* **17**, 123012 (2015).
- [67] B. Gouraud, D. Maxein, A. Nicolas, O. Morin, and J. Laurat, *Phys. Rev. Lett.* **114**, 180503 (2015).
- [68] T. Gallagher, *Rydberg Atoms*, University Press (2005).
- [69] R. Löw, H. Weimer, J. Nipper, J. B. Balewski, B. Butscher, H. P. Büchler, and T. Pfau, *J. Phys. B: At. Mol. Opt. Phys.* **45**, 113001 (2012).
- [70] J. Lim, H. Lee, and J. Ahn, *J. Korean Phys. Soc.* **63**, 867–876 (2013).
- [71] I. Mourachko, D. Comparat, F. de Tomasi, A. Fioretti, P. Nosbaum, V. M. Akulin, and P. Pillet, *Phys. Rev. Lett.* **80**, 253–256 (1998).
- [72] K. Singer, M. Reetz-Lamour, T. Amthor, L. G. Marcassa, and M. Weidemüller, *Phys. Rev. Lett.* **93**, 163001 (2004).

-
- [73] P. Schausz, M. Cheneau, M. Endres, T. Fukuhara, S. Hild, A. Omran, T. Pohl, C. Gross, S. Kuhr, and I. Bloch, *Nature* **491**, 87–91 (2012).
- [74] Y. Dudin and A. Kuzmich, *Science* **336**, 887 (2012).
- [75] D. B. Tretyakov, I. I. Beterov, V. M. Entin, I. I. Ryabtsev, and P. L. Chapovsky, *J. Exp. Theor. Phys* **108**, 374–383 (2009).
- [76] J. Pritchard, *Cooperative Optical Non-linearity in a Blockaded Rydberg Ensemble*, PhD Thesis, Department of Physics, Durham University (2011).
- [77] I. Friedler, D. Petrosyan, M. Fleischhauer, and G. Kurizki, *Phys. Rev. A* **72**, 043803 (2005).
- [78] A. Mohapatra, T. Jackson, and C. Adams, *Phys. Rev. Lett.* **98**, 113003 (2007).
- [79] T. Peyronel, O. Firstenberg, Q. Liang, S. Hofferberth, A. Gorshkov, T. Pohl, M. Lukin, and V. Vuletic, *Nature* **488**, 57 (2012).
- [80] J. Han, T. Vogt, M. Manjappa, R. Guo, M. Kiffner, and W. Li, *Phys. Rev. A* **92**, 063824 (2015).
- [81] W. Xu and B. DeMarco, *Phys. Rev. A* **93**, 011801 (2016).
- [82] J. Pritchard, A. Gauguet, K. Weatherill, and C. Adams, *J. Phys. B-At. Mol. Opt.* **44**, 184019 (2011).
- [83] S. Sevinçli, C. Ates, T. Pohl, H. Schempp, C. Hofmann, G. Günter, T. Amthor, M. Weidemüller, J. Pritchard, D. Maxwell, A. Gauguet, K. Weatherill, M. Jones, and C. Adams, *J. Phys. B-At. Mol. Opt.* **44**, 184018 (2011).
- [84] J. Pritchard, K. Weatherill, and C. Adams. *Nonlinear Optics Using Cold Rydberg Atoms*, chapter 8, page 301. World Scientific, (2013).
- [85] J. B. Naber, A. Tauschinsky, H. B. van Linden van den Heuvell, and R. J. C. Spreeuw, *SciPost Phys.* **2**, 015 (2017).
- [86] G. Günter, M. Robert-de Saint-Vincent, H. Schempp, C. S. Hofmann, S. Whitlock, and M. Weidemüller, *Phys. Rev. Lett.* **108**, 013002 (2012).
- [87] Z. Zhang, J. Che, D. Zhang, Z. Liu, X. Wang, and Y. Zhang, *Opt. Express* **23**, 13814–13822 (2015).
- [88] Z. Zhang, J. Guo, B. Gu, L. Hao, G. Yang, K. Wang, and Y. Zhang, *Photon. Res.* **6**, 713–720 (2018).
- [89] J. Che, Z. Zhang, M. Hu, X. Shi, and Y. Zhang, *Opt. Express* **26**, 3054–3066 (2018).
- [90] E. Brekke, J. O. Day, and T. G. Walker, *Phys. Rev. A* **78**, 063830 (2008).

- [91] A. Kölle, G. Epple, H. Kübler, R. Löw, and T. Pfau, *Phys. Rev. A* **85**, 063821 (2012).
- [92] M. Ferreira-Cao, V. Gavryusev, T. Franz, R. F. Alves, A. Signoles, G. Zürn, and M. Weidemüller, *J. Phys. B: At. Mol. Opt. Phys.* **53**, 084004 (2020).
- [93] J. O. Day, E. Brekke, and T. G. Walker, *Phys. Rev. A* **77**, 052712 (2008).
- [94] J. Bai, S. Liu, J. Wang, J. He, and J. Wang, *IEEE J. Sel. Top. Quant.* **26**, 1–6 (2020).
- [95] S. Dutta, J. Guest, D. Feldbaum, A. Walz-Flannigan, and G. Raithel, *Phys. Rev. Lett.* **85**, 5551 (2000).
- [96] S. Anderson, K. Younge, and G. Raithel, *Phys. Rev. Lett.* **107**, 263001 (2011).
- [97] S. Zhang, F. Robicheaux, and M. Saffman, *Phys. Rev. A* **84**, 043408 (2011).
- [98] D. Barredo, V. Lienhard, P. Scholl, S. de Léséleuc, T. Boulier, A. Browaeys, and T. Lahaye, *Phys. Rev. Lett.* **124**, 023201 (2020).
- [99] A. G. Boetes, R. V. Skannrup, J. Naber, S. J. J. M. F. Kokkelmans, and R. J. C. Spreeuw, *Phys. Rev. A* **97**, 013430 (2018).
- [100] Y. Pu and F. Dunning, *Phys. Rev. A* **88**, 012901 (2013).
- [101] C. Hermann-Avigliano, R. C. Teixeira, T. Nguyen, T. Cantat, G. Nogues, I. Dotsenko, S. Gleyzes, J. Raimond, S. Haroche, and M. Brune, *Phys. Rev. A* **90**, 040502 (2014).
- [102] J. Mozley, P. Hyafil, G. Nogues, M. Brune, J.-M. Raimond, and S. Haroche, *Eur. Phys. J. D* **35**, 43–57 (2005).
- [103] E. So, M. Dethlefsen, M. Ford, and T. P. Softley, *Phys. Rev. Lett.* **107**, 093201 (2011).
- [104] J. Crosse, S. Ellingsen, K. C., S. Buhmann, and S. Scheel, *Phys. Rev. A* **82**, 010901 (2010).
- [105] T. Peyrot, N. Šibalić, Y. R. P. Sortais, A. Browaeys, A. Sargsyan, D. Sarkisyan, I. G. Hughes, and C. S. Adams, *Phys. Rev. A* **100**, 022503 (2019).
- [106] J. Gutekunst, D. Weller, H. Kübler, J.-P. Negel, M. A. Ahmed, T. Graf, and R. Löw, *Appl. Opt.* **56**, 5898–5902 (2017).
- [107] H. Kübler, J. P. Shaffer, T. Baluktsian, R. Löw, and T. Pfau, *Nat. Photonics* **4**, 112–116 (2010).
- [108] A. Tauschinsky, R. M. T. Thijssen, S. Whitlock, H. B. van Linden van den Heuvell, and R. J. C. Spreeuw, *Phys. Rev. A* **81**, 063411 (2010).

-
- [109] V. Leung, D. Pijn, H. Schlatter, L. Torralbo-Campo, A. La Rooij, G. Mulder, J. Naber, M. Soudijn, A. Tauschinsky, C. Abarbanel, B. Hadad, E. Golan, R. Folman, and R. J. C. Spreeuw, *Rev. Sci. Instrum.* **85** (2014).
- [110] J. Naber, S. Machluf, L. Torralbo-Campo, M. Soudijn, N. Druten, H. Heuvell, and R. J. C. Spreeuw, *J. Phys. B-At. Mol. Opt.* **49**, 094005 (2016).
- [111] D. Davtyan, S. Machluf, M. L. Soudijn, J. B. Naber, N. J. van Druten, H. B. van Linden van den Heuvell, and R. J. C. Spreeuw, *Phys. Rev. A* **97**, 023418 (2018).
- [112] J. de Hond, R. van Bijnen, S. J. J. M. F. Kokkelmans, R. J. C. Spreeuw, H. van den Heuvell, and N. J. van Druten, *Phys. Rev. A* **98**, 062714 (2018).
- [113] Y. Chougale, J. Talukdar, T. Ramos, and R. Nath, *arXiv* **2003.09885** (2020).
- [114] G. Epple, K. S. Kleinbach, T. G. Euser, N. Y. Joly, T. Pfau, P. S. J. Russell, and R. Löw, *Nat. Commun.* **5**, 4132 (2014).
- [115] G. Epple, N. Y. Joly, T. G. Euser, P. S. Russell, and R. Löw, *Opt. Lett.* **42**, 3271–3274 (2017).
- [116] M. Langbecker, M. Noaman, N. Kjærgaard, F. Benabid, and P. Windpassinger, *Phys. Rev. A* **96**, 041402 (2017).
- [117] J. A. Sedlacek, E. Kim, S. T. Rittenhouse, P. F. Weck, H. R. Sadeghpour, and J. P. Shaffer, *Phys. Rev. Lett.* **116**, 133201 (2016).
- [118] E. Stourm, M. Lepers, J. Robert, S. Nic Chormaic, K. Mølmer, and E. Brion, *Phys. Rev. A* **101**, 052508 (2020).
- [119] J. Lee, J. A. Grover, J. E. Hoffman, L. A. Orozco, and S. L. Rolston, *J. Phys. B-At. Mol. Opt.* **48**, 165004 (2015).
- [120] S. Lee, K. Ravi, and S. A. Rangwala, *Phys. Rev. A* **87**, 052701 (2013).
- [121] G. Tkachenko, F. Lei, and S. Nic Chormaic, *J. Opt.* **21**, 125604 (2019).
- [122] R. W. Boyd, *Nonlinear Optics*, Elsevier Science, 3 edition (2008).
- [123] N. Bloembergen. *Recent Progress in Four-Wave Mixing Spectroscopy*. In H. Walther and K. W. Rothe, editors, *Laser Spectroscopy IV*, pages 340–348. Springer Berlin Heidelberg, (1979).
- [124] S. Liu, Y. Zhang, H. Wu, and P. Yuan, *J. Opt. Soc. Am. B* **28**, 1100–1103 (2011).
- [125] J. D. Pritchard, D. Maxwell, A. Gauguier, K. J. Weatherill, M. P. A. Jones, and C. S. Adams, *Phys. Rev. Lett.* **105**, 193603 (2010).
- [126] U. Raitzsch, R. Heidemann, H. Weimer, B. Butscher, P. Kollmann, R. Löw, H. P. Büchler, and T. Pfau, *New J. Phys.* **11**, 055014 (2009).

- [127] C. Liu, J. F. Chen, S. Zhang, S. Zhou, Y.-H. Kim, M. M. T. Loy, G. K. L. Wong, and S. Du, *Phys. Rev. A* **85**, 021803 (2012).
- [128] M. M. Salour, *Ann. Phys.* **111**, 364–503 (1978).
- [129] G. Grynberg and B. Cagnac, *Rep. Prog. Phys.* **40**, 791 (1977).
- [130] K. D. Bonin and T. J. McIlrath, *J. Opt. Soc. Am. B* **1**, 52–55 (1984).
- [131] N. Melikechi and L. Allen, *J. Opt. Soc. Am. B* **3**, 41–44 (1986).
- [132] B. W. Shore, *Acta Phys. Slovaca* **58**, 243–486 (2008).
- [133] N. Hayashi, A. Fujisawa, H. Kido, K. ichi Takahashi, and M. Mitsunaga, *J. Opt. Soc. Am. B* **27**, 1645–1650 (2010).
- [134] D. Grischkowsky, *Phys. Rev. A* **14**, 802–812 (1976).
- [135] R. Loudon, *The Quantum Theory of Light*, Oxford University Press (2000).
- [136] J. Rydberg, *The London, Edinburgh, and Dublin Philosophical Magazine and Journal of Science* **29**, 331–337 (1890).
- [137] M. Mack, F. Karlewski, H. Hattermann, S. Höckh, F. Jessen, D. Cano, and J. Fortágh, *Phys. Rev. A* **83**, 052515 (2011).
- [138] C. J. Lorenzen and K. Niemax, *Phys. Scripta* **27**, 300 (1983).
- [139] A. Messiah, *Quantum Mechanics*, North-Holland Publishing Company, 4 edition (1967).
- [140] J. Rydberg Ph.D., *Phil. Mag.* **29**, 331 (1890).
- [141] Gounand, F., *J. Phys. France* **40**, 457 (1979).
- [142] T. L. Nguyen, *Study of Dipole-Dipole Interaction Between Rydberg Atoms Toward Quantum Simulation with Rydberg Atoms*, PhD Thesis, Département de Physique, De Ecole Normale Supérieure, Laboratoire Kastler Brossel (2016).
- [143] J. Ward, A. Maimaiti, V. Le, and S. Nic Chormaic, *Rev. Sci. Instrum.* **85** (2014).
- [144] T. E. Dimmick, G. Kakarantzas, T. A. Birks, and P. S. J. Russell, *Appl. Opt.* **38**, 6845–6848 (1999).
- [145] L. Shi, X. Chen, H. Liu, Y. Chen, Z. Ye, W. Liao, and Y. Xia, *Opt. Express* **14**, 5055–5060 (2006).
- [146] T. A. Birks and Y. W. Li, *J. Lightwave Technol.* **10**, 432–438 (1992).
- [147] T. Nieddu, *Optical Nanofibers for Multiphoton Processes and Selective Mode Interactions with Rubidium*, PhD Thesis, OIST Graduate University (2019).

-
- [148] G. Gynberg, A. Aspect, and C. Fabre, *Introduction to Quantum Optics*, University Press, 1 edition (2010).
- [149] H. J. Metcalf and P. van der Straten, *Laser Cooling and Trapping*, Springer-Verlag (1999).
- [150] C. Foot, *Atomic Physics*, Oxford University Press (2013).
- [151] D. Steck. *Rubidium 87 D line data*, (2008).
- [152] A. M. Steane, M. Chowdhury, and C. J. Foot, J. Opt. Soc. Am. B **9**, 2142–2158 (1992).
- [153] C. G. Townsend, N. H. Edwards, C. J. Cooper, K. P. Zetie, C. J. Foot, A. M. Steane, P. Szriftgiser, H. Perrin, and J. Dalibard, Phys. Rev. A **52**, 1423–1440 (1995).
- [154] C. Monroe, W. Swann, H. Robinson, and C. Wieman, Phys. Rev. Lett. **65**, 1571–1574 (1990).
- [155] A. Mohapatra, *Study of Atom-Surface Interaction using Laser Cooled Atoms*, PhD Thesis, Tata Institute of Fundamental Research (2005).
- [156] P. Anderson, S. Jalnapurkar, E. S. Moiseev, D. Chang, P. E. Barclay, A. Lezama, and A. I. Lvovsky, AIP Advances **8**, 055005 (2018).
- [157] E. Vetsch, D. Reitz, G. Sagué, R. Schmidt, S. T. Dawkins, and A. Rauschenbeutel, Phys. Rev. Lett. **104**, 203603 (2010).
- [158] F. Le Kien, T. Ray, T. Nieddu, T. Busch, and S. Nic Chormaic, Phys. Rev. A **97**, 013821 (2018).
- [159] N. V. Corzo, A. Raskop, J. Chandra, A. S. Sheremet, B. Gouraud, and J. Laurat, Nature **556**, 359–362 (2019).
- [160] D. Yu, L. C. Kwek, L. Amico, and R. Dumke, Quantum Sci. Technol. **2**, 035005 (2017).
- [161] R. P. Abel, A. K. Mohapatra, M. G. Bason, J. D. Pritchard, K. J. Weatherill, U. Raitzsch, and C. S. Adams, Appl. Phys. Lett. **94**, 071107 (2009).
- [162] F. Le Kien, V. Balykin, and K. Hakuta, Phys. Rev. A **70**, 063403 (2004).
- [163] B. D. Patterson, P. Solano, P. S. Julienne, L. A. Orozco, and S. L. Rolston, Phys. Rev. A **97**, 032509 (2018).
- [164] W. Li, P. J. Tanner, and T. F. Gallagher, Phys. Rev. Lett. **94**, 173001 (2005).
- [165] K. J. Weatherill, J. D. Pritchard, R. P. Abel, M. G. Bason, A. K. Mohapatra, and C. S. Adams, J. Phys. B: At. Mol. Opt. Phys. **41**, 201002 (2008).

- [166] M. Marcuzzi, J. Minář, D. Barredo, S. de Léséleuc, H. Labuhn, T. Lahaye, A. Browaeys, E. Levi, and I. Lesanovsky, *Phys. Rev. Lett.* **118**, 063606 (2017).
- [167] D. P. Fahey and M. W. Noel, *Opt. Express* **19**, 17002–17012 (2011).
- [168] F. Camargo, R. Schmidt, J. D. Whalen, R. Ding, G. Woehl, S. Yoshida, J. Burgdörfer, F. B. Dunning, H. R. Sadeghpour, E. Demler, and T. C. Killian, *Phys. Rev. Lett.* **120**, 083401 (2018).
- [169] Y. Miroshnychenko, A. Gaëtan, C. Evellin, P. Grangier, D. Comparat, P. Pillet, T. Wilk, and A. Browaeys, *Phys. Rev. A* **82**, 013405 (2010).
- [170] Z. Zuo, M. Fukusen, Y. Tamaki, T. Watanabe, Y. Nakagawa, and K. Nakagawa, *Opt. Express* **17**, 22898–22905 (2009).
- [171] K. Shimoda, *High-Resolution Laser Spectroscopy*, Springer-Verlag (2014).
- [172] L. S. Vasilenko, V. P. Chebotaev, and A. V. Shishaev, *JETP Lett.* **12**, 113–115 (1970).
- [173] B. Cagnac, G. Grynberg, and F. Biraben, *Journal de Physique* **34**, 845–858 (1973).
- [174] N. Bloembergen, M. D. Levenson, and M. M. Salour, *Phys. Rev. Lett.* **32**, 867–869 (1974).
- [175] T. W. Hänsch, *Rev. Mod. Phys.* **78**, 1297–1309 (2006).
- [176] S. Gulde, H. Häffner, M. Riebe, G. Lancaster, C. Becher, J. Eschner, F. Schmidt-Kaler, I. L. Chuang, and R. Blatt, *Philos. T Roy. Soc. A* **361**, 1363–1374 (2003).
- [177] I. D. Abella, *Phys. Rev. Lett.* **9**, 453–455 (1962).
- [178] F. Biraben, B. Cagnac, and G. Grynberg, *Phys. Lett. A* **49**, 71 – 72 (1974).
- [179] D. Roberts and E. Fortson, *Opt. Commun.* **14**, 332 – 335 (1975).
- [180] E. Campani, G. Degan, G. Gorini, and E. Polacco, *Opt. Commun.* **24**, 203 – 206 (1978).
- [181] Y.-W. Liu and P. E. G. Baird, *Meas. Sci. Technol.* **12**, 740 (2001).
- [182] B. A. Bushaw, W. Nörtershäuser, G. Ewald, A. Dax, and G. W. F. Drake, *Phys. Rev. Lett.* **91**, 043004 (2003).
- [183] M.-S. Ko and Y.-W. Liu, *Opt. Lett.* **29**, 1799–1801 (2004).
- [184] Y.-C. Lee, Y.-H. Chang, Y.-Y. Chen, C.-C. Tsai, and H.-C. Chui, *J. Phys. B-At. Mol. Opt.* **43**, 235003 (2010).
- [185] T. W. Hänsch, S. A. Lee, R. Wallenstein, and C. Wieman, *Phys. Rev. Lett.* **34**, 307–309 (1975).

-
- [186] A. Matveev, C. G. Parthey, K. Predehl, J. Alnis, A. Beyer, R. Holzwarth, T. Udem, T. Wilken, N. Kolachevsky, M. Abgrall, D. Rovera, C. Salomon, P. Laurent, G. Grosche, O. Terra, T. Legero, H. Schnatz, S. Weyers, B. Altschul, and T. W. Hänsch, *Phys. Rev. Lett.* **110**, 230801 (2013).
- [187] R. Roy, P. C. Condylis, Y. J. Johnathan, and B. Hessmo, *Opt. Express* **25**, 7960–7969 (2017).
- [188] T. Chanelière, D. N. Matsukevich, S. D. Jenkins, T. A. B. Kennedy, M. S. Chapman, and A. Kuzmich, *Phys. Rev. Lett.* **96**, 093604 (2006).
- [189] A. Pérez Galván, Y. Zhao, and L. A. Orozco, *Phys. Rev. A* **78**, 012502 (2008).
- [190] E. Gomez, F. Baumer, A. D. Lange, G. D. Sprouse, and L. A. Orozco, *Phys. Rev. A* **72**, 012502 (2005).
- [191] K. D. Bonin and T. J. McIlrath, *J. Opt. Soc. Am. B* **1**, 52–55 (1984).
- [192] G. Sagué, E. Vetsch, W. Alt, D. Meschede, and A. Rauschenbeutel, *Phys. Rev. Lett.* **99**, 163602 (2007).
- [193] G. Tkachenko, I. Toftul, C. Esporlas, A. Maimaiti, F. Le Kien, V. G. Truong, and S. Nic Chormaic, *Optica* **7**, 59–62 (2020).
- [194] F. Biraben, B. Cagnac, and G. Grynberg, *Phys. Rev. Lett.* **32**, 643–645 (1974).
- [195] M. D. Levenson and N. Bloembergen, *Phys. Rev. Lett.* **32**, 645–648 (1974).
- [196] S. Wang, J. Yuan, L. Wang, L. Xiao, and S. Jia, *Laser Phys. Lett.* **16**, 125204 (2019).
- [197] K. Y. Bliokh, Y. Gorodetski, V. Kleiner, and E. Hasman, *Phys. Rev. Lett.* **101**, 030404 (2008).
- [198] F. Le Kien and A. Rauschenbeutel, *Phys. Rev. A* **88**, 063845 (2013).
- [199] F. Le Kien, J. Q. Liang, K. Hakuta, and V. I. Balykin, *Opt. Commun.* **242**, 445–455 (2004).
- [200] L. Tong, J. Lou, and E. Mazur, *Opt. Express* **12**, 1025–1035 (2004).
- [201] F. Le Kien, T. Busch, V. G. Truong, and S. Nic Chormaic, *Phys. Rev. A* **96**, 023835 (2017).
- [202] S. M. Spillane, G. S. Pati, K. Salit, M. Hall, P. Kumar, R. G. Beausoleil, and M. S. Shahriar, *Phys. Rev. Lett.* **100**, 233602 (2008).
- [203] M. Babiker, C. R. Bennett, D. L. Andrews, and L. C. Dávila Romero, *Phys. Rev. Lett.* **89**, 143601 (2002).
- [204] M. F. Andersen, C. Ryu, P. Cladé, V. Natarajan, A. Vaziri, K. Helmerson, and W. D. Phillips, *Phys. Rev. Lett.* **97**, 170406 (2006).

- [205] R. Jones, G. Buonaiuto, B. Lang, I. Lesanovsky, and B. Olmos, *Phys. Rev. Lett.* **124**, 093601 (2020).
- [206] C. S. Wood, S. C. Bennett, D. Cho, B. P. Masterson, J. L. Roberts, C. E. Tanner, and C. E. Wieman, *Science* **275**, 1759–1763 (1997).
- [207] B. J. Wundt, C. T. Munger, and U. D. Jentschura, *Phys. Rev. X* **2**, 041009 (2012).
- [208] M. M. Müller, A. Kölle, R. Löw, T. Pfau, T. Calarco, and S. Montangero, *Phys. Rev. A* **87**, 053412 (2013).
- [209] M. Saffman and T. G. Walker, *Phys. Rev. A* **66**, 065403 (2002).
- [210] H. Gorniaczyk, C. Tresp, J. Schmidt, H. Fedder, and S. Hofferberth, *Phys. Rev. Lett.* **113**, 053601 (2014).
- [211] D. Tiarks, S. Baur, K. Schneider, S. Dürr, and G. Rempe, *Phys. Rev. Lett.* **113**, 053602 (2014).
- [212] J. Huang, *Two-Photon Absorption and Two-Photon-Resonant Four-Wave Mixing for the Tb^{3+} Ion in Insulators*, PhD Thesis, Montana State University (1987).
- [213] Z. Tong, C. Lundström, P. A. Andrekson, C. J. McKinstrie, M. Karlsson, D. J. Blessing, E. Tipsuwannakul, B. J. Puttnam, H. Toda, and L. Grüner-Nielsen, *Nat. Photonics* **5**, 430–436 (2011).
- [214] A. Yariv and D. M. Pepper, *Opt. Lett.* **1**, 16–18 (1977).
- [215] M. Cronin-Golomb, B. Fischer, J. O. White, and A. Yariv, *Appl. Phys. Lett.* **41**, 689–691 (1982).
- [216] H. J. Gerritsen, *Appl. Phys. Lett.* **10**, 239–241 (1967).
- [217] A. Yariv, *IEEE J. Sel. Top. Quant.* **14**, 650–660 (1978).
- [218] J. F. Reintjes, *Nonlinear Optical Parametric Processes in Liquids and Gases*, Academic Press (1984).
- [219] A. Kuzmich, W. P. Bowen, A. D. Boozer, A. Boca, C. W. Chou, L.-M. Duan, and H. J. Kimble, *Nature* **423**, 731–734 (2003).
- [220] B. Srivathsan, G. K. Gulati, B. Chng, G. Maslennikov, D. Matsukevich, and C. Kurtsiefer, *Phys. Rev. Lett.* **111**, 123602 (2013).
- [221] L. Zhu, X. Guo, C. Shu, H. Jeong, and S. Du, *Appl. Phys. Lett.* **110**, 161101 (2017).
- [222] Y.-S. Lee, S. M. Lee, H. Kim, and H. S. Moon, *Opt. Express* **24**, 28083–28091 (2016).

-
- [223] R. T. Willis, F. E. Becerra, L. A. Orozco, and S. L. Rolston, *Phys. Rev. A* **82**, 053842 (2010).
- [224] K. T. Kaczmarek, P. M. Ledingham, B. Brecht, S. E. Thomas, G. S. Thekkadath, O. Lazo-Arjona, J. H. D. Munns, E. Poem, A. Feizpour, D. J. Saunders, J. Nunn, and I. A. Walmsley, *Phys. Rev. A* **97**, 042316 (2018).
- [225] R. Finkelstein, E. Poem, O. Michel, O. Lahad, and O. Firstenberg, *Sci. Adv.* **4** (2018).
- [226] G. S. Agarwal, *Phys. Rev. Lett.* **57**, 827–830 (1986).
- [227] R. E. Slusher, L. W. Hollberg, B. Yurke, J. C. Mertz, and J. F. Valley, *Phys. Rev. Lett.* **55**, 2409–2412 (1985).
- [228] J. Park and H. S. Moon, *Opt. Express* **26**, 14461–14471 (2018).
- [229] K.-K. Park, J.-H. Kim, T.-M. Zhao, Y.-W. Cho, and Y.-H. Kim, *Optica* **4**, 1293–1297 (2017).
- [230] T. Jeong, J. Park, and H. S. Moon, *Phys. Rev. A* **100**, 033818 (2019).
- [231] R. Henke, *A Two-Colour Fibre Trap for Cold Atom-Based Multiphoton Processes*, Master’s Thesis, Westfälische Wilhelms-Universität Münster (2020).
- [232] B. Srivathsan, G. K. Gulati, B. Chng, G. Maslennikov, D. Matsukevich, and C. Kurtsiefer, *Phys. Rev. Lett.* **111**, 123602 (2013).
- [233] D. Marcuse, *Light Transmission Optics*, Van nostrand reinhold company (1989).

Appendix A

Modes in Optical Nanofibres

A.1 Eigenvalue Equations from Maxwell's Equations

This section of the appendix introduces light propagation in optical nanofibres and explains the field distribution in the core and cladding of the ONF. Light is an electromagnetic wave and the propagation of light in the absence of currents and charges, in a linear isotropic medium, can be described using Maxwell's equations [233]

$$\begin{aligned}\nabla \times \mathbf{H} &= \frac{\partial \mathbf{D}}{\partial t}, & \nabla \cdot \mathbf{B} &= 0, \\ \nabla \times \mathbf{E} &= -\frac{\partial \mathbf{B}}{\partial t}, & \nabla \cdot \mathbf{D} &= 0.\end{aligned}\tag{A.1}$$

where \mathbf{H} is the magnetic field intensity vector, $\mathbf{D} = \varepsilon \mathbf{E}$ is the electric displacement vector, \mathbf{E} is the electric field intensity vector, $\mathbf{B} = \mu \mathbf{H}$ is the magnetic flux density vector, ε is dielectric permittivity and μ is magnetic permeability. Using A.1, the wave equation of light propagation can be derived as

$$\nabla^2 \mathbf{E} + \nabla \left[\mathbf{E} \cdot \frac{\nabla \varepsilon}{\varepsilon} \right] = \varepsilon \mu \frac{\partial^2 \mathbf{E}}{\partial t^2}.\tag{A.2}$$

The wave equation for the magnetic field \mathbf{B} takes a similar form as Eqn. A.2. Consider a cylindrical symmetric waveguide, *i.e.* an optical fibre, with the axis along the z -direction and cross-section on the x - y plane, when ε is constant, second term in LHS of A.2 vanishes. The solution of Eqn. A.2, the mode propagating along the fibre, takes the form

$$\begin{aligned}\mathbf{E} &= \mathcal{E}(x, y) e^{i(\omega t - \beta z)}, \\ \mathbf{H} &= \mathcal{H}(x, y) e^{i(\omega t - \beta z)}.\end{aligned}\tag{A.3}$$

where β is the axial propagation constant of the field and ω is the angular frequency. Replacing the above equations for \mathbf{E} and \mathbf{H} in Eqns. A.1, we get [233]

$$\begin{aligned} \frac{\partial H_z}{\partial y} + i\beta H_y &= i\omega\varepsilon E_x, \\ -i\beta H_x - \frac{\partial H_z}{\partial x} &= i\omega\varepsilon E_y, \\ \frac{\partial H_y}{\partial x} - \frac{\partial H_x}{\partial y} &= i\omega\varepsilon E_z, \end{aligned} \quad (\text{A.4})$$

$$\begin{aligned} \frac{\partial E_z}{\partial y} + i\beta E_y &= -i\omega\mu H_x, \\ i\beta E_x + \frac{\partial E_z}{\partial x} &= i\omega\mu H_y, \\ \frac{\partial E_y}{\partial x} - \frac{\partial E_x}{\partial y} &= -i\omega\mu H_z. \end{aligned} \quad (\text{A.5})$$

Using the above set of equations, the transverse field components of \mathbf{E} and \mathbf{H} in terms of E_z and H_z are

$$E_x = -\left(\frac{i}{\kappa^2}\right) \left(\beta \frac{\partial E_z}{\partial x} + \omega\mu \frac{\partial H_z}{\partial y}\right), \quad (\text{A.6})$$

$$E_y = -\left(\frac{i}{\kappa^2}\right) \left(\beta \frac{\partial E_z}{\partial y} - \omega\mu \frac{\partial H_z}{\partial x}\right), \quad (\text{A.7})$$

$$H_x = -\left(\frac{i}{\kappa^2}\right) \left(\beta \frac{\partial H_z}{\partial x} - \omega\varepsilon \frac{\partial E_z}{\partial y}\right), \quad (\text{A.8})$$

$$H_y = -\left(\frac{i}{\kappa^2}\right) \left(\beta \frac{\partial H_z}{\partial y} + \omega\varepsilon \frac{\partial E_z}{\partial x}\right). \quad (\text{A.9})$$

where $\kappa^2 = k^2 - \beta^2$ and $k^2 = \omega^2\varepsilon\mu$. Using the expressions for H_x , H_y , E_x and E_y in Eqns. A.4 and A.5, we get wave equations for the z -component as

$$\begin{aligned} \frac{\partial^2 E_z}{\partial x^2} + \frac{\partial^2 E_z}{\partial y^2} + \kappa^2 E_z &= 0, \\ \frac{\partial^2 H_z}{\partial x^2} + \frac{\partial^2 H_z}{\partial y^2} + \kappa^2 H_z &= 0. \end{aligned} \quad (\text{A.10})$$

Equations A.5–A.9 are exact, but Eqn. A.10 is exact only for constant ε ; however, they are correct in our situation as they are only applied in the regions with homogeneous refractive indices. Rewriting the Eqns A.6–A.10 in cylindrical co-ordinates, we get

$$E_r = -\left(\frac{i\beta}{\kappa^2}\right) \left(\frac{\partial E_z}{\partial r} + \frac{\omega\mu}{\beta} \frac{1}{r} \frac{\partial H_z}{\partial \phi}\right), \quad (\text{A.11})$$

$$E_\phi = -\left(\frac{i\beta}{\kappa^2}\right) \left(\frac{1}{r} \frac{\partial E_z}{\partial \phi} - \frac{\omega\mu}{\beta} \frac{\partial H_z}{\partial r}\right), \quad (\text{A.12})$$

$$H_r = -\left(\frac{i\beta}{\kappa^2}\right) \left(\frac{\partial H_z}{\partial r} - \frac{\omega\varepsilon}{\beta} \frac{1}{r} \frac{\partial E_z}{\partial \phi}\right), \quad (\text{A.13})$$

$$H_\phi = -\left(\frac{i\beta}{\kappa^2}\right) \left(\frac{1}{r} \frac{\partial H_z}{\partial \phi} + \frac{\omega\varepsilon}{\beta} \frac{\partial E_z}{\partial r}\right), \quad (\text{A.14})$$

Now the solution of the problem can be obtained by solving the following wave equations,

$$\frac{\partial^2 E_z}{\partial r^2} + \frac{1}{r} \frac{\partial E_z}{\partial r} + \frac{1}{r^2} \frac{\partial^2 E_z}{\partial \phi^2} + \kappa^2 E_z = 0, \quad (\text{A.15})$$

$$\frac{\partial^2 H_z}{\partial r^2} + \frac{1}{r} \frac{\partial H_z}{\partial r} + \frac{1}{r^2} \frac{\partial^2 H_z}{\partial \phi^2} + \kappa^2 H_z = 0. \quad (\text{A.16})$$

The axial components of the fields can be written with solutions of Eqn. A.3 as

$$E_z(r, \phi, z, t) = E_z(r, \phi) e^{i(\omega t - \beta z)}, \quad (\text{A.17})$$

$$H_z(r, \phi, z, t) = H_z(r, \phi) e^{i(\omega t - \beta z)}. \quad (\text{A.18})$$

The solution for Eqn. A.15 is of the form

$$E_z(r, \phi) = R(r) e^{il\phi}, \quad (\text{A.19})$$

where l must be a positive or negative integer or zero to ensure that the field is periodic in ϕ with a period of 2π . Using Eqn. A.19 into Eqn. A.15, we get

$$\left(\frac{\partial^2}{\partial r^2} + \frac{1}{r} \frac{\partial}{\partial r} + \frac{1}{r^2} \frac{\partial^2}{\partial \phi^2} + \kappa^2 - \frac{l^2}{r^2} \right) R(r) = 0, \quad (\text{A.20})$$

which is a differential equation for Bessel functions with a general solution depending on the sign of κ^2 such that

$$R(r) = A J_l(\kappa r) + B Y_l(\kappa r), \quad \kappa^2 > 0, \quad (\text{A.21})$$

$$R(r) = C I_l(|\kappa|r) + D K_l(|\kappa|r), \quad \kappa^2 < 0, \quad (\text{A.22})$$

where $J_l(\kappa r)$ and $Y_l(\kappa r)$ are the Bessel functions of the first and the second kind and $I_l(|\kappa|r)$ and $K_l(|\kappa|r)$ are the modified Bessel functions of the first and the second kind, respectively. These are monotonically increasing and decreasing functions of r . Y_l is singular at $r = 0$ and I_l diverges as $r \rightarrow \infty$, and we consider such solutions to be physically unreasonable. Then, Eqn. A.21 and Eqn. A.22 are reduced to

$$R(r) = A J_l(\kappa r), \quad \kappa^2 > 0, \quad (\text{A.23})$$

$$R(r) = C K_l(|\kappa|r), \quad \kappa^2 < 0. \quad (\text{A.24})$$

Let us consider an optical fibre with refractive indices of the core and the cladding being n_1 and n_2 , respectively, where $n_1 > n_2$ and take k_0 as the free space wavenumber. Thus, the wavenumber in the core is $k_1 = n_1 k_0$ and in the cladding is $k_2 = n_2 k_0$. For bound rays, *i.e.* lossless modes confined to the core, we see

$$k_2 < \beta < k_1. \quad (\text{A.25})$$

In the core, $\kappa^2 > 0$, hence we have that

$$\kappa = h = \sqrt{k_1^2 - \beta^2} = \sqrt{n_1^2 k_0^2 - \beta^2}. \quad (\text{A.26})$$

In the cladding, $\kappa^2 > 0$,

$$|\kappa| = q = \sqrt{\beta^2 - k_2^2} = \sqrt{\beta^2 - n_2^2 k_0^2}. \quad (\text{A.27})$$

Thereby we can write the field component of the field inside the core as

$$E_z(r, \phi, z, t) = AJ_l(hr)e^{i(\omega t - \beta z + l\phi)}, \quad (\text{A.28})$$

$$H_z(r, \phi, z, t) = PJ_l(hr)e^{i(\omega t - \beta z + l\phi)}, \quad (\text{A.29})$$

and outside the core as

$$E_z(r, \phi, z, t) = CK_l(qr)e^{i(\omega t - \beta z + l\phi)}. \quad (\text{A.30})$$

$$H_z(r, \phi, z, t) = QK_l(qr)e^{i(\omega t - \beta z + l\phi)}. \quad (\text{A.31})$$

Using the equations above and considering the radius of the fibre to be a , we have, for $r < a$

$$\begin{aligned} E_r(r, \phi, z, t) &= -\frac{i}{h^2} \left[\beta h A J_l'(hr) + i\omega\mu_0 \frac{l}{r} P J_l(hr) \right] e^{i(\omega t - \beta z + l\phi)}, \\ E_\phi(r, \phi, z, t) &= -\frac{i}{h^2} \left[i\beta \frac{l}{r} A J_l(hr) - h\omega\mu_0 P J_l'(hr) \right] e^{i(\omega t - \beta z + l\phi)}, \\ E_z(r, \phi, z, t) &= A J_l(hr) e^{i(\omega t - \beta z + l\phi)}, \\ H_r(r, \phi, z, t) &= -\frac{i}{h^2} \left[-i\omega\varepsilon_1 \frac{l}{r} A J_l(hr) + h\beta P J_l'(hr) \right] e^{i(\omega t - \beta z + l\phi)}, \\ H_\phi(r, \phi, z, t) &= -\frac{i}{h^2} \left[h\omega\varepsilon_1 A J_l'(hr) + i\beta \frac{l}{r} P J_l(hr) \right] e^{i(\omega t - \beta z + l\phi)}, \\ H_z(r, \phi, z, t) &= P J_l(hr) e^{i(\omega t - \beta z + l\phi)}. \end{aligned} \quad (\text{A.32})$$

where $J_l'(hr) = \frac{J_l(hr)}{hr}$ and $\varepsilon_1 = n_1^2 \varepsilon_0$ is the dielectric constant of the core. For $r > a$

$$\begin{aligned} E_r(r, \phi, z, t) &= \frac{i}{q^2} \left[\beta q C K_l'(qr) + i\omega\mu_0 \frac{l}{r} Q K_l(qr) \right] e^{i(\omega t - \beta z + l\phi)}, \\ E_\phi(r, \phi, z, t) &= \frac{i}{q^2} \left[i\beta \frac{l}{r} C K_l(qr) - q\omega\mu_0 Q K_l'(qr) \right] e^{i(\omega t - \beta z + l\phi)}, \\ E_z(r, \phi, z, t) &= C K_l(qr) e^{i(\omega t - \beta z + l\phi)}, \\ H_r(r, \phi, z, t) &= \frac{i}{q^2} \left[-i\omega\varepsilon_2 \frac{l}{r} C K_l(qr) + q\beta Q K_l'(qr) \right] e^{i(\omega t - \beta z + l\phi)}, \\ H_\phi(r, \phi, z, t) &= \frac{i}{q^2} \left[q\omega\varepsilon_2 C K_l'(qr) + i\beta \frac{l}{r} Q K_l(qr) \right] e^{i(\omega t - \beta z + l\phi)}, \\ H_z(r, \phi, z, t) &= Q K_l(qr) e^{i(\omega t - \beta z + l\phi)}. \end{aligned} \quad (\text{A.33})$$

where $K_l'(qr) = \frac{K_l(qr)}{qr}$ and $\varepsilon_2 = n_2^2 \varepsilon_0$ is the dielectric constant of the medium surrounding the core [233].

The set of equations above, *i.e.* Eqns. A.32 and A.33 are the solutions to Maxwell's equation, but in order to describe the modes of a fibre they must satisfy boundary conditions at the core-cladding interface, *i.e.* at $r = a$. The constants A, C, P and Q can be determined by the boundary conditions. Equating the tangential components, E_z, E_ϕ, H_z and H_ϕ at $r = a$, we get a set of four equations:

$$\begin{aligned} 0 &= J_l(ha)A - K_l(qa)C, \\ 0 &= PJ_l(ha) - K_l(qa)Q, \\ 0 &= \frac{i\beta l}{h^2 a} J_l(ha)A - \frac{\omega\mu_0}{h} J'_l(ha)P + \frac{i\beta l}{q^2 a} K_l(qa)C - \frac{\omega\mu_0}{q} K'_l(qa)Q, \\ 0 &= \frac{\omega\varepsilon_1}{h} J'_l(ha)A + \frac{i\beta l}{h^2 a} J_l(ha)P + \frac{\omega\varepsilon_2}{q} K'_l(qa)C + \frac{i\beta l}{q^2 a} K_l(qa)Q. \end{aligned} \quad (\text{A.34})$$

Equation A.34 can have solutions only if the determinant of the equation system vanishes. The condition for the determinant to be zero is called an eigenvalue equation and is given as

$$\left(\frac{J'_l(ha)}{haJ_l(ha)} + \frac{K'_l(qa)}{qaK_l(qa)} \right) \left(\frac{J'_l(ha)}{haJ_l(ha)} + \frac{n_2^2 K'_l(qa)}{n_1^2 qaK_l(qa)} \right) = l^2 \left(\frac{\beta}{kn_1} \right)^2 \left[\left(\frac{1}{ha} \right)^2 + \left(\frac{1}{qa} \right)^2 \right]^2. \quad (\text{A.35})$$

Each of the eigenvalues, β , obtained from this equation describes a propagation mode of the fibre. The eigenvalue equation can be rewritten for the four possible guided modes inside the step index fibre; namely transverse magnetic (TM), transverse electric (TE), hybrid electric (HE) and electric hybrid (EH). For the TE_{0m} mode, where $E_z = 0$, we have

$$\frac{J_1(ha)}{haJ_0(ha)} + \frac{K_1(qa)}{qaK_0(qa)} = 0. \quad (\text{A.36})$$

For the TM_{0m} modes, where $H_z = 0$,

$$\frac{J_1(ha)}{haJ_0(ha)} + \frac{n_2^2 K_1(qa)}{n_1^2 qaK_0(qa)} = 0. \quad (\text{A.37})$$

For the EH_{lm} mode,

$$\frac{J_{l+1}(ha)}{haJ_l(ha)} - \left(\frac{n_1^2 + n_2^2}{2n_1^2} \right) \frac{K'_l(qa)}{qaK_l(qa)} - \frac{l}{(ha)^2} + R = 0. \quad (\text{A.38})$$

For the HE_{lm} mode,

$$\frac{J_{l+1}(ha)}{haJ_l(ha)} + \left(\frac{n_1^2 + n_2^2}{2n_1^2} \right) \frac{K'_l(qa)}{qaK_l(qa)} - \frac{l}{(ha)^2} + R = 0, \quad (\text{A.39})$$

where

$$R = \left[\left(\frac{n_1^2 - n_2^2}{2n_1^2} \right)^2 \left(\frac{K'_l(qa)}{qaK_l(qa)} \right)^2 + \left(\frac{l\beta}{n_1 k_0} \right)^2 \left(\frac{1}{q^2 a^2} + \frac{1}{h^2 a^2} \right)^2 \right]^{1/2}. \quad (\text{A.40})$$

A.2 Electric Field Equations

The electric field components for the fundamental mode are given as follows [199]. Outside the fibre (when $r < a$):

$$\begin{aligned}
 E_x &= -iS \frac{\beta}{2q} \frac{J_1(ha)}{K_1(qa)} \left[(1-s)K_0(hr) \cos \phi_0 - (1+s)K_2(hr) \cos (2\phi - \phi_0) \right] e^{i(\omega t - \beta z)}, \\
 E_y &= -iS \frac{\beta}{2q} \frac{J_1(ha)}{K_1(qa)} \left[(1-s)K_0(hr) \sin \phi_0 - (1+s)K_2(hr) \sin (2\phi - \phi_0) \right] e^{i(\omega t - \beta z)}, \\
 E_z &= S \frac{J_1(ha)}{K_1(qa)} K_1(qr) \cos (\phi - \phi_0) e^{i(\omega t - \beta z)},
 \end{aligned} \tag{A.41}$$

and when $r > a$, *i.e.* inside the fibre

$$\begin{aligned}
 E_x &= -iS \frac{\beta}{2h} \left[(1-s)J_0(hr) \cos \phi_0 - (1+s)J_2(hr) \cos (2\phi - \phi_0) \right] e^{i(\omega t - \beta z)}, \\
 E_y &= -iS \frac{\beta}{2h} \left[(1-s)J_0(hr) \sin \phi_0 - (1+s)J_2(hr) \sin (2\phi - \phi_0) \right] e^{i(\omega t - \beta z)}, \\
 E_z &= S J_1(qr) \cos (\phi - \phi_0) e^{i(\omega t - \beta z)}.
 \end{aligned} \tag{A.42}$$

The coefficient S is a normalisation constant. The angle ϕ_0 determines the orientation of the polarisation of the field and $s = \left(\frac{1}{h^2 a^2} + \frac{1}{q^2 a^2} \right) / \left(\frac{J_1'(ha)}{ha J_1(ha)} + \frac{K_1'(qa)}{qa K_1(qa)} \right)$. For a typical nanofibre with radius 200 nm, the parameter $qa = 0.486$ is small. The terms $K_1(qa)$ and $K_2(qa)$ become significant. This leads to a considerable E_z component and azimuthal dependence of the E_x and E_y components.

Appendix B

Other Published Works

B.1 Observation of the ^{87}Rb $5\text{S}_{1/2}$ to $4\text{D}_{3/2}$ Electric Quadrupole Transition at 516.6 nm Mediated via an Optical Nanofibre

Abstract

Light guided by an optical nanofibre has a very steep evanescent field gradient extending from the fibre surface. This gradient can be exploited to drive electric quadrupole transitions in nearby quantum emitters. In this paper, we report on the observation of the $5\text{S}_{1/2} \rightarrow 4\text{D}_{3/2}$ electric quadrupole transition at 516.6 nm (in vacuum) in laser-cooled ^{87}Rb atoms using only a few μW of laser power propagating through an optical nanofibre embedded in the atom cloud. This work extends the range of applications for optical nanofibres in atomic physics to include more fundamental tests such as high-precision measurements of parity non-conservation.

Contribution: K.P. Subramonian Rajasree contributed to building and maintaining the MOT-ONF system used for the experiments and provided feedback on the manuscript.

FAST TRACK COMMUNICATION • OPEN ACCESS

Observation of the ^{87}Rb $5\text{S}_{1/2}$ to $4\text{D}_{3/2}$ electric quadrupole transition at 516.6 nm mediated via an optical nanofibre

To cite this article: Tridib Ray *et al* 2020 *New J. Phys.* **22** 062001

View the [article online](#) for updates and enhancements.

**FAST TRACK COMMUNICATION****Observation of the ^{87}Rb $5S_{1/2}$ to $4D_{3/2}$ electric quadrupole transition at 516.6 nm mediated via an optical nanofibre****OPEN ACCESS**RECEIVED
6 February 2020REVISED
14 March 2020ACCEPTED FOR PUBLICATION
23 March 2020PUBLISHED
15 June 2020

Original content from
this work may be used
under the terms of the
[Creative Commons
Attribution 4.0 licence](#).

Any further distribution
of this work must
maintain attribution to
the author(s) and the
title of the work, journal
citation and DOI.

Tridib Ray^{1,3}, Ratnesh K Gupta¹, Vandna Gokhroo¹, Jesse L Everett¹ ,
Thomas Nieddu^{1,3}, Krishnapriya S Rajasree¹ and Sile Nic Chormaic^{1,2,4} ¹ Light-Matter Interactions for Quantum Technologies Unit, Okinawa Institute of Science and Technology Graduate University, Onna, Okinawa 904-0495, Japan² Université Grenoble Alpes, CNRS, Grenoble INP, Institut Néel, 38000 Grenoble, France³ Present address: Laboratoire Kastler Brossel, Sorbonne Université, CNRS, ENS-Université PSL, Collège de France, 4 place Jussieu, 75005 Paris, France.⁴ Author to whom any correspondence should be addressed.E-mail: sile.nicchormaic@oist.jp**Keywords:** optical nanofibre, electric quadrupole, rubidium, cold atoms**Abstract**

Light guided by an optical nanofibre has a very steep evanescent field gradient extending from the fibre surface. This gradient can be exploited to drive electric quadrupole transitions in nearby quantum emitters. In this paper, we report on the observation of the $5S_{1/2} \rightarrow 4D_{3/2}$ electric quadrupole transition at 516.6 nm (in vacuum) in laser-cooled ^{87}Rb atoms using only a few μW of laser power propagating through an optical nanofibre embedded in the atom cloud. This work extends the range of applications for optical nanofibres in atomic physics to include more fundamental tests such as high-precision measurements of parity non-conservation.

1. Introduction

The simplest and generally the strongest interaction between electromagnetic waves and matter is the electric dipole (E1) interaction—the first radiating term in a multipole expansion. Naturally, optical excitations mostly exploit E1 allowed transitions [1], such as the cooling transition for alkali atoms. The commonly used selection rules for atomic transitions are based on the electric dipole approximation and the effect of the higher order terms are frequently neglected, leading to what are known as dipole forbidden transitions. The strength of the optical transitions can be defined in terms of several different parameters, such as the Einstein A and B coefficients, the dipole moments, or the oscillator strengths (i.e. the f values) [2]. The electric dipole Rabi frequency, which defines the actual number of transitions that take place per second in the two-level system, is linearly proportional to the electric dipole moment and the amplitude of the light field. The corresponding E1 oscillator strengths (i.e. the f values) are proportional to the square of the dipole moment and, hence, the square of the E1 Rabi frequency.

The next term in the multipole expansion is the electric quadrupole (E2). Quadrupole transitions play an important role in atomic and molecular spectroscopy [3–5] with relevance in photochemistry, atmospheric physics, and fundamental processes [6], to name just a few. The E2 Rabi frequency is linearly proportional to the quadrupole moment and the gradient of the light field. Similarly to the E1 case, the oscillator strength for E2 transitions is proportional to the square of the E2 Rabi frequency. This implies that the electric quadrupole oscillator strengths also depend on the gradient of the electric field. Due to this dependency, E2 transitions are less studied than their E1 counterparts as it can be challenging to create a large enough field gradient experimentally. Note that the square of the quadrupole Rabi frequency is equivalently proportional to the E2 oscillator strength.

Several platforms for driving E2 transitions in the alkali atoms have been proposed and/or demonstrated, with recent particular focus on the $S \rightarrow D$ transitions since they may be useful for

high-precision measurements of parity non-conservation (PNC) [6] and could be used for an exchange of orbital angular momentum between light and the internal states of the atom [7, 8]. There are significant studies on the $6S_{1/2}$ to $5D_{5/2}$ transition in Cs at 685 nm using a variety of techniques including evanescent light fields from prism surfaces [5, 9], surface plasmons [10], and continuous wave (CW) free-space excitation [11], with proposals for using optical vortices [12], nano-edges [13], and plasmonics [10, 14].

Experiments in Rb have been more limited, with pulsed laser excitation of the $5S_{1/2}$ to the 4D levels at 516.5 nm [15, 16] and from the $5S_{1/2}$ to nD , where $n = 27 - 59$ Rydberg levels, using pulsed excitation at ~ 297 nm [17] being reported. Some works have also focussed on $n_1^2P \rightarrow n_2^2P$ electric quadrupole transitions in Rb by exploiting double resonances [18, 19]. However, for the reasons mentioned earlier, our focus is primarily on the $S \rightarrow D$ quadrupole transitions. The difficulty in exciting the $5S_{1/2} \rightarrow 4D$ transitions lies in the fact that the ratio of E1 to E2 transitions in the visible region is of the order of 10^7 , so aside from the desirability of a strong electric field gradient, sufficient laser intensity at ~ 516.6 nm is needed to drive the transition, with the cross-section for absorbing one photon being 1.4×10^{-17} cm² [15].

In this paper, we report on the experimental observation of the 516.6 nm (in vacuum) electric quadrupole transition in a cloud of laser-cooled ^{87}Rb atoms mediated by an optical nanofibre (ONF) using CW light. The rapid radial exponential decay of the 516.6 nm evanescent field from the surface of the ONF provides a very steep electric field gradient in the region of highest field intensity even for very low excitation laser powers, leading to relatively efficient excitation of the E2 transition. Additionally, optical nanofibres are quite easy to fabricate and integrate into magneto-optical traps or atomic vapour cells, as evidenced by the sheer volume of work in the last decade [20–31], negating the necessity for nanofabrication facilities as needed when using metamaterials or other such nanostructures.

2. Theoretical considerations

Recently, we theoretically investigated the enhancement of the $5S_{1/2} \rightarrow 4D_{5/2}$ quadrupole interaction for a ^{87}Rb atom in the evanescent field of an optical nanofibre [8]. We proposed that, while the E2 Rabi frequency reduces rapidly with radial distance from the fibre, the E2 oscillator strength enhancement is still significant even at appreciable distances from the nanofibre surface. In reference [8], the oscillator strength enhancement was expressed in terms of an *enhancement factor*, η_{osc} , which is the ratio of the oscillator strength of a fibre-guided field to the oscillator strength defined for a free-space, plane wave field with equal intensity. The enhancement depends on the wavelength and the fibre geometry, not the transition itself. Following the methods from reference [8], here we consider a different E2 excitation in ^{87}Rb , namely the $5S_{1/2} \rightarrow 4D_{3/2}$ transition. We focus on this transition due to technical issues related to photon detection for the subsequent decay channels. In figure 1(a), η_{osc} is plotted as a function of atom position in the xy -plane (where we assume the fibre axis is along z and the axis for the quasilinearly polarised guided light is along x). Assuming light is guided in the fundamental fibre mode, HE_{11} , we find a maximum enhancement factor for the oscillator strength, $\eta_{\text{osc}} = 4.92$, for an atom located on the fibre surface and positioned along the x -axis. As the atom moves further from the fibre, the enhancement still exists as long it is positioned close to the x -axis. This enhancement factor is not easily measured experimentally since it is a comparison between the ONF-mediated quadrupole transition and that in free-space for a specific intensity at a single point; it does not account for the exponential decay of the evanescent field.

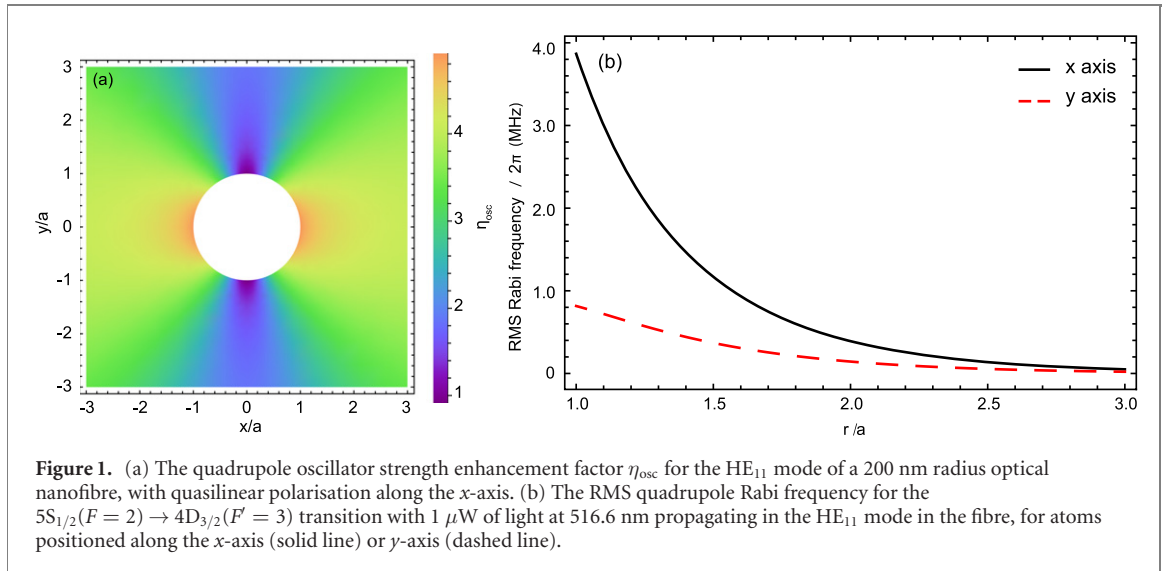
If we take the varying profile of the evanescent field into consideration, a far more experimentally useful and accessible parameter is the electric quadrupole Rabi frequency. Let us consider an alkali atom with ground state $|g\rangle = |nFM_F\rangle$ and excited state $|e\rangle = |n'F'M_{F'}\rangle$, where n is the principal quantum number, F is the total angular momentum quantum number of the atom and M_F is the magnetic quantum number. The quadrupole Rabi frequency, using Cartesian coordinates (x_1, x_2, x_3) , is given by [32]

$$\Omega_{FM_F F'M_{F'}} = \frac{1}{6\hbar} \sum_{ij} \langle n'F'M_{F'} | Q_{ij} | nFM_F \rangle \frac{\partial \mathcal{E}_j}{\partial x_i}, \quad (1)$$

where $i, j = 1, 2, 3$, the Q_{ij} are the quadrupole tensor components representing the strength of the quadrupole transition and the \mathcal{E}_j are the field components. The Q_{ij} are defined by [8]

$$Q_{ij} = q(3x_i x_j - R^2 \delta_{ij}). \quad (2)$$

Here, q is the electron charge, x_i is the i th coordinate of the valence electron of the atom and $R = \sqrt{x_1^2 + x_2^2 + x_3^2}$ is the distance from the valence electron to the centre-of-mass of the atom.



We now introduce a root-mean-square (RMS) quadrupole Rabi frequency, $\bar{\Omega}_{FF'}$, determined from equation (1) using

$$\bar{\Omega}_{FF'}^2 = \sum_{M_F M_{F'}} \left| \Omega_{FM_F F' M_{F'}} \right|^2, \quad (3)$$

where we sum over all the possible M_F values. In figure 1(b), we use analytical expressions for the evanescent field components based on the experimental fibre parameters and propagating power to plot $\bar{\Omega}_{FF'}$ as a function of an atom's position relative to the fibre, either along or perpendicular to the quasipolarisation axis. We choose $1 \mu\text{W}$ of resonant optical power (at 516.6 nm) in the fundamental mode, HE_{11} , of the nanofibre with quasilinear polarisation. We see that the RMS quadrupole Rabi frequency reduces dramatically as the atom moves away from the fibre surface.

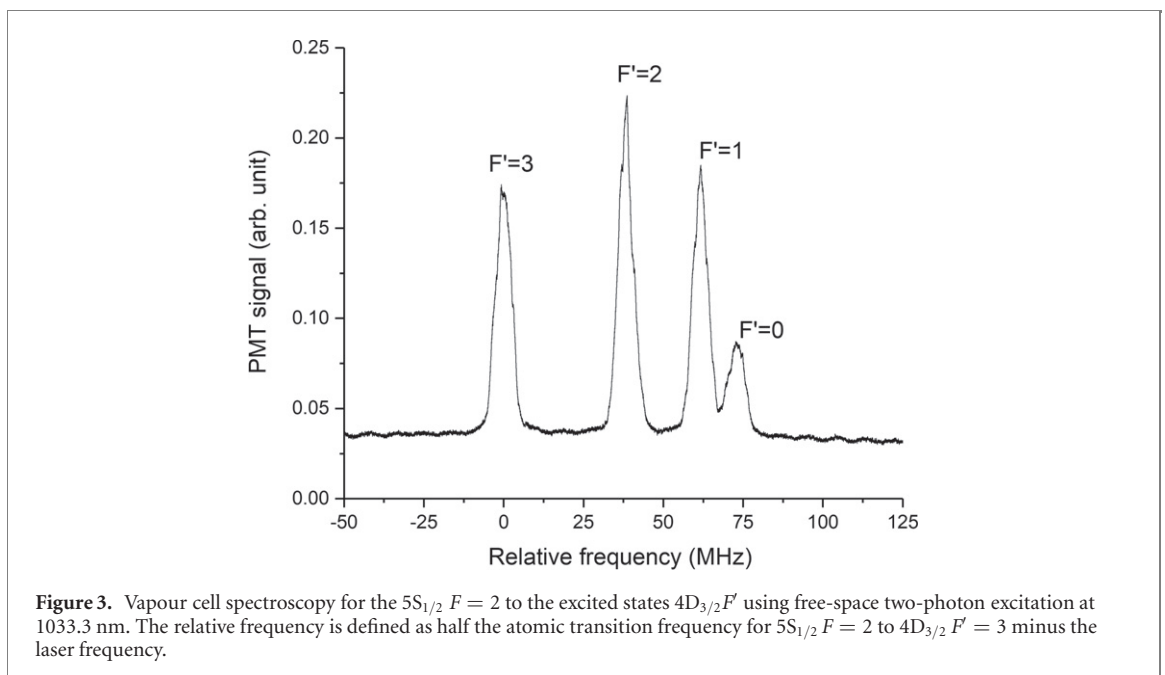
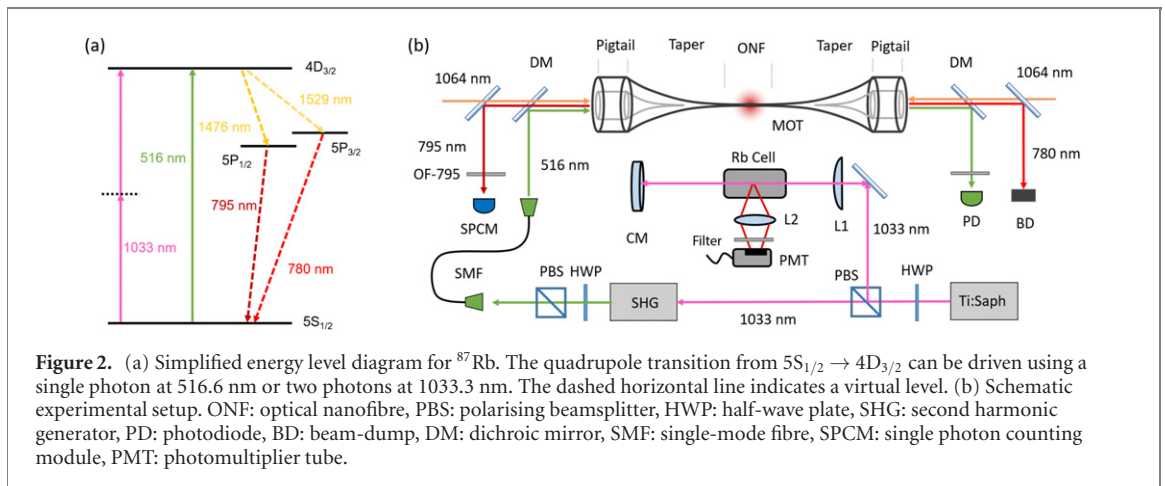
3. Experiments

In our experiment, we drive the $5S_{1/2} \rightarrow 4D_{3/2}$ E1 forbidden, E2 allowed optical transition in a cold atomic ensemble of ^{87}Rb , via the evanescent field of an optical nanofibre embedded in the atom cloud. The relevant energy level diagram is shown in figure 2(a) and a schematic of the experiment is given in figure 2(b). The E1 forbidden transition is excited using a single photon pathway at 516.6 nm derived from a frequency-doubled Ti: sapphire laser (M Squared Lasers Inc. SolsTiS and ECD-X second harmonic generator) set to 1033.3 nm. The 516.6 nm light from the second harmonic generator (SHG) is mode cleaned using a single-mode fibre and is coupled to one pigtail of the ONF using a pair of dichroic mirrors, see figure 2(b). Shortpass filters are placed after the SHG to remove any residual 1033.3 nm, which could lead to two-photon excitation of the transition of interest. We control the 516.6 nm power through the ONF using a half-wave plate combined with a polarising beam splitter (PBS) and neutral density filters (NDF).

Atoms excited to the $4D_{3/2}$ state can decay back to the ground state via two channels, see figure 2(a): (i) the $5P_{1/2}$ intermediate state, by cascaded emission of two photons at 1476 nm and 795 nm and (ii) the $5P_{3/2}$ intermediate state, by cascaded emission of two photons at 1529 nm and 780 nm [33, 34], which couple into the ONF and can be detected at the output pigtail. Detection of either of the emitted photon pairs would allow us to infer the electric quadrupole excitation. In this work, we detect the second step of decay path (i) at 795 nm due to the availability of single photon detectors (SPD) at near infrared (NIR) wavelengths and its spectral separability from the 780 nm photons scattered during the atom cooling process. The first step in the decay path at 1476 nm is undetected.

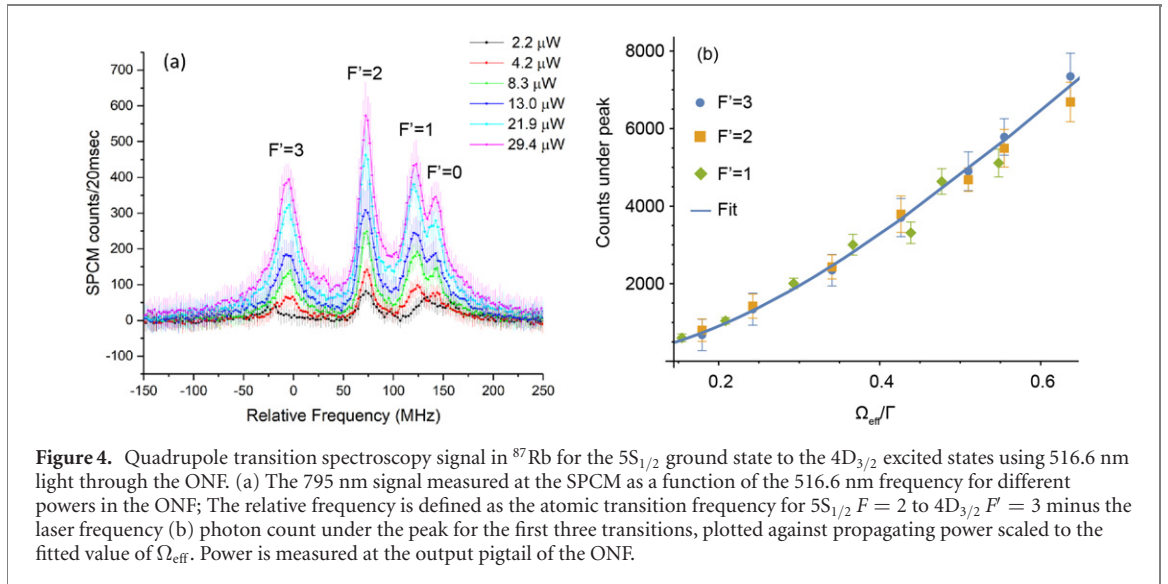
A frequency reference for the quadrupole transition is obtained using free-space, two-photon spectroscopy in a Rb vapour cell heated to 125°C [35]. We use the tightly focussed, 1033.3 nm direct output from the Ti-sapphire laser to drive the two-photon transition. The laser is scanned around 1033.3 nm such that atoms are excited to the $4D_{3/2}F'$ level. Figure 3 shows the two-photon spectroscopy signal for $5S_{1/2}F=2$ to $4D_{3/2}F'$. The four observed peaks correspond to the allowed transitions for the two-photon excitation at 1033.3 nm ($\Delta F \leq 2$) [36].

To study the quadrupole transition itself, we use ^{87}Rb atoms that are cooled and trapped in a conventional 3D magneto-optical trap (MOT) to a temperature of about $\sim 120 \mu\text{K}$. The cold atom cloud



has a Gaussian full width at half maximum (FWHM) of ~ 0.5 mm. We fabricate the ONF, which has a waist diameter of ~ 400 nm, by exponentially tapering a section of SM800-125 fibre using the flame-brushing method [37]. Further details of the MOT setup and the ONF can be found elsewhere [31]. The ONF has been optimised for 780 nm propagation and only $\sim 10\%$ of the 516.6 nm light (used to drive the E2 transition) as measured at the input to the ONF pigtail is detected at the output. We assume that most losses are at the down-taper as the adiabatic criterion is not satisfied for this wavelength. For wavelengths shorter than ~ 550 nm, the ONF supports several guided modes. Hence, for light at 516.6 nm, the ONF can support the fundamental, HE_{11} , mode and the first group of higher order modes, TE_{01} , TM_{01} , and $\text{HE}_{21,\text{eo}}$ [38]. We have seen elsewhere that, by coupling the HE_{11} mode into the input fibre pigtail to the ONF, the amount of coupling into the higher order modes is minimal [39, 40] and we, therefore, assume that the atoms only interact with the fundamental mode at the nanofibre waist. Note that, in all the following, when we refer to light power through the ONF, the values given are those measured at the output pigtail of the fibre and not at the nanofibre waist. This may be higher, due to both the aforementioned design criteria and, additionally, wavelength-specific material losses.

In addition to the fibre-guided light at 516.6 nm, we also inject a pair of 1064 nm counter-propagating beams into the fibre. This has several purposes. First, it keeps the ONF hot during the experiments, thus avoiding atom deposition on the fibre. Second, it attracts atoms towards the ONF surface due to the optical dipole force, thereby increasing the number of atoms in the evanescent field, resulting in larger photon signals.



4. Results and discussion

For a demonstration of the quadrupole excitation in the cold atom-ONF system, we study the $4D_{3/2}F'$ transition in detail. As mentioned, atoms can decay from $4D_{3/2}F'$ to $5S_{1/2}F$ via $5P_{1/2}$ emitting 795 nm photons. These emitted photons can be filtered efficiently from the 780 nm photons scattered from the trapping light leading to a relatively clean signal. The experiment is performed by scanning the Ti: sapphire laser frequency across the $4D_{3/2}F'$ transitions, see figure 2, and recording the 795 nm decay photons generated from the ONF-mediated E2 transition on a single photon counting module (SPCM). Simultaneously, we record the 1033.3 nm, two-photon spectroscopy signal from the vapour cell using a photomultiplier tube (PMT), see figure 2. Each experiment cycle is 10 s long, with 20 ms of bin time both for the SPCM and the PMT. Each data point is an average of 50 cycles. We can also detect the transmission of the 516.6 nm light through the fibre using a photodiode (PD) if desired.

As a first experiment, we studied the dependence of the 795 nm emission on the 516.6 nm power propagating through the ONF, see figure 4(a). The four observed peaks correspond to the electric quadrupole transitions, $\Delta F \leq 2$, and they are comparable to the observed two-photon dipole spectroscopy signal at 1033.3 nm in figure 3. Expected features, such as peak broadening and peak shifts due to the presence of the ONF, are visible in the spectra, with wide asymmetric tails which we attribute to the van der Waals interaction between the nanofibre and the atoms [41]. Due to the roughly exponential decay profile of the evanescent field, atoms experience a varying 516.6 nm intensity as they are excited to the $4D_{3/2}$ state. We ignore this and assume that the 795 nm emission into the fibre is produced by stationary atoms in a constant field with an effective quadrupole Rabi frequency Ω_{eff} . This frequency includes the oscillator strength $f_{F'}$ for each $F \rightarrow F'$ transition, so each F' level experiences a different Ω_{eff} for a specific propagating power in the fibre. We also ignore the pumping of atoms into particular M_F states by the cooling beams, as we expect this to be random and for the polarisation dependence to essentially average out over the length of the nanofibre. This allows us to equate the RMS quadrupole Rabi frequency with the experimentally measured quadrupole Rabi frequency.

From figure 4(a), we extract Ω_{eff} for each power by modelling each F' transition as a broadened Lorentzian. We integrate the photon counts for each transition, with bounds set manually. The $F' = 0$ transition is discarded due to the large overlap that it has with $F' = 1$. Using the area under the peak allows us to ignore the exact source of the broadening. The integrated photon count is then related to the effective Rabi frequency by $A \propto \Omega_{\text{eff}}^2 / \sqrt{\Gamma^2 + 2\Omega_{\text{eff}}^2}$, where $\Gamma/2\pi$ is the decay rate of the $4D_{3/2}$ state indirectly towards the ground state. In figure 4(b) we fit the data to find $\Omega_{\text{eff}} = (0.12 \pm 0.02)\Gamma$ for $1 \mu\text{W}$ of propagating power, with the data plotted directly against the fitted value. Ignoring intermediate state lifetimes and the effect of the nanofibre on E1 transition rates, the dipole decay from the $4D_{3/2}$ state gives $\Gamma/2\pi = 2.12 \text{ MHz}$, resulting in $\Omega_{\text{eff}}/2\pi = 250 \pm 50 \text{ kHz}$ for a power of $1 \mu\text{W}$ in the fibre. For comparison, the theoretically estimated value for the Rabi frequency (see figure 1(b)), averaged over the azimuthal angle, is about 250 kHz for $1 \mu\text{W}$ of propagating optical power, 200 nm from the fibre. Since there is good qualitative agreement between the value predicted by theory and that measured experimentally by our alternate

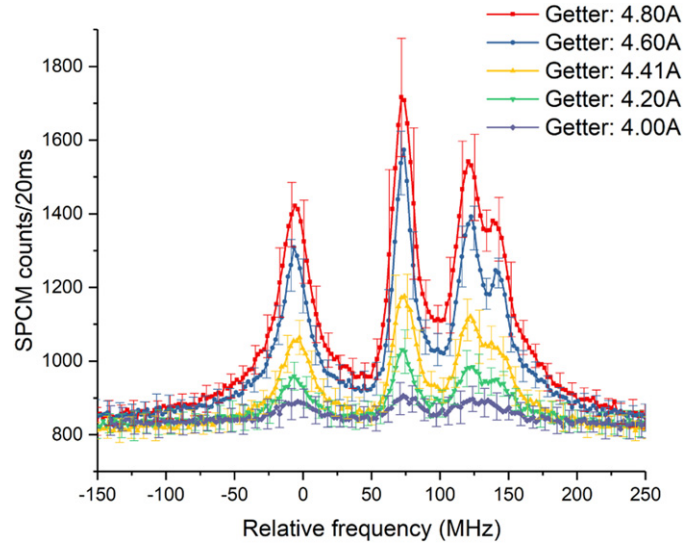


Figure 5. Quadrupole transition spectroscopy signal in ^{87}Rb for the $5S_{1/2}$ ground state to the $4D_{3/2}$ excited states using 516.6 nm light through the ONF showing the 795 nm signal as a function of the 516.6 nm frequency for different Rb getter currents. The peaks are the same as in figure 4. The relative frequency is defined as the atomic transition frequency for $5S_{1/2} F = 2$ to $4D_{3/2} F' = 3$ minus the laser frequency.

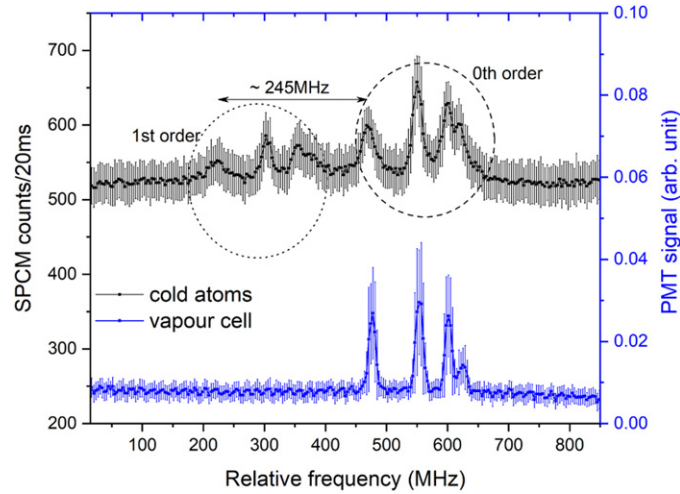


Figure 6. Spectroscopy signal in ^{87}Rb for the $5S_{1/2}$ ground state to the $4D_{3/2}$ excited state. Bottom: two-photon reference at 1033.3 nm in a vapour cell. Top: quadrupole excitation in cold atoms when the SHG output is passed through an AOM before being coupled to the ONF. The presence of the 1st order signal due to the AOM frequency shift, in the absence of a 2nd order signal, verifies the E2 excitation. The strong 0th order signal is due to inefficient coupling of light into the 1st order. Note that the frequency calibration on the x -axis is done with respect to 516.6 nm light.

method, we can conclude that the 516.6 nm power at the waist should correspond roughly to that measured at the output.

In a second experiment, we studied the dependence of the 795 nm emission on the getter current to the Rb source. Results are shown in figure 5. By assuming a Gaussian profile atom cloud around the ONF, we estimate that a getter current of 4.0 A (4.8 A) corresponds to a density of $\sim 6 \times 10^9$ (8×10^9) atoms/cm³. Note, however, that the cloud shape changes dramatically during these measurements and it is more accurate to consider the number of atoms in the trap increasing with getter current. In addition, the size of the atom cloud is increasing along the length of the nanofibre, leading to stronger photon signals.

As a verification that the transition is E2 driven, we used an acousto-optic modulator (AOM), with a central frequency $\omega_{\text{RF}} \sim 245$ MHz, to shift the frequency of the SHG output light. Here, light from the SHG at 516.6 nm and any residual light at 1033.3 nm passed through the AOM and the positive first-order was sent through the ONF. The frequency of the light with respect to the SHG output is shifted by ω_{RF} . If the atoms were excited via the E2 transition at 516.6 nm, the spectroscopy signal peaks should shift by ω_{RF} , whereas if excitation was via the two-photon transition by residual light at 1033.3 nm, the peaks should

shift by $2 \times \omega_{\text{RF}}$. Observations show, see figure 6, that the signal is shifted by ω_{RF} ; thence, the excitation is indeed via the quadrupole transition.

5. Conclusion

We have demonstrated an optical nanofibre-mediated electric quadrupole transition, $5S_{1/2}$ to $4D_{3/2}$, in ^{87}Rb at 516.6 nm [42], by recording fluorescence emissions at 795 nm. An important feature is that only a few μW of power were needed to drive the E2 transition. Even though the 1476 nm photon from the first step in the decay path is undetected in this work, it may be possible to indirectly determine the lifetime of the 4D level from the fluorescence distribution of the 795 nm step [43] since the lifetime of the $5P_{1/2}$ level is well-documented [44, 45]. This will be the focus of future work.

The $5S_{1/2} \rightarrow 4D_{X/2}$ transition in ^{87}Rb could be used to study parity-violating nuclear forces beyond the standard model with the accuracy in Rb expected to be higher than that for Cs [6, 46] or could be exploited for the transfer of orbital angular momentum of light to the internal degrees of freedom of an atom. A similar technique to the work presented here could be used to study the $4D_{5/2}$ transition; this decays to $5S_{1/2}$ along a single path via the $5P_{3/2}$ state with the emission of 1529 nm and 780 nm correlated photons. The challenge would be the detection of the 1529 nm photons to distinguish from the 780 nm cooling beams. The advantages would be that the oscillator strength of this transition for a free-space beam has already been measured experimentally [16] and a similar transition in Cs, i.e., the $6S_{1/2} \rightarrow 5D_{5/2}$ transition, has been studied in the evanescent field of a prism [5]. This work extends the use of optical nanofibres in atomic systems and could find applications in atomic clocks, lifetime measurements of atomic states, and in devising trapping schemes for neutral atoms.

Acknowledgments

This work was supported by Okinawa Institute of Science and Technology Graduate University and JSPS Grant-in-Aid for Scientific Research (C) Grant No. 19K05316. The authors wish to acknowledge F Le Kien for useful discussions, M Ozer and K Karlsson for technical support, and E Nakamura for research support.

ORCID iDs

Jesse L Everett  <https://orcid.org/0000-0002-6290-9354>

Sile Nic Chormaic  <https://orcid.org/0000-0003-4276-2014>

References

- [1] Demtröder W 2010 *Atoms, Molecules and Photons* (Berlin: Springer)
- [2] Hilborn R C 1982 *Am. J. Phys.* **50** 982–6
- [3] Sayer B, Wang R, Jeannot J C and Sassi M 1971 *J. Phys. B: At. Mol. Phys.* **4** L20–3
- [4] Camy-Peyret C, Flaud J M, Delbouille L, Roland G, Brault J W and Testerman L 1981 *J. Physique Lett.* **42** 279–83
- [5] Tojo S, Hasuo M and Fujimoto T 2004 *Phys. Rev. Lett.* **92** 053001
- [6] Roberts B M, Dzuba V A and Flambaum V V 2014 *Phys. Rev. A* **89** 012502
- [7] Babiker M, Bennett C R, Andrews D L and Dávila Romero L C 2002 *Phys. Rev. Lett.* **89** 143601
- [8] Le Kien F, Ray T, Nieddu T, Busch T and Nic Chormaic S 2018 *Phys. Rev. A* **97** 013821
- [9] Tojo S, Fujimoto T and Hasuo M 2005 *Phys. Rev. A* **71** 012507
- [10] Chan E A, Aljunid S A, Adamo G, Zheludev N I, Ducloy M and Wilkowski D 2019 *Phys. Rev. A* **99** 063801
- [11] Pucher S, Schneeweiss P, Rauschenbeutel A and Dareau A 2020 *Phys. Rev. A* **101** 042510
- [12] Lembessis V E and Babiker M 2013 *Phys. Rev. Lett.* **110** 083002
- [13] Shibata K, Tojo S and Bloch D 2017 *Opt. Express* **25** 9476
- [14] Sakai K, Yamamoto T and Sasaki K 2018 *Sci. Rep.* **8** 7746
- [15] Teppner U and Zimmermann P 1978 *Astron. Astrophys.* **64** 215–7
- [16] Nilsen J and Marling J 1978 *J. Quant. Spectrosc. Radiat. Transfer* **20** 327–9
- [17] Tong D, Farooqi S M, van Kempen E G M, Pavlovic Z, Stanojevic J, Côté R, Eyler E E and Gould P L 2009 *Phys. Rev. A* **79** 052509
- [18] Ponciano-Ojeda F *et al* 2015 *Phys. Rev. A* **92** 042511
- [19] Mojica-Casique C, Ponciano-Ojeda F, Hernández-Gómez S, López-Hernández O, Flores-Mijangos J, Ramírez-Martínez F, Sahagún D, Jáuregui R and Jiménez-Mier J 2016 *J. Phys. B: At. Mol. Opt. Phys.* **50** 025003
- [20] Hendrickson S M, Lai M M, Pittman T B and Franson J D 2010 *Phys. Rev. Lett.* **105** 173602
- [21] Vetsch E, Reitz D, Sagué G, Schmidt R, Dawkins S T and Rauschenbeutel A 2010 *Phys. Rev. Lett.* **104** 203603
- [22] Nayak K P, Das M, Le Kien F and Hakuta K 2012 *Opt. Commun.* **285** 4698–704
- [23] Lacroûte C, Choi K S, Goban A, Alton D J, Ding D, Stern N P and Kimble H J 2012 *New J. Phys.* **14** 023056
- [24] Kumar R, Gokhroo V and Nic Chormaic S 2015 *New J. Phys.* **17** 123012
- [25] Kumar R, Gokhroo V, Deasy K and Nic Chormaic S 2015 *Phys. Rev. A* **91** 053842

- [26] Sayrin C, Clausen C, Albrecht B, Schneeweiss P and Rauschenbeutel A 2015 *Optica* **2** 353–6
- [27] Kumar R, Gokhroo V, Tiwari V B and Nic Chormaic S 2016 *J. Opt.* **18** 115401
- [28] Ruddell S K, Webb K E, Herrera I, Parkins A S and Hoogerland M D 2017 *Optica* **4** 576–9
- [29] Béguin J B, Müller J, Appel J and Polzik E 2018 *Phys. Rev. X* **8** 031010
- [30] Kato S, Némethy N, Senga K, Mizukami S, Huang X, Parkins S and Aoki T 2019 *Nat. Commun.* **10** 1–6
- [31] Rajasree K S, Ray T, Karlsson K, Everett J L and Nic Chormaic S 2020 *Phys. Rev. Research* **2** 012038
- [32] Jackson J D 1999 *Classical Electrodynamics* 3rd edn (New York: Wiley)
- [33] Moon H S, Ryu H Y, Lee S H and Suh H S 2011 *Opt. Express* **19** 15855–63
- [34] Roy R, Condylis P C, Johnathan Y J and Hessmo B 2017 *Opt. Express* **25** 7960–9
- [35] Nieddu T, Ray T, Rajasree K S, Roy R and Nic Chormaic S 2019 *Opt. Express* **27** 6528–35
- [36] Salour M 1978 *Ann. Phys.* **111** 364–503
- [37] Ward J M, Maimaiti A, Le V H and Nic Chormaic S 2014 *Rev. Sci. Instrum.* **85** 111501
- [38] Frawley M C, Petcu-Colan A, Truong V G and Nic Chormaic S 2012 *Opt. Commun.* **285** 4648–54
- [39] Nieddu T 2019 Optical nanofibers for multiphoton processes and selective mode interactions with rubidium *PhD Thesis* Okinawa Institute of Science and Technology Graduate University
- [40] Mekhail S P 2019 Optical fiber probes for in-vivo neuronal compressive microendoscopy and mode analysis in nanofibers *PhD Thesis* Okinawa Institute of Science and Technology Graduate University
- [41] Minogin V and Chormaic S N 2010 *Laser Phys.* **20** 32–7
- [42] Safronova M S and Safronova U I 2011 *Phys. Rev. A* **83** 052508
- [43] Gomez E, Baumer F, Lange A D, Sprouse G D and Orozco L A 2005 *Phys. Rev. A* **72** 012502
- [44] Simsarian J E, Orozco L A, Sprouse G D and Zhao W Z 1998 *Phys. Rev. A* **57** 2448–58
- [45] Gutterres R F, Amiot C, Fioretti A, Gabbanini C, Mazzoni M and Dulieu O 2002 *Phys. Rev. A* **66** 024502
- [46] Dzuba V A, Flambaum V V and Roberts B 2012 *Phys. Rev. A* **86** 062512

B.2 Simple, Narrow and Robust Atomic Frequency Reference at 993 nm Exploiting the Rubidium (Rb) $5S_{1/2}$ to $6S_{1/2}$ Transition using One-Color, Two-Photon Excitation

Abstract

We experimentally demonstrate a one-color two-photon transition from the $5S_{1/2}$ ground state to the $6S_{1/2}$ excited state in rubidium (Rb) vapor using a continuous wave laser at 993 nm. The Rb vapor contains both isotopes (^{85}Rb and ^{87}Rb) in their natural abundances. The electric dipole allowed transitions are characterized by varying the power and polarization of the excitation laser. Since the optical setup is relatively simple, and the energies of the allowed levels are impervious to stray magnetic fields, this is an attractive choice for a frequency reference at 993 nm, with possible applications in precision measurements and quantum information processing.

Contribution: K.P. Subramonian Rajasree contributed to the initial experimental design and participated in the discussions and paper writing.



Simple, narrow, and robust atomic frequency reference at 993 nm exploiting the rubidium (Rb) $5S_{1/2}$ to $6S_{1/2}$ transition using one-color two-photon excitation

T. NIEDDU,¹ T. RAY,¹ K. S. RAJASREE,¹ R. ROY,^{2,*} AND S. NIC CHORMAIC^{1,3,4}

¹Light-Matter Interactions Unit, Okinawa Institute of Science and Technology Graduate University, Onna, Okinawa 904-0495, Japan

²Quantum Systems & Devices Group, School of Mathematical and Physical Sciences, Pevensey II, University of Sussex, Falmer, Brighton BN1 9QH, UK

³Université Grenoble Alpes, CNRS, Grenoble INP, Institut Néel, 38000 Grenoble, France

⁴School of Chemistry and Physics, University of KwaZulu-Natal, Durban 4001, South Africa
*ritayan.roy@u.nus.edu

Abstract: We experimentally demonstrate a one-color two-photon transition from the $5S_{1/2}$ ground state to the $6S_{1/2}$ excited state in rubidium (Rb) vapor using a continuous wave laser at 993 nm. The Rb vapor contains both isotopes (^{85}Rb and ^{87}Rb) in their natural abundances. The electric dipole-allowed transitions are characterized by varying the power and polarization of the excitation laser. Since the optical setup is relatively simple, and the energies of the allowed levels are impervious to stray magnetic fields, this is an attractive choice for a frequency reference at 993 nm, with possible applications in precision measurements and quantum information processing.

© 2019 Optical Society of America under the terms of the [OSA Open Access Publishing Agreement](#)

1. Introduction

Two-photon processes in atomic systems have several distinct advantages over single-photon processes. For example, two-photon processes can give direct access to optical excitations that would be electric-dipole forbidden for a single-photon process [1]. Furthermore, when the two photons are derived from two laser beams in a counter-propagating configuration, a judicious choice of the polarizations can yield background-less, Doppler-free spectra [2, 3]. In addition, two-photon transition frequencies for nS to mS transitions, with n and m the principal quantum numbers of the ground and excited states, respectively, are insensitive to magnetic fields below the Paschen-Back domain [4, 5], while two-photon transitions to metastable states have extremely narrow linewidths compared to those for single-photon processes [6, 7]. These unique features make two-photon spectroscopy a powerful tool for precision measurements. Following the first observation of a two-photon transition in an atomic system containing cesium [8], numerous different atomic transitions have been investigated [9–15]. The technique has been extensively used for metrology and the accurate determination of fundamental constants [16, 17], as a frequency reference [18], and in quantum telecommunications [19].

In this paper, we report on the observation and spectroscopic study of the $5S_{1/2}$ to $6S_{1/2}$ two-photon transition in a hot Rb-atom vapor using a single-frequency laser beam. To our knowledge, this is the first observation of this particular Rb transition using a one-color two-photon excitation. We explore the dependency of the spectroscopy signal on (i) the intensity and (ii) the polarization of the pump beam. Observation of a quadratic dependency on the intensity of the pump laser is a signature of the two-photon transition. We also show that the pump laser frequency can be stabilized to the observed spectroscopic peaks, thereby illustrating that the transition can

be used as a frequency reference. Finally, we discuss some possible applications for precision measurements and quantum telecommunications.

2. Experimental details

The energy level diagram for the Rb transition of interest is shown in Fig. 1. Atoms are excited from the $5S_{1/2}$ ground state via a virtual state to the $6S_{1/2}$ state using a two-photon process at 993 nm. The atoms can decay back to the ground state via two possible channels characterized by an intermediate state, which can be either (i) the $5P_{1/2}$ level on emission of a pair of photons with wavelengths of 1324 nm and 795 nm (i.e. the D1 transition), or (ii) the $5P_{3/2}$ level on emission of a pair of photons with wavelengths of 1367 nm and 780 nm (i.e. the D2 transition). The photons at 1324 nm and 1367 nm fall beyond the range of the detectors available for this experiment, hence, for the work reported hereafter, we only detect the 780 nm and 795 nm light.

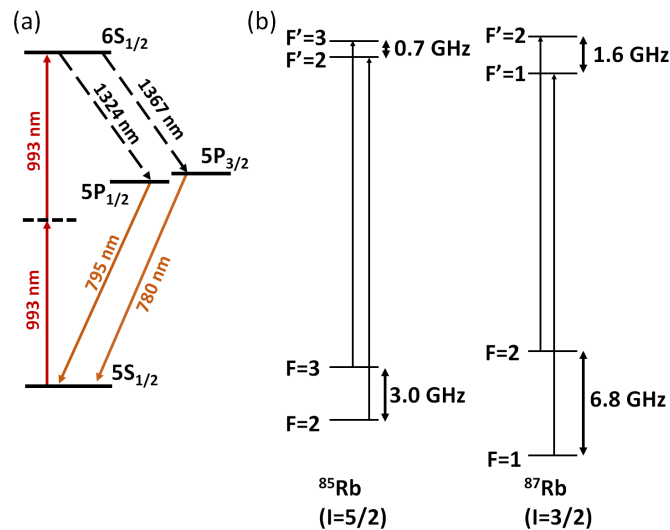


Fig. 1. (a) Energy level diagram for Rb. A beam at 993 nm excites atoms from $5S_{1/2}$ to $6S_{1/2}$ via single-color two-photon excitation. The intermediate virtual state is represented as a dashed line. The atoms decay back to the $5S_{1/2}$ level via the $5P_{1/2}$ or $5P_{3/2}$ levels, with photons emitted at 795 nm and 780 nm (orange arrows); (b) Hyperfine level diagrams for the two Rb isotopes. Two-photon transitions allowed by the selection rule, $\Delta F = 0$, $\Delta m_F = 0$, are shown, along with the frequencies of the hyperfine splittings.

The experimental setup is illustrated in Fig. 2. The experiment is carried out in a glass cell filled with Rb in its natural isotopic abundances, maintained at a temperature of 130 °C. The 993 nm beam used to drive the two-photon transition is provided by a continuous wave (CW) Ti:Sapphire laser (Coherent MBR 110), locked to a scanning reference cavity yielding a spectral linewidth of 100 kHz. The laser frequency can be scanned by changing the length of the reference cavity. The combination of a half-wave plate (HWP) and a polarizing beam-splitter (PBS) at the output of the laser allows us to control the powers in the reflected (R) and transmitted (T) beams from the PBS. Most of the optical power, typically >90%, is in T and passes through the vapor cell for the two-photon spectroscopy studies. The remaining light, in R, is fiber-coupled and further split so that 99% goes to a Fabry-Pérot cavity (Toptica FPI-100) and 1% to a wavemeter (HighFinesse WS-6). The wavemeter has two purposes; it allows us to tune the laser to the desired wavelength and to monitor the frequency scanning. The Fabry-Pérot cavity has a free-spectral

range of 1 GHz and is used to monitor the linearity of the frequency scan.

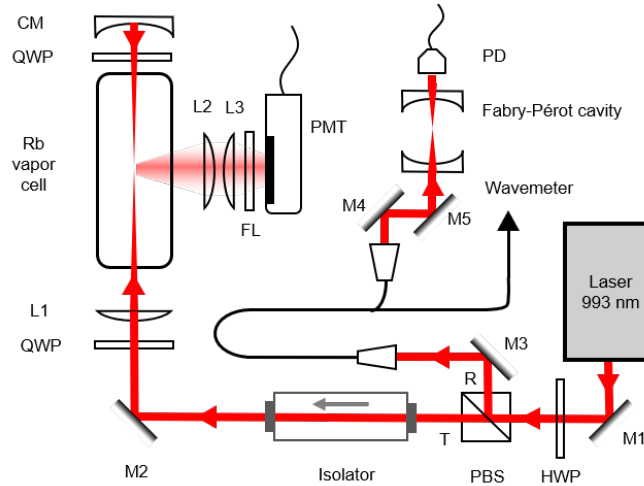


Fig. 2. Schematic of the experimental setup. Light from a tunable 993 nm laser is used for two-photon excitation in a Rb vapor cell using a retro-reflected configuration. The resulting atomic fluorescence is detected by a PMT. The polarizations of the forward and retro-reflected beams are controlled using QWPs. A small amount (i.e. <10%) of the 993 nm beam is coupled to a Fabry-Pérot cavity and a wavemeter to monitor the laser frequency. M1-M5: Mirrors, L1-L3 Plano-convex lens, HWP: Half-wave plate, QWP: Quarter-wave plate, PBS: Polarizing beam splitter, CM: Concave mirror, PMT: Photomultiplier tube, FL: Short-pass optical filter, PD: Photodiode.

An optical isolator is placed before the vapor cell to avoid reflections back into the laser. A plano-convex lens (L1), with focal length $f_1 = 150$ mm, is placed after the optical isolator to focus the beam in the cell. The $1/e^2$ beam diameter is $128 \mu\text{m}$. A concave mirror (CM), with focal length $f_{CM} = 75$ mm, and placed $2f_{CM} = 150$ mm away from the focal plane of L1 ensures retro-reflection of the beam back to the focal point. Quarter-wave plates (QWP) can be inserted in the beam path before L1 and CM to generate a circularly polarized beam. We detect both the 795 nm and 780 nm decay photons using a photomultiplier tube (PMT) (Hamamatsu R636-10). A short-pass filter with a cut-off wavelength of 800 nm is placed in front of the PMT to prevent any scattered light from the 993 nm pump from being detected. We use a pair of lenses, L2 and L3, with focal lengths of $f_2 = f_3 = 50$ mm, in front of the PMT in a telescope configuration for efficient collection of the light. The quantum efficiencies of the PMT at 780 nm and 795 nm are 9% and 8%, respectively. The obtained current is amplified by a pre-amplifier with a gain of 10^5 and dropped across a 50Ω resistor on an oscilloscope.

3. Results

Electric dipole forbidden (single-photon) nS to mS transitions, accessible via two-photon excitation, obey the selection rules $\Delta F = 0$ and $\Delta m_F = 0$ [20]. This results in only two allowed transitions for each Rb isotope, i.e. $^{87}\text{Rb } F = 2 - F' = 2$, $^{85}\text{Rb } F = 3 - F' = 3$, $^{85}\text{Rb } F = 2 - F' = 2$, and $^{87}\text{Rb } F = 1 - F' = 1$ (see Fig. 1(b)). A typical spectrum obtained is shown in Fig. 3(a). Here, excitation to the $6S_{1/2}$ level is obtained by scanning the frequency of the 993 nm laser and using the same linear polarization for the forward and retro-reflected beams that generate the two-photon process. Note that the simple setup presented here does not measure the absolute frequency of the transition. The hyperfine splitting of the $6S_{1/2}$ level is obtained

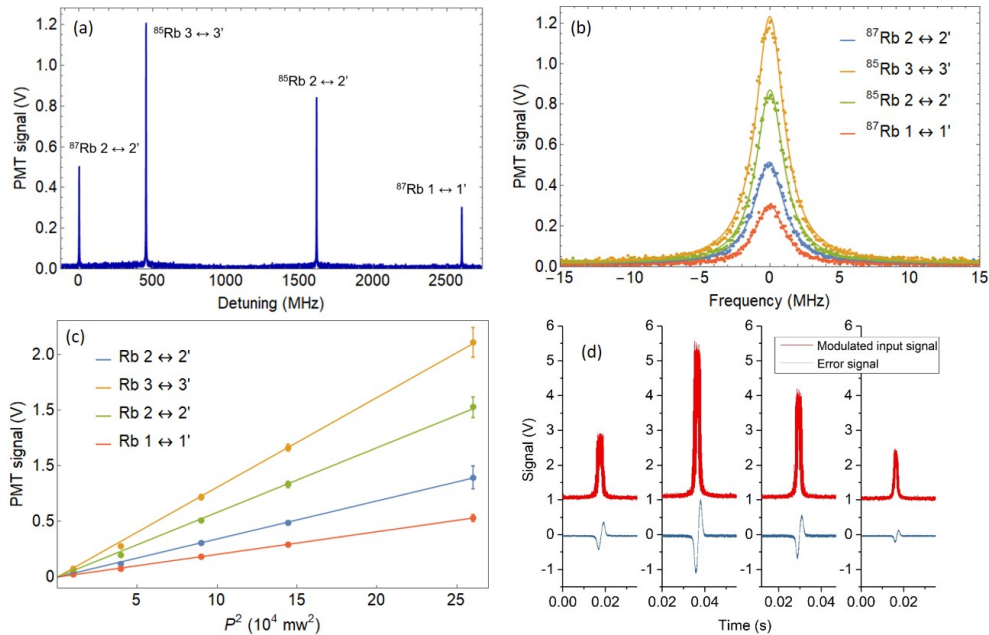


Fig. 3. (a) Typical spectroscopic signal obtained by scanning the frequency of the 993 nm pump beam and recording the signal on the PMT. Each peak indicates a hyperfine transition as labeled. (b) Comparison of the individual peak intensities and linewidths from (a). (c) Linear dependence of the peak height as a function of the total pump power (P) squared. (d) Modulated signals and the generated error signals for each peak to which the laser can be locked. For clarity, a 1 V offset is added to the modulated signal.

from Ref. [21] using a resonant intermediate level. The relative frequency difference is obtained by setting the frequency of the first peak, i.e. the $^{87}\text{Rb } 5S_{1/2}, F = 2 - 6S_{1/2}, F' = 2$ transition, to zero, see Fig. 3(a). A linear frequency scaling obtained by using fringe interpolation of the Fabry-Pérot peaks, which are 1 GHz apart, yields a similar result. Due to the two-photon process, the relative frequency differences of the peaks are half the actual energy differences of the atomic levels.

3.1. Power variation

The relative height and width of each peak in Fig. 3(a) is shown in Fig. 3(b). For a particular Rb isotope, the intensities of the transitions from the ground hyperfine levels are proportional to the statistical weights of the atomic population in those hyperfine levels [22]. However, since the difference in energy between the hyperfine levels is negligible compared to the transition energy, the weight factor is equivalent to the degeneracy ($2F + 1$) of the hyperfine levels. These values are 5 : 3 and 7 : 5 for ^{87}Rb and ^{85}Rb , respectively. The variation of peak height as a function of the square of the laser power is shown in Fig. 3(c). The peak heights show a quadratic dependence on the total beam power, P (i.e. the sum of the powers in the forward and retro-reflected beams); this is a signature of the two-photon process [23]. The ratios of the slopes of the fitted straight lines are 1.667 for ^{87}Rb and 1.387 for ^{85}Rb , i.e., close to the expected ratios of 5 : 3 and 7 : 5, respectively. The width of the peaks does not change as a function of power, at least within the standard deviation of the measurements. We measure a Lorentzian full-width-at-half-maximum (FWHM) of 2.60 ± 0.07 MHz, 2.44 ± 0.09 MHz, 2.49 ± 0.04 MHz and 2.43 ± 0.04 MHz for

$^{87}\text{Rb } F = 2 - F' = 2$, $^{87}\text{Rb } F = 1 - F' = 1$, $^{85}\text{Rb } F = 3 - F' = 3$ and $^{85}\text{Rb } F = 2 - F' = 2$ peaks, respectively.

3.2. Laser frequency stabilization to spectroscopic peaks

To establish the viability of the transition as a frequency reference, we demonstrate frequency locking of the pump laser to the spectroscopic peaks. This is implemented by integrating a TEM LaseLock module with the Ti:Sapphire laser. First, the reference cavity is bypassed and the laser frequency is scanned by directly scanning its cavity. A 10 kHz modulation is applied to one of the piezo-driven mirrors to generate frequency sidebands. The modulated spectroscopic signal is fed into a lock-in amplifier and an error signal is generated. An example of a modulated signal and a derived error signal are shown in Fig. 3(d). The laser cavity and, hence, the frequency can be stabilized to each of these error signals.

3.3. Polarization variation

We next explore the effect of changing the polarization of the counter-propagating beams on the spectroscopic signal. As shown in Fig. 2, a quarter-wave plate at either end of the vapor cell can be used to generate identical, or orthogonal, circularly polarized forward and retro-reflected beams. Let us denote linear and circular polarizations as π and σ , respectively, and their orthogonal polarizations as π' and σ' , respectively. As mentioned, the two-photon transition selection rules between the S levels are $\Delta F = 0$ and $\Delta m_F = 0$, hence the total angular momentum of two photons absorbed by an atom during the excitation process must be zero.

First we study the case of linear polarizations. By blocking the retro-reflected beam, a π configuration is created, see Fig. 4(a). We observe a Doppler-broadened signal since both photons are derived from the forward beam. Next, by introducing a retro-reflected beam, a $\pi - \pi$ configuration is created, see Fig. 4(b). Here, we obtain a narrow Doppler-free spectrum on top of a small Doppler-broadened baseline. The Doppler-free spectrum arises when the two photons are absorbed from counter-propagating beams, whereas the Doppler-broadened signal results from the two photons being absorbed from the same (forward or retro-reflected) beam. Next, the addition of a QWP after the vapor cell, aligned at 45° with respect to the forward beam's polarization axis, creates a linearly polarized, retro-reflected beam, orthogonal to the forward beam, resulting in a $\pi - \pi'$ configuration, see Fig. 4(c). In this case, the two photons can only be absorbed from either the forward or the retro-reflected beam, i.e., they cannot be absorbed simultaneously from both beams. This results in a signal on the PMT that is the sum of two Doppler-broadened spectra, one from each beam, yielding double the amplitude of the π configuration.

We next move to the case where the beams have circular polarizations. By inserting a QWP at 45° before the vapor cell and blocking the retro-reflected beam, a σ configuration (see Fig. 4(d)) is created. In this case, the transition is forbidden (the sum of the angular momenta of two photons in the forward beam is non-zero), hence there is no signal recorded on the PMT. The $\sigma - \sigma$ configuration (see Fig. 4(e)) is created by allowing the retro-reflected beam to propagate inside the vapor cell. This transition is also forbidden as, once more, the sum of the angular momenta of the two photons from the counter-propagating beams ($2\hbar$) is non-zero; as a result there is no signal. Finally, inserting a QWP before the retro-reflecting mirror forms a $\sigma - \sigma'$ configuration. The orientation of the waveplate's axis is irrelevant. The two photons that drive the transition can only be absorbed from the counter-propagating beams. As a result, a background-less, Doppler-free spectrum is obtained (see Fig. 4(f)). The peak heights are half those obtained for the $\pi - \pi$ configuration as the probability to absorb two-photons with opposite spin angular momentum is lesser in this case. It should be noted that the other orthogonal circular polarization configuration yields a similar result and is not presented here.

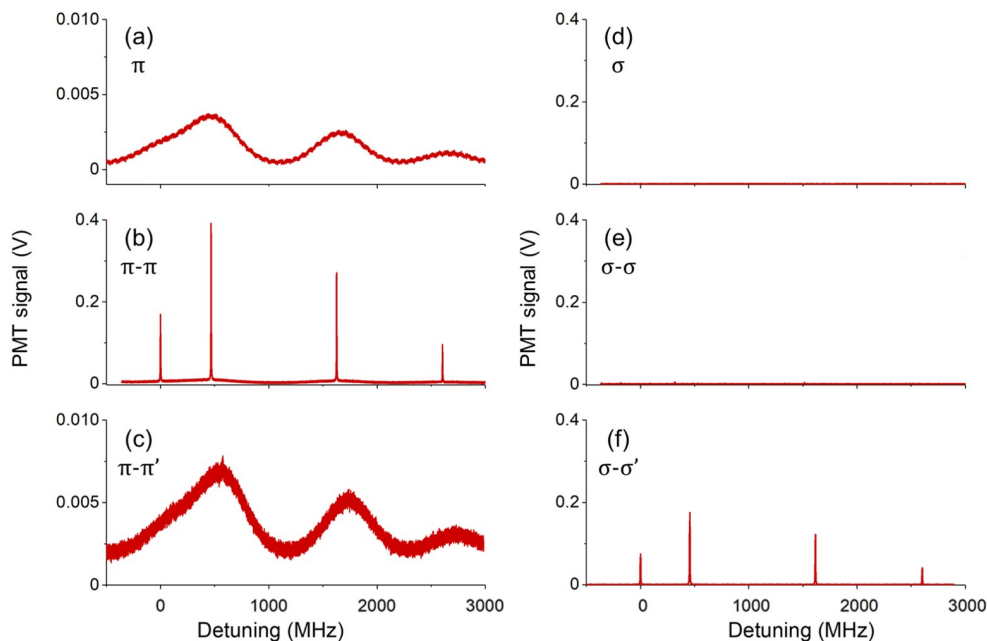


Fig. 4. Effect of beam polarization on the two-photon excitation as recorded by the PMT. As in Fig. 3(a), the relative frequency is obtained by setting the frequency of the $5S_{1/2}, F = 2 - 6S_{1/2}, F' = 2$ peak to zero. The power of the 993 nm beam is fixed at 250 mW and its frequency is scanned. The polarization of the beam is changed using QWPs. (a) Doppler-broadened spectrum with a single, linearly polarized beam. (b) Linearly polarized counter-propagating beams reveal the Doppler-free peaks and a small Doppler-broadened base. (c) Counter-propagating beams with orthogonal linear polarizations yield a Doppler-broadened spectrum of twice the amplitude of that in (a). (d) A single, circularly polarized beam does not yield a signal. This configuration is forbidden, according to the selection rules. (e) Counter-propagating beams with identical circular polarizations do not yield a signal for the same reason as in (d). (f) Counter-propagating beams with orthogonal circular polarizations yield a background-less Doppler-free spectrum. Here, the total angular momentum for the transition is zero.

4. Discussion

Ab-initio calculations of the electronic wavefunction close to the nucleus rely on an accurate measurement of the hyperfine splitting of the atomic energy level [24]. To date, the $6S_{1/2}$ level in Rb has been accessed via a two-color, two-photon excitation scheme at 795 nm and 1324 nm for measuring its lifetime [21] and hyperfine splitting [25]. Accessing the $6S_{1/2}$ level via the one-color, two-photon method presented here should enhance the accuracy and precision of such measurements since only a single laser is necessary for the excitation. Additionally, the two-photon transition could be used for the measurement of parity nonconservation [26, 27] in alkali atoms.

The excitation scheme presented herein enables the conversion of two near-infrared photons at 993 nm into a telecommunication O-band photon, at either 1324 nm or 1367 nm, and another near-infrared photon, at 795 nm or 780 nm, respectively. Chanielière *et al.* [19] proposed a method for building quantum repeaters using cascaded atomic transitions, whereas Willis *et al.* [28] generated time-correlated photon-pairs between a near-infrared photon and an O-band photon

using a four-wave mixing (4WM) process in a Rb vapor. The 4WM scheme made use of the $6S_{1/2}$ level, accessed via a two-color, two-photon excitation. Our scheme is compatible with these results, as driving the $5S_{1/2}$ to $6S_{1/2}$ two-photon transition would permit us to exploit both O-band photons as signal photons, and the corresponding NIR photons as idlers mapped onto an atomic quantum memory. In particular, the 993 nm photons could be coupled to atoms interacting with the evanescent field at the waist of an optical nanofiber embedded in a cold atomic ensemble [29] to make the process more efficient [30].

The first order Zeeman shifts experienced by the same hyperfine states of the $5S_{1/2}$ and $6S_{1/2}$ levels are identical since they have the same hyperfine Landé g -factors. This feature renders the frequency of the $5S_{1/2}$ to $6S_{1/2}$ transition insensitive to stray magnetic fields. The transition frequency is also less sensitive to electric fields compared to transitions to nonzero angular momentum states (where $l > 0$). These features makes the transition an attractive choice for a frequency reference.

5. Conclusion

We have demonstrated the $5S_{1/2}$ to $6S_{1/2}$ one-color, two-photon transition in a hot Rb vapor. The effects of excitation laser power and beam polarization on the observed spectroscopy signals were investigated. We also propose that the transition can be used as a reference at 993 nm by demonstrating frequency stabilization of the excitation laser to the spectroscopic peaks. The simple optical setup is easy to miniaturize and can be readily integrated into more complex experiments. The transition frequency is insensitive to stray magnetic fields and is, therefore, suitable for precision measurements and experimental setups where magnetic fields cannot be completely eliminated, e.g. in a magneto-optical trap or a magnetically trapped Bose-Einstein condensate. Future investigation of the enhanced nonlinear process by embedding an optical nanofiber in such a system will open up new possibilities for the generation of a fiber-integrated photon-pair source for quantum key distribution.

Funding

Okinawa Institute of Science and Technology Graduate University.

Acknowledgments

R. Roy would like to thank B. Hessmo for discussion.

References

1. K. Shimoda, *High-Resolution Laser Spectroscopy*, Topics in Applied Physics (Springer Berlin, 2014).
2. L. S. Vasilenko, V. P. Chebotayev, and A. V. Shishaev, "Line shape of two-photon absorption in a standing-wave field in a gas," *JETP Lett.* **12**, 113–115 (1970).
3. B. Cagnac, G. Grynberg, and F. Biraben, "Spectroscopie d'absorption multiphotonique sans effet Doppler," *J. Phys. (Paris)* **34**, 845–858 (1973).
4. N. Bloembergen, M. D. Levenson, and M. M. Salour, "Zeeman effect in the two-photon $3S - 5S$ transition in sodium vapor," *Phys. Rev. Lett.* **32**, 867–869 (1974).
5. P. Morzyński, P. Wcisło, P. Ablewski, R. Gartman, W. Gawlik, P. Masłowski, B. Nagórny, F. Ozimek, C. Radzewicz, M. Witkowski, R. Ciuryło, and M. Zawada, "Absolute frequency measurement of rubidium $5s-7s$ two-photon transitions," *Opt. Lett.* **38**, 4581–4584 (2013).
6. T. W. Hänsch, "Nobel lecture: Passion for precision," *Rev. Mod. Phys.* **78**, 1297–1309 (2006).
7. S. Gulde, H. Häffner, M. Riebe, G. Lancaster, C. Becher, J. Eschner, F. Schmidt-Kaler, I. L. Chuang, and R. Blatt, "Quantum information processing with trapped Ca^+ ions," *Philos. Transactions Royal Soc. Lond. A: Math. Phys. Eng. Sci.* **361**, 1363–1374 (2003).
8. I. D. Abella, "Optical double-photon absorption in cesium vapor," *Phys. Rev. Lett.* **9**, 453–455 (1962).
9. F. Biraben, B. Cagnac, and G. Grynberg, "Observation of the $3S - 5S$ two-photon transition in sodium vapor without Doppler broadening, using a CW dye laser," *Phys. Lett. A* **49**, 71 – 72 (1974).
10. D. Roberts and E. Fortson, "Rubidium isotope shifts and hyperfine structure by two-photon spectroscopy with a multi-mode laser," *Opt. Commun.* **14**, 332 – 335 (1975).

11. E. Campani, G. Degan, G. Gorini, and E. Polacco, "Measurement of the 8S hyperfine splitting in cesium," *Opt. Commun.* **24**, 203–206 (1978).
12. Y.-W. Liu and P. E. G. Baird, "Two-photon spectroscopy in potassium," *Meas. Sci. Technol.* **12**, 740 (2001).
13. B. A. Bushaw, W. Nörtershäuser, G. Ewald, A. Dax, and G. W. F. Drake, "Hyperfine splitting, isotope shift, and level energy of the 3S states of $^6,7\text{Li}$," *Phys. Rev. Lett.* **91**, 043004 (2003).
14. M.-S. Ko and Y.-W. Liu, "Observation of rubidium $5S_{1/2} \rightarrow 7S_{1/2}$ two-photon transitions with a diode laser," *Opt. Lett.* **29**, 1799–1801 (2004).
15. Y.-C. Lee, Y.-H. Chang, Y.-Y. Chen, C.-C. Tsai, and H.-C. Chui, "Polarization and pressure effects in caesium 6S-8S two-photon spectroscopy," *J. Phys. B: At. Mol. Opt. Phys.* **43**, 235003 (2010).
16. T. W. Hänsch, S. A. Lee, R. Wallenstein, and C. Wieman, "Doppler-free two-photon spectroscopy of hydrogen $1s - 2s$," *Phys. Rev. Lett.* **34**, 307–309 (1975).
17. A. Matveev, C. G. Parthey, K. Predehl, J. Alnis, A. Beyer, R. Holzwarth, T. Udem, T. Wilken, N. Kolachevsky, M. Abgrall, D. Rovera, C. Salomon, P. Laurent, G. Grosche, O. Terra, T. Legero, H. Schnatz, S. Weyers, B. Altschul, and T. W. Hänsch, "Precision measurement of the hydrogen $1S - 2S$ frequency via a 920-km fiber link," *Phys. Rev. Lett.* **110**, 230801 (2013).
18. R. Roy, P. C. Condylis, Y. J. Johnathan, and B. Hessmo, "Atomic frequency reference at 1033 nm for ytterbium (Yb)-doped fiber lasers and applications exploiting a rubidium (Rb) $5S_{1/2}$ to $4D_{5/2}$ one-colour two-photon transition," *Opt. Express* **25**, 7960–7969 (2017).
19. T. Chanelière, D. N. Matsukevich, S. D. Jenkins, T. A. B. Kennedy, M. S. Chapman, and A. Kuzmich, "Quantum telecommunication based on atomic cascade transitions," *Phys. Rev. Lett.* **96**, 093604 (2006).
20. K. D. Bonin and T. J. McIlrath, "Two-photon electric-dipole selection rules," *J. Opt. Soc. Am. B* **1**, 52–55 (1984).
21. A. Pérez Galván, Y. Zhao, and L. A. Orozco, "Measurement of the hyperfine splitting of the $6S_{1/2}$ level in rubidium," *Phys. Rev. A* **78**, 012502 (2008).
22. Grynberg, G., Biraben, F., Giacobino, E., and Cagnac, B., "Doppler-free two-photon spectroscopy of neon. ii. line intensities," *J. Phys. France* **38**, 629–640 (1977).
23. G. Grynberg and B. Cagnac, "Doppler-free multiphotonic spectroscopy," *Rep. Prog. Phys.* **40**, 791 (1977).
24. E. Gomez, S. Aubin, L. A. Orozco, and G. D. Sprouse, "Lifetime and hyperfine splitting measurements on the 7S and 6P levels in rubidium," *J. Opt. Soc. Am. B* **21**, 2058–2067 (2004).
25. E. Gomez, F. Baumer, A. D. Lange, G. D. Sprouse, and L. A. Orozco, "Lifetime measurement of the 6S level of rubidium," *Phys. Rev. A* **72**, 012502 (2005).
26. C. S. Wood, S. C. Bennett, J. L. Roberts, D. Cho, and C. E. Wieman, "Precision measurement of parity nonconservation in cesium," *Can. J. Phys.* **77**, 7–75 (1999).
27. J. Guéna, D. Chauvat, P. Jacquier, E. Jahier, M. Lintz, S. Sanguinetti, A. Wasan, M. A. Bouchiat, A. V. Papoyan, and D. Sarkisyan, "New manifestation of atomic parity violation in cesium: A chiral optical gain induced by linearly polarized $6S-7S$ excitation," *Phys. Rev. Lett.* **90**, 143001 (2003).
28. R. T. Willis, F. E. Becerra, L. A. Orozco, and S. L. Rolston, "Correlated photon pairs generated from a warm atomic ensemble," *Phys. Rev. A* **82**, 053842 (2010).
29. T. Nieddu, V. Gokhroo, and S. Nic Chormaic, "Optical nanofibres and neutral atoms," *J. Opt.* **18**, 053001 (2016).
30. H. You, S. M. Hendrickson, and J. D. Franson, "Analysis of enhanced two-photon absorption in tapered optical fibers," *Phys. Rev. A* **78**, 053803 (2008).